Polar Remote Sensing by CryoSat-type Radar Altimetry

Stenseng, Lars

Publication date:
2011

Document Version
Publisher's PDF, also known as Version of record

Polar Remote Sensing by CryoSat-type Radar Altimetry

Lars Stenseng
PhD Thesis
September 28, 2011

DTU Space
National Space Institute

Polar Remote Sensing by CryoSat-type Radar Altimetry

Lars Stenseng
National Space Institute
PhD Thesis, Copenhagen, September 28, 2011

Financed by National Space Institute, Technical University of Denmark.
Supervised by Rene Forsberg, National Space Institute, Technical University of Denmark,
Jørgen Dall, National Space Institute, Technical University of Denmark and
Carl Christian Tscherning, Niels Bohr Institute, University of Copenhagen.

ISBN: 978-87-92477-06-4

http://www.space.dtu.dk

Resumé

Remote sensing i polområderne med CryoSat lignende radar altimetri

Jordens klima er i forandring og gennem de seneste 30 år er havisens udbredelse faldet stødt, samtidigt har de store iskapper på Grønland og Antarktis oplevet en øget afsmeltning. Udbredelsen af havis kan i dag bestemmes ganske præcis med eksisterende satellitobservationer, men tykkelsen og dermed massen af havis er behæftet med stor usikkerhed. Satellitobservationer af iskapperne er ligeledes påvirket af fejl i randområderne, hvor de største ændringer finder sted. Udviklingen af en ny type radarhøjdemålere, kaldet et SAR altimeter, giver mulighed for at observere iskapperne og havisen i meget større detaljeringsgrad end tidligere.

I denne afhandling er der anvendt SAR altimeter data fra CryoSat-2 og det flybårne ASIRAS instrument til at demonstrere mulighederne i de nye observationer. Med en ny metode, udviklet i forbindelse med studiet, er det muligt at finde dybden af årlige lag i sneen på den Grønlandske indlandsis ved hjælp af ASIRAS data. Disse årlag kan blandt andet bruges til at bestemme nedbøren, en parameter som er vigtig for en nøjagtig bestemmelse og modellering af ændringer i indlandsisens masse.

Der er endvidere udviklet metoder til at skelne mellem radarsignaler reflekteret af havisflager og radarsignaler reflekteret af havet mellem isflagerne. Ved at kunne skelne mellem højder målt over isflager og højder målt over havet kan man bestemme hvor meget af isflagen der er over havoverfladen og dermed bestemme hvor tyk hele isflagen er. Derved kan havisens samlede masse bestemmes mere præsist end tidligere.

Abstract

Polar Remote Sensing by CryoSat-type Radar Altimetry

The Earth's climate is changing and during the last 30 years the extent of the sea-ice has been decreasing steadily. At the same time the major icecaps in Greenland and Antarctica have experienced an increased melt. The extent of the sea-ice can be determined quite accurately with current satellite observations, but the thickness and thereby the mass of the sea-ice is subject to large uncertainties. Satellite observations of the icecaps are also affected by errors in the margin zones, where the largest changes takes place. The development of a new type of radar altimeter, named the SAR altimeter, provides the possibility of observing the icecaps and the sea-ice with a much higher resolution than previously.

In this thesis SAR altimetry data from CryoSat-2 and the airborne ASIRAS instrument have been used to demonstrate the possibilities in the new observations. Using a new method developed during the PhD it is possible to determine the depth of annual layers in the snow on the icecap of Greenland from ASIRAS data. From these annual layers it is possible to estimate the accumulation, which is an important parameter for the precise determination and modelling of changes in the mass of the icecap.

Furthermore, a method has been developed to separate radar signals returned by ice floes from radar signals returned from the sea between the ice floes. When heights measured over ice floes and heights measured over ocean can be separated, the height by which the ice floe is above the sea surface can be determined and hereby the thickness of the entire ice floe. This allows the entire mass of the sea-ice to be determined much more accurately than previously.

Preface

This thesis is submitted in fulfilment of the requirements for obtaining a PhD degree at DTU Space, National Space Institute, Technical University of Denmark. The research was carried out under supervision of Réne Forsberg, Jørgen Dall, and Carl Christian Tscherning.

During my PhD I have had the opportunity to participate in some of the fieldwork and meetings related to the CryoSat-2 mission and through this I have gained a huge network and great experiences. Furthermore, I have had the opportunity to participate in the SAMOSA project and to follow the creation of a new ocean retracker for CryoSat-2 and the upcomming Sentinel-3. By the end of the SAMOSA project I was given the opportunity to propose a work package for the continuation of the project and to lead this work packet.

I am grateful for the help and support I have received from my wonderful family and all my friends and colleagues at DTU Space and out in the world. I wish to thank R. Keith Raney and Robert Cullen for sharing their deep insights in the SAR altimeter, Harald Lentz for instructions on how to operate ASIRAS and sharing the concept and ideas behind its design, and to all the CVRT members who contributed directly or indirectly to this work.

Finally, special thanks goes to Veit Helm from the Alfred Wegener Institute, who was responsible for the bulk processing of the ASIRAS data collected during the CryoVEx campaigns, and to Elizabeth M. Morris from Scott Polar Research Institute for sharing her wisdom and knowledge on glaciology.

Lars Stenseng
Copenhagen, September 2011.

List of Figures

List of Tables

Contents

Chapter 1

Introduction

The Earths cryosphere is changing in response to changes in the climate. Precise measurements of the cryosphere are needed to model how these changes will affect for instance the sea level. Observations show that the sea ice extent has been decreasing steadily over the last 30 years, the marginal zone of the major icecaps are loosing volume and the major glaciers are retreating.

However, these observations do only show part of the picture.

The changes in both the sea-ice thickness and the total mass of the icecaps are essential parameters in the climate models. Therefore precise observations of these parameters are needed in order to minimize the uncertainties in the modelling of the future climate.

The extent of the sea-ice cover can be estimated with high horizontal resolution and accuracy using existing remote sensing observations, e.g. the imaging Advanced Synthetic Aperture Radar (ASAR) onboard ENVISAT. Measurement of the sea-ice freeboard, and thereby the sea-ice thickness, on the other hand suffers from the low horizontal resolution of conventional radar altimeters, making more than 90% of the altimeter observations unsuitable for freeboard estimation. Measuring the height changes over the marginal zone of icecaps are challenging as the nature of the conventional radar altimeter makes it sensitive to surface slopes.

1.1 Background

A new radar altimeter principle was introduced by Raney (1998), which exploit the Doppler effect to enhance the resolution dramatically. The new type of altimeter is called a delay/Doppler altimeter or a synthetic aperture radar (SAR) altimeter. In 1999 The European Space Agency (ESA) selected the CryoSat mission as the first Earth Explorer Opportunity Mission. The CryoSat mission aimed to overcome some of the limitations imposed by conventional radar altimetry. CryoSat uses a novel radar altimeter designed to obtain high resolution radar altimetry observations over sea-ice. Furthermore CryoSat features a second antenna and receiver channel to enable interferometric measurements. The combination of these two techniques is believed to overcome some of the difficulties encountered when observing the marginal zone of the icecaps. This new type of radar altimetry observations is expected to provide the data needed to better understand the interaction between the

climate and the cryosphere.

In preparation for the CryoSat satellite a series of airborne campaigns were carried out with radar altimeters similar to the one on CryoSat. The airborne campaigns were coordinated with in situ observations of the snow and ice properties. Data from these campaigns were distributed amongst the members of the CryoSat Calibration, Validation and Retrieval Team (CVRT) to prepare the community for the new type of radar altimetry. Furthermore, the datasets will be an important part in the interpretation of the radar return signals.

1.2 Objectives of this Thesis

The introduction of a new type of measurements is not without complications. Theory concerning the new instrument and its interaction with the object being observed must be build and understood. Next, investigations of real data is needed to calibrate the instrument and validate the results obtained from the new measurements. As the technique matures the measurements and methods will usually evolve into operational products that are accepted by the user communities.

The objective of this work is to study and develop methods to utilize the unique new features of the SAR altimeters. In the studies an empirical approach to the SAR altimeter datasets are used and aims at extracting information relevant for climatic, oceanographic and geophysical applications. Four important features and properties of the SAR altimeter data have been investigated through studies of real CryoSat-2 and airborne data. All presented studies, implementations and method developments have been carried out by the author unless other is explicit stated.

1.2.1 Studies Included in this Work

The focus area in this work is the Greenland Ice Sheet and the seas around Greenland. However, both the study of retracking methods and sea level mapping for marine gravity field determinations are general and therefore applicable to SAR dataset from other regions of the world.

Retracking of Radar Altimeter Waveforms

The most basic measurement of an altimeter is the distance between the radar and some scattering surface below, which, if combined with accurate knowledge of the radars position, gives the elevation of the scattering surface. The sampling interval of the radar return is usual on the order of 50 cm and a careful analysis of this returned waveform is needed to obtain a better accuracy.

The SAR altimeter introduces a waveform shape, which is significantly different from the waveforms typical obtained with a conventional radar altimeter. Therefore new waveform analysis methods, called retrackers, must be developed and experience with the new waveform types and their dependence of the surface properties must be gained.

This study presents the first comparison of different approaches to retracking of real CryoSat-2 data. The author has developed a software suite consisting of three retrackers adapted from conventional radar altimetry and one simple retracker designed for SAR altimeter waveforms. The performance of the software suite is compared with a state of the

art retracker build on a physical model and developed under ESA contract with participation of the author.

Automatic Detection of Annual Layers in Firn

The mass balance of an ice sheet is a measure for the growth or shrinkage of the ice sheet and therefore an important factor in the estimation of the future sea level. When an ice sheet is growing, water is evaporated from the oceans and stored as ice and snow on the ice cap, which results in a decrease of the sea level assuming that all other variables affecting the sea level are kept constant. If the ice sheet is instead shrinking, mass is transported from the ice sheet to the oceans through calving, runoff and other processes thereby leading to an increase in the sea level. The mass balance of the ice sheet is traditionally modelled from estimates of the accumulation and discharge, or from measurements of the surface elevation change.

The accumulation rate and its variability is an important factor in an attempt to model the mass balance. Traditionally the accumulation rates have been based on snow pits, firn cores and ice cores, but the availability of these are sparse both temporally and spatially. If the mass balance is instead being estimated from changes in the surface elevation, the compaction rate of the firn becomes an important factor in converting the volume change into mass change. Studies have shown that a significant part of the change in surface elevation is caused by the compaction of the firn and therefore not related to changes in the mass.

In the first airborne SAR altimeter data over the Greenland ice sheet it was discovered that layer structures within the dry firn were detectable in the returned waveforms. Studies have shown that the airborne SAR altimeter data can be used to estimate the accumulation rate in the dry snow zone of the Greenland Ice Sheet. In these previous studies the layers have been identified manually in averaged waveforms. This procedure is however slow and due to the manual picking of the layers the results could be biased by the person carrying out the analysis.

The author has developed an automated method to identify and pick layers in the waveforms. With this new method it is possible to process long flight profiles at high resolution in a short time. During the process a set of parameters, related to the properties of the layer, are obtained for each detected layers. These parameters can be used to identify a specific layer in radar profiles obtained some years later. Furthermore, repeated measurements of the layering at a selected position allows an estimate of the average compaction of the firn at the selected position.

The automatic layer detection method and density gradient method developed by the author is compared with in situ measurement of density profiles and a firn compaction model driven by a weather model.

Sea-Ice Lead Detection

One of the main objectives of the CryoSat mission is to obtain precise measurements of the sea ice thickness. Even with the new altimeter type it is not possible to measure the thickness directly, instead the freeboard of the ice floes is measured and converted into thickness using Archimedes principle and assumptions on the density of the sea ice and the sea water.

The freeboard is determined by subtracting the instantaneous sea surface height from

the heights measured by the radar altimeter. However, since the instantaneous sea surface height is unknown it must also be determined from the radar altimeter measurements. Therefore the radar altimeter returns must be separated into returns from the sea between the ice floes and returns from the ice floes. The large area sampled by a conventional radar altimeter will often result in ambiguous returns from a mix of multiple ice floes, ridges and sea water. These ambiguous returns must be removed as they potentially could lead to an erroneous estimate of the sea ice freeboard, leaving only a small fraction of usable returns. The improved resolution offered by the SAR altimeter is expected to greatly increase the amount of useful returns and thereby give a more precise estimate of the freeboard.

An automatic method has been developed by the author to detect leads over sea ice in airborne SAR altimetry data. Two known methods have been adapted and combined to obtain a robust detection of leads in airborne SAR altimetry data. The developed method is compared with manual detected leads using the same radar dataset and airborne laser scanning data.

The developed method has also been applied on real CryoSat-2 data but without a stable result. The method has then been adapted to include more parameters unique to the SAR altimeter data. The adapted method is tested on a single profile of real CryoSat-2 data and compared to an ASAR radar image obtained within 15 minutes of the CryoSat-2 overpass.

Sea Level and Gravity Field Mapping

Traditional radar altimetry over ocean has a limited resolution due to the nature of the conventional radar altimeter. The new SAR altimeter promises better spatial resolution in the along-track direction, which unlike conventional altimeters is independent of the significant wave height. Furthermore, the precision in the determination of sea surface elevation, significant wave height and wind speed is expected to increase when using the new SAR altimeter data.

The developed retracker software suite has been applied on three months of real CryoSat-2 data from the Baffin Bay to map the sea level. The mapped sea level is converted into a gravity field and compared with marine gravity field observations to get an independent evaluation of the obtained sea level map. With only three months of sea level data it is not possible to determine a gravity field, therefore the CryoSat-2 data is combined with data from the ERS-1 geodetic mission. Two sets of combined ERS-1 and CryoSat-2 gravity fields have been calculated. The first combined gravity field treats the CryoSat-2 data in a similar way as the ERS-1 data and the second is optimised to take advantage of the improved features of CryoSat-2. The ERS-1 only and the combined ERS-1 and CryoSat-2 gravity fields are then compared with marine gravity field observations to estimate the effect of adding the CryoSat-2. Finally a method to mask out sea ice in the altimeter data is suggested.

1.2.2 Structure of the Thesis

Chapter 2 gives an introduction to the principle of the SAR altimeter, followed by a presentation of the existing and planed instruments and the datasets available at the time of this thesis. Chapter 3 to 6 presents four studies carried out during the PhD study. Finally Appendix A presents four papers submitted as part of the PhD and a list of publications related to this work with the authors contribution.

Chapter 2

SAR Altimeter Theory, Instruments and Datasets

The principle of the delay compensated synthetic aperture radar (SAR) altimeter was introduced by Raney (1998). This new altimeter type promises higher return power, smaller constant area footprints and speckle reduction through multiple equivalent looks. Compared with a conventional radar altimeter, the only additional hardware demand is that the radar pulses are coherent within a number of pulses, known as a burst.

The Johns Hopkins University Applied Physics Laboratory designed and build the airborne delay-Doppler Phase-monopulse (D2P) radar as a proof of concept for the new radar principle and after initial laboratory tests the D2P gathered the first real SAR altimeter data on a NASA P-3 flight in 2000. The advantages of the delay-Doppler radar were promising and led to the proposal for the ESA satellite CryoSat.

To obtain further experience with the new type of radar altimeter the company Radar Systemtechnique (RST) build the Airborne SAR Interferometric Altimeter System (ASIRAS) on behalf of ESA in 2003. Since then a number of campaigns have been carried out with ASIRAS to prepare scientists and ESA for the calibration and validation of the satellite data. CryoSat was to be the first space-borne SAR altimeter, but was lost in 2005 due to a failure in the launcher. Almost immediately hereafter ESA decided to rebuild CryoSat, with some updates. On April 8 2010 CryoSat-2 was launched and it is now operating successfully.

This chapter will introduce the basic theory of the SAR altimeter and present the existing and planed SAR altimeter instruments. Following this is an overview of the airborne SAR altimeter and CryoSat-2 dataset whereof some are used in this work.

2.1 The SAR Altimeter Principle

The key idea behind the SAR altimeter is to use the Doppler effect to divide the radar footprint into a number of along-track slices, and then average all the slices which illuminate a selected area on the surface. Figure 2.1 shows a conceptual sketch of the SAR altimeter principle, where a selected area on the surface (ΔX_{Dop}) is observed from five different positions.

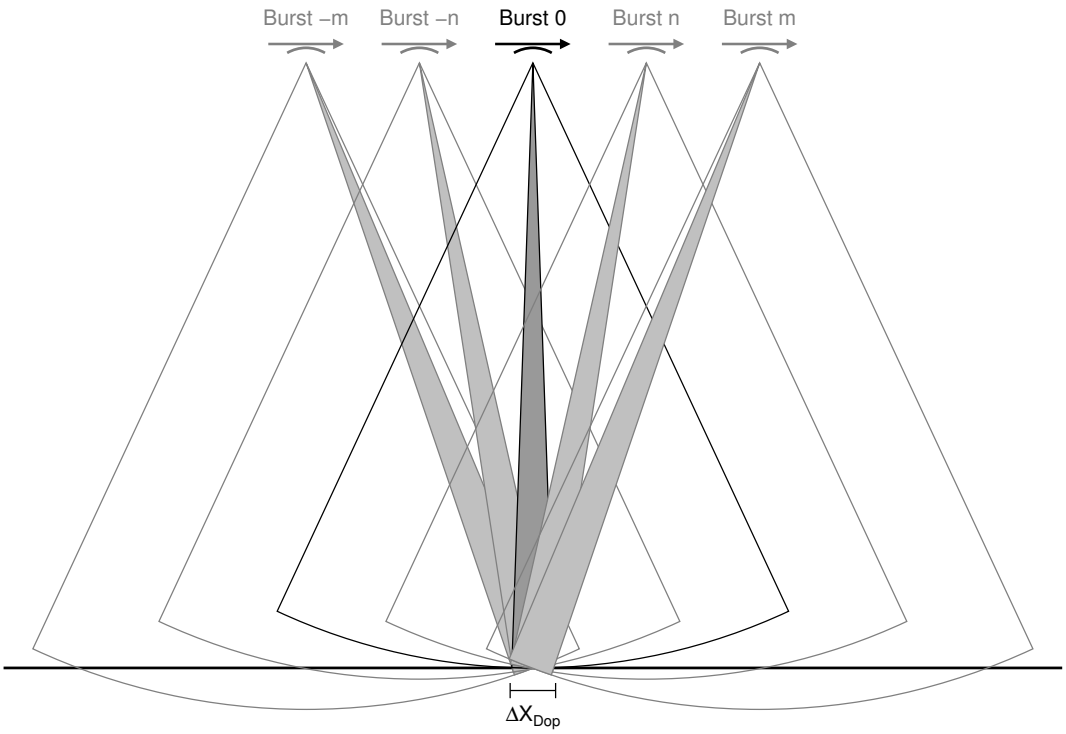

Figure 2.1: Illustration of the SAR altimeter principle, showing beams from five different bursts (-m, -n, 0, n, and m) illuminating a small area on the surface.

The SAR altimeter[1] uses pulse compression in the range dimension as most conventional radar altimeters. The pulse compression is achieved through linear frequency modulation (FM) of the transmitted pulse. The reflected signal is multiplied with a delayed replica of the transmitted FM signal and after low-pass filtering the signal will contain a continuous wave with a frequency which is proportional to the range offset between the delayed FM signal and the true range offset (MacArthur, 1976).

The footprint of a conventional altimeter and the cross-track footprint of the SAR altimeter are both pulse limited, as illustrated in Figure 2.2. The footprint size (ΔX_{pl}) over a quasi-flat surface can be calculated as a function of the radar's height above the surface (h), the pulse length (ρ), and the orbital factor (a derived from the height and the radius of the Earth R_e)(Vignudelli et al., 2011):

$$\Delta X_{pl} = 2 \cdot \sqrt{2 \cdot \rho \cdot \frac{h}{a}} \quad , \quad a = \frac{R_e + h}{R_e} \tag{2.1}$$

The footprint size is dependant of the significant wave height, as ρ can be considered the sum of the pulse length and the significant wave height. The SAR altimeter uses the Doppler principle to achieve a small along-track footprint, and to acquire multiple looks at a surface resolution cell in order to reduce the speckle noise. Figure 2.2 summarizes the differences in footprint geometry between the conventional pulse limited altimeter and the SAR altimeter.

The consequence of the small along-track footprint and the multiple looks is a waveform with a steep leading edge, a fast decaying trailing edge, and a response more than 10 dB stronger at the peak power, compared with an conventional altimeter waveform (Raney, 1998). Figure 2.3 illustrates the differences in the received echoes from a conventional altimeter and the SAR altimeter. As shown in Figure 2.4 simulations suggest that the precision in deriving physical parameters, such as the height, wind speed, and significant wave height, from a SAR altimeter will double compared to a conventional altimeter (Jensen and Raney, 1998).

2.2 SAR Altimetry Processing

The Doppler processing includes some additional steps in the processing chain, compared with conventional altimetry. Figure 2.5 is a flowchart of the SAR altimetry processing, with the SAR specific steps marked in blue.

The receiver (to the left in Figure 2.5) receives a pulse and performs the deramping, using the delayed pulse replica from the chirp generator. The consecutive pulses are stored in the memory, to form a burst of the desired size. When the desired number of pulses have been obtained, a fast Fourier transform (FFT) is performed in the azimuth (along-track) dimension on each range bin, whereby the stored pulses are transformed into range frequency offset versus azimuth Doppler frequency.

The off-nadir Doppler beams observes a target at an apparently longer range, due to the slanted geometry. This range artefact is compensated for by applying a delay phase correction[2]. To transform the range frequency offset into range delay time, an Inverse FFT is applied in the range dimension. The data is then detected to obtain a power echo, as a

[1] In this work the terms delay/Doppler altimeter and SAR altimeter is considered the same.
[2] Delay phase correction is equivalent to a range cell migration correction

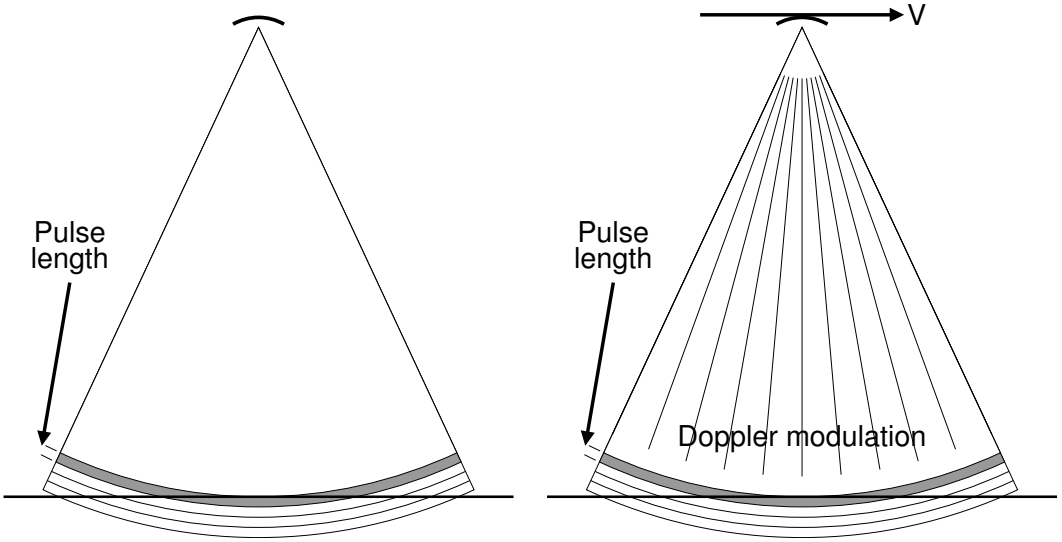

(a) Conventional altimeter footprint seen from the side.

(b) SAR altimeter footprint seen from the side.

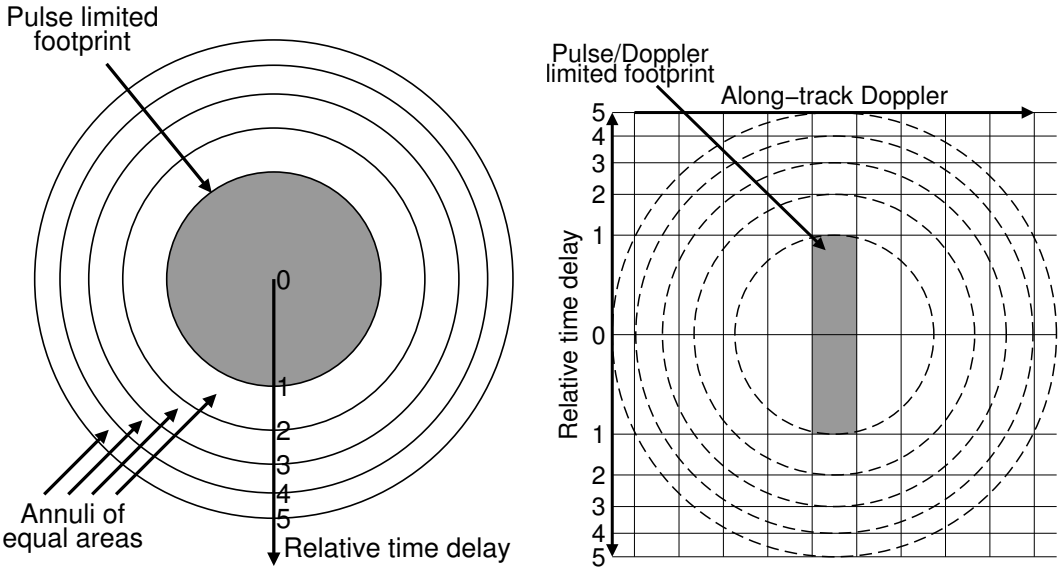

(c) Conventional altimeter footprint seen from the top.

(d) SAR altimeter footprint seen from the top.

Figure 2.2: Comparison of the footprint geometry of a conventional pulse limited radar altimeter and a SAR altimeter. Adapted from Raney (1998).

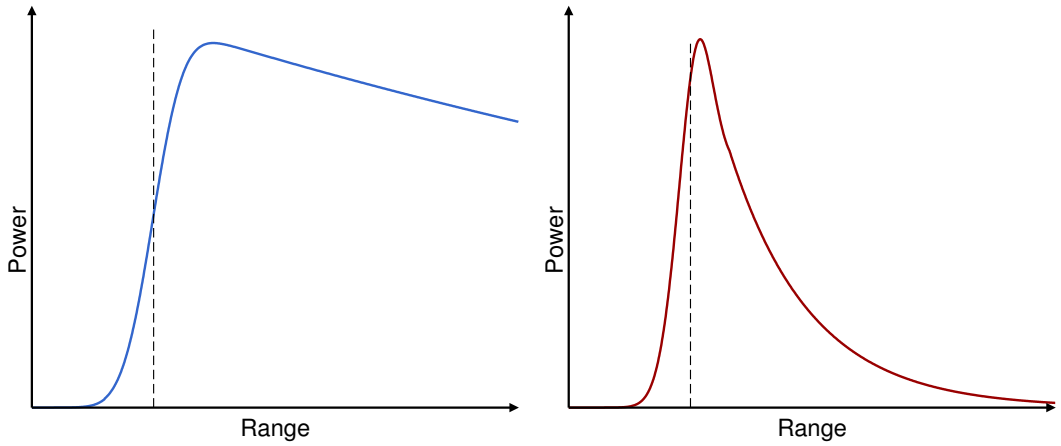

(a) Conventional altimeter echo.

(b) SAR altimeter echo.

Figure 2.3: Idealized shape of a SAR altimeter echo versus a conventional altimeter echo. The response of the SAR echo is expected to be more than 10 dB stronger than a conventional altimeter with equivalent hardware. The position related to the surface is marked with a dashed line. (Adapted from Raney (1998)).

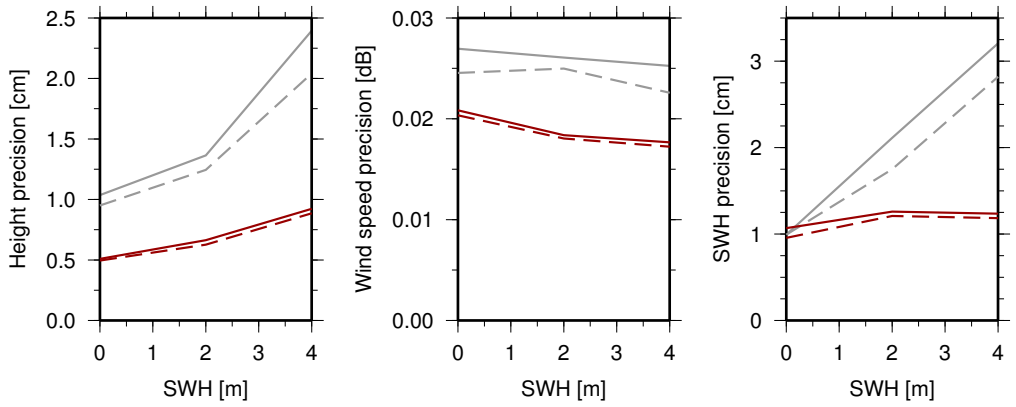

(a) Simulated precision on the height determination.

(b) Simulated precision on the determination of wind speed (σ_0).

(c) Simulated precision on determination of the significant wave height.

Figure 2.4: Expected precision of a SAR altimeter (red) compared to a conventional pulse limited radar altimeter (grey) estimated from simulations. Dashed lines indicates no noise and solid lines 10 dB signal to noise ratio. Adapted from Jensen and Raney (1998).

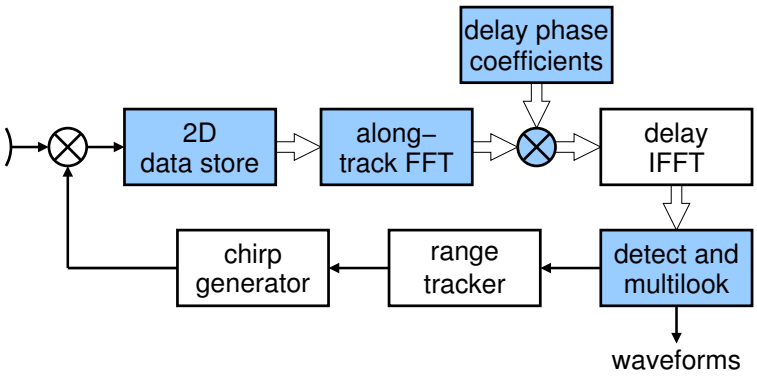

Figure 2.5: Block diagram of the delay/Doppler processing scheme. Blue indicates steps unique to the delay/Doppler altimeter. Outlined arrows indicate transfer of a data matrix and thin arrows indicate transfer of a single row or column. Adapted from Raney (1998)

function of range delay, for each Doppler beam. Finally, all beams from a series of bursts that illuminate a selected area on the ground is summed to form the resulting multi-looked waveform (Cullen and Wingham, 2002; Raney, 1998).

In the description above it is assumed that one beam from a burst will illuminate a selected area on ground, but in reality the position of the nearest beam will move around within the selected area. To ensure that the Doppler beams from different bursts illuminate the same area on the surface, the individual beams must be steered towards the selected area by applying phase shifts to the pulses in the burst prior to the FFT (Cullen et al., 2007).

2.2.1 SAR Altimeter Properties

The Doppler frequency (f_{Dop}) is a function of the emitted wavelength (λ) and radial velocity (v) between the emitter and the reflecting target. For a downwards looking radar instrument travelling at the speed $\overrightarrow{V}$ on an aircraft or satellite, the Doppler frequency at a time, t, of a reflector at a along-track position, t_n, and pointed at by $\overrightarrow{r}$, can be calculated as:

$$\begin{aligned} f_{Dop}(t) &= \frac{2 \cdot \overrightarrow{r}(t-t_n) \cdot \overrightarrow{V}}{\lambda \cdot |\overrightarrow{r}(t-t_n)|} \\ &= \frac{2 \cdot |\overrightarrow{V}| \cdot cos(\theta_n(t))}{\lambda} \\ &= \frac{2 \cdot v(t)}{\lambda} \end{aligned} \tag{2.2}$$

From Equation 2.3 the maximal expected Doppler frequency can be calculated as a function of the platform speed (V) and the along-track antenna beamwidth (θ_b). The Nyquist sampling theorem for complex signals, dictates the minimum required pulse repetition frequency (f_{PRF}) that the instrument has to operate at.

$$f_{PRF} \geq \frac{2 \cdot V \cdot cos(\theta_b)}{\lambda} \tag{2.3}$$

The burst size determines the number of pulses available for the along-track FFT and

thereby how many beams the burst can be divided into. By introducing the number of pulses in a burst (N_{burst}) and the radar's height above the surface (h), it is possible to calculate the along-track Doppler bin size (ΔX_{Dop}), which is equal to the along-track footprint size:

$$\Delta X_{Dop} = \frac{\lambda \cdot h \cdot f_{PRF}}{2 \cdot V \cdot N_{burst}} \tag{2.4}$$

There is an upper bound on the pulse repetition frequency (PRF) for conventional altimeters, at which any two consecutive pulses are uncorrelated and thereby contribute equally to calculation of a statistical mean. This bound was introduced by Walsh (1982) and revisited by R. K. Raney in Vignudelli et al. (2011) resulting in Equation 2.5.

$$f_{PRF\_max} = \frac{2 \cdot V}{\lambda} \cdot \frac{\Delta X_{pl}}{h} \tag{2.5}$$

In a SAR altimeter, consecutive pulses are not used for averaging but are used to describe the Doppler history of the along-track Doppler bins on the surface, and the upper limit described in Equation 2.5 is therefore not valid. However, since beams from consecutive bursts are used for averaging the bound can be imposed here, and thus introduces a lower limit for uncorrelated looks on the burst period (Raney, 2010):

$$V \cdot T_{Burst\_min} = h \cdot \frac{\lambda}{2 \cdot V} \tag{2.6}$$

2.2.2 Critical Look Angle

The amount of looks (or beams) that contribute to a steep leading edge and trailing tail is not unlimited. Beams will contribute to the steep leading edge as long as the selected surface Doppler cell (ΔX_{Dop}) can be observed within a single range bin (Δr_{res}). With an increasing look angle, surface return in the beams cover an increasing number of range cells. Figure 2.6 shows the angle at which the selected surface area spans exactly one range bin. The critical angle (θ_c) can be expressed in terms of the Doppler cell size and the range resolution (Raney, 2010):

$$\theta_c < k \cdot \frac{\Delta r_{res}}{\Delta X_{Dop}}, \tag{2.7}$$

where k is a factor depending on the tolerance of the resulting waveform.

2.2.3 Example of Doppler Beams

Figure 2.7 shows an example of all slant range corrected looks available for a SAR waveform, obtained with the ASIRAS instrument over the Fram Strait. In the top plot the speckle noise is clearly visible, and so is the smearing of the power over multiple range bins in the lowest and highest beam bins. In the lower plot it is seen how the power is bound between two hyperbolas, as a effect of the slant range correction. The hyperbola to the right is caused by the end of the sample window for the radar (e.g. around beam bin 5 and range bin 100). In this plot it is also seen how the maximal power in each beam is arranged around range bin 100, and how the peak power drops and smears out when moving away from the center beam (i.e. beam 80).

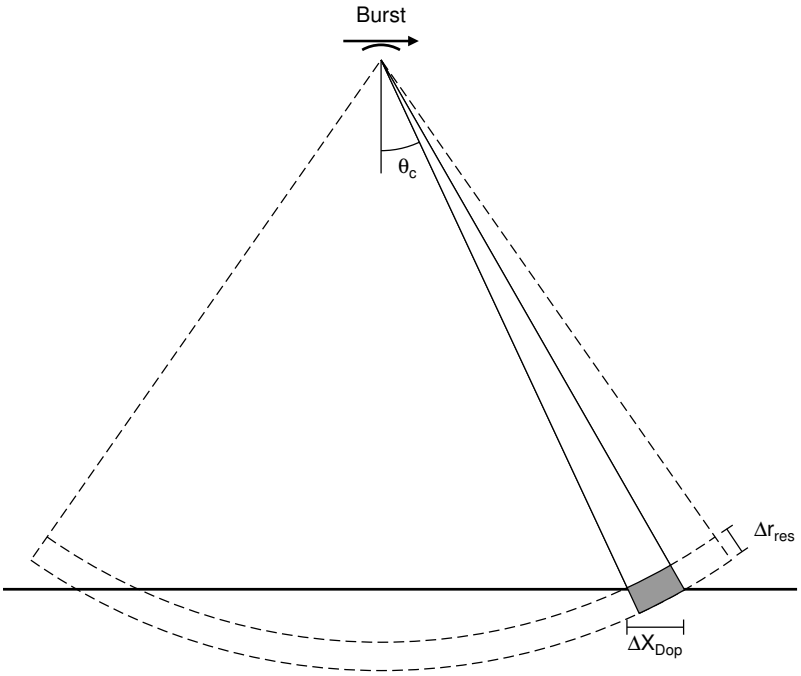

Figure 2.6: Critical look angle.

2.3 Airborne SAR Altimeters

The major differences between an airborne and a spaceborne altimeter system lies in the geometry between the surface and the radar. Some differences are obvious, as for example the shorter travel time of the airborne system due to the shorter distance to the surface. Other differences are more subtle; such as the footprint of an airborne radar often being beam limited, while a spaceborne system tends to be pulse limited. The reason for this is that the radius of the beam limited footprint grows linearly as a function of range, while the radius of the pulse limited footprint only grows with the square root of the range.

Due to the short travel time in airborne systems, it is possible to receive an emitted pulse before the next pulse is emitted, and still maintain a high PRF. With the constant stream of pulses the burst size can be decided during post-processing, as shown in Figure 2.8. Choosing the burst size during post-processing allows studies of the effect of the burst size, and this makes the system very flexible.

The following will introduce the two airborne SAR altimeters flown in preparation for the CryoSat mission.

2.3.1 Delay-Doppler Phase-Monopulse Radar (D2P)

The D2P radar was designed and build in 2000 at the Johns Hopkins University, Applied Physics Laboratory, as part of the NASA incubator program (Leuschen and Raney, 2005). The D2P is a proof of concept instrument to demonstrate the SAR altimeter principle and the possibilities of cross-track interferometry from a dual receiver chain. Comparison of

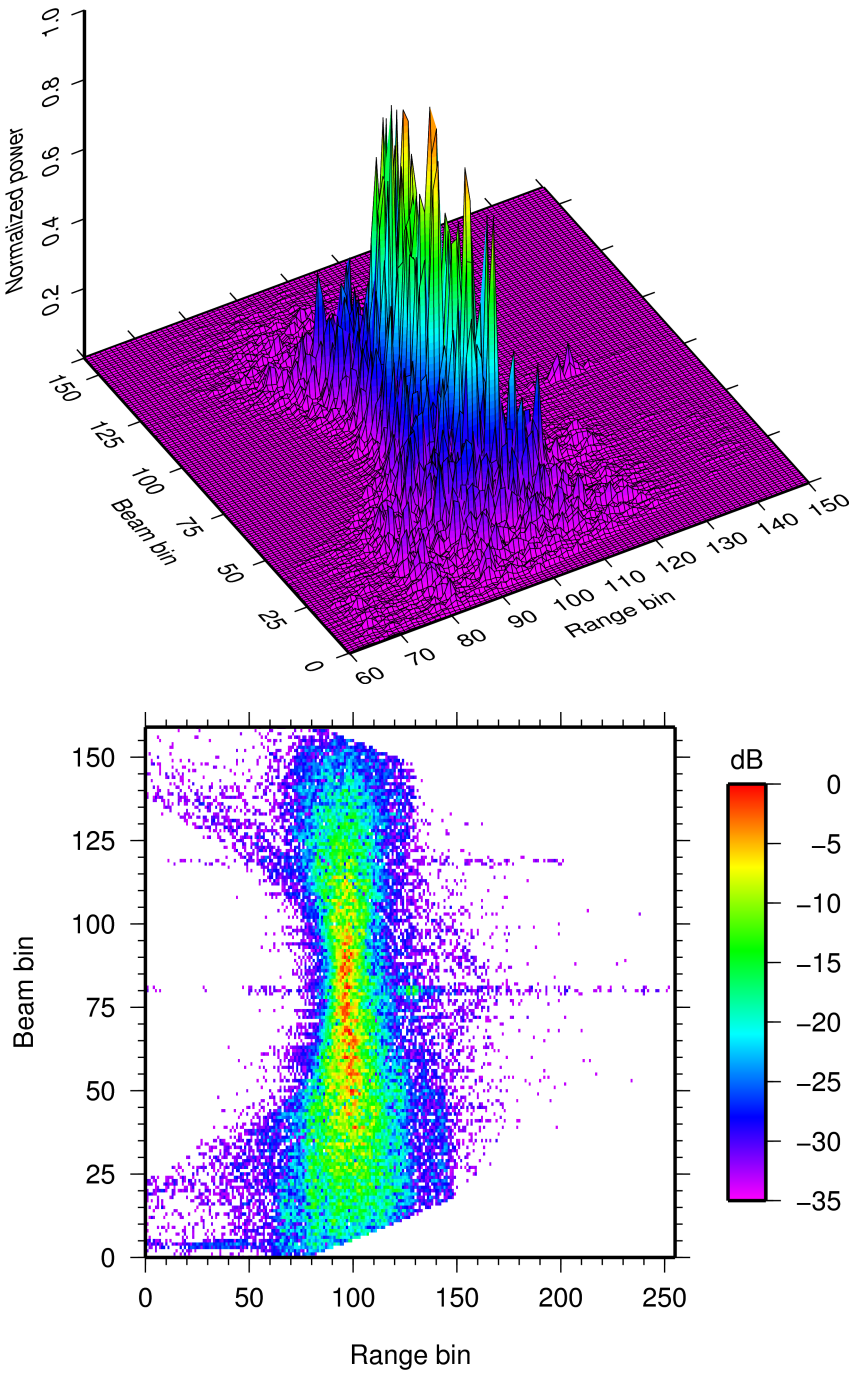

Figure 2.7: Example of the individual beams used to form one ASIRAS waveform obtained over ocean. Adapted from Stenseng (2009).

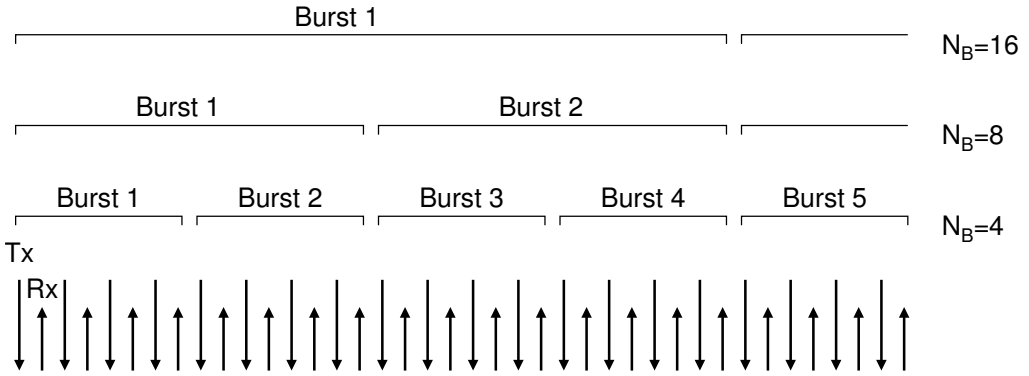

Figure 2.8: The short travel time associated with an airborne SAR radar allows the burst size to be chosen during post-processing.

Centre frequency	13.900 GHz
Bandwidth	360 MHz
Transmit power	5 W
Antenna beamwidth (along-track)	4.0°
Antenna beamwidth (across-track)	8.0°
Antenna baseline	0.15 m
Sample interval	0.42 m
Samples per echo	128
Range window	54 m
PRF	1.00-1.75 kHz
Operational altitude	200-10,000 m

Table 2.1: Key parameters associated with the D2P instrument. From Leuschen and Raney (2005)

the key parameters (Table 2.1) of D2P and the SAR/interferometric altimeter (SIRAL) instrument on CryoSat-2 (Table 2.3) reveals many common features. Some parameters must however be scaled to accommodate the inherent differences between an airborne and a spaceborne system. The PRF, for example, can on one hand be reduced significantly for the D2P due to the much lower platform speed, but on the other hand it must be increased to accommodate a broader along-track antenna beam width needed to allow for the aircraft's movement.

In 2002, the D2P was flown on a NASA airplane in a joint NASA/ESA experiment (the LaRa campaign) to collect radar and laser data over inland ice and sea-ice. One year later in spring 2003, the first airborne CryoSat Validation Experiment (CryoVEx) campaign was carried out using the D2P instrument (Leuschen and Raney, 2005).

The installation of the D2P on the Air Greenland Twin-Otter OY-POF, during the CryoVEx 2003 campaign, is shown in Figure 2.9. The two D2P instrument racks are shown in the right hand side of Figure 2.9a. The instrument rack on the left contains the power supply, GPS receivers, and data collection computers for the inertial navigation system (INS) and laser scanner. Figure 2.9b shows the antenna assembly, with the two antenna elements, mounted underneath the aircraft. Each of the two antenna elements are approximately 15 cm across-track and 30 cm along-track and covered by a protective radome.

(a) Instrument rack installed in the cabin. D2P to the right and support instrumentation (incl. pc for laser scanner) to the right.

(b) Antenna mounted under the baggage compartment.

Figure 2.9: The D2P radar installed in the Air Greenland Twin-Otter OY-POF.

2.3.2 Airborne SAR/Interferometric Altimeter System (ASIRAS)

ASIRAS was developed under the ESA technology research program and build by the Radar Systemtechnik (RST) company. ASIRAS is the main airborne instrument for the calibration and validation of CryoSat-2 and, like the D2P radar, it has features similar to the satellite, but scaled to airborne use. However the scaling for ASIRAS is somewhat different from the scaling used by the D2P system.

The bandwidth, and thereby the range resolution, on ASIRAS is higher than on the SIRAL and the D2P, in order to allow a more detailed study of the radar returns. The higher bandwidth also shrinks the pulse limited part of the footprint, and thereby make it less beam limited and more pulse limited.

To ensure a reliable data collection over steep and rapidly varying terrain, it was decided to use a 10° along-track antenna beam, thus making ASIRAS less sensitive to aircraft pitch manoeuvres. The wide antenna pattern increases the demands on the PRF to allow the Doppler spectrum to be sampled unambiguously. The key parameters of the ASIRAS radar are shown in Table 2.2.

The ASIRAS was originally designed to operate in a SAR interferometric mode, called high altitude mode (HAM). In HAM the distance to the surface must be larger than 1000 m to allow a clear separation of the transmitted and received signal. After the first campaigns the need for coincident collection of laser and radar data came up, but the minimum distance needed by ASIRAS was too far for most commercial laser scanner systems. To overcome this problem an extra mode, the low altitude mode (LAM), was added to the ASIRAS firmware in 2005. Essentially the LAM is achieved by stretching the transmitted pulse and letting one radar chain be used for transmitting, while the other chain is used to receive. The received signal is then multiplied with the signal being transmitted to achieve the deramping, and in this way the minimum range to the surface can be reduced significantly. An inherent problem with this approach is that the data volume is increased by a factor proportional to the stretch factor of the pulse length. The problem with the large

	HAM	LAM	LAM-A
Centre frequency		13.500 GHz	
Bandwidth		0.100-1.000 GHz	
Tramsmit power		5 W	
Antenna beamwidth (along-track)		10°	
Antenna beamwidth (across-track)		2.5°	
Antenna baseline	0.77 m	-	-
Sample interval	0.0878 m	0.1098 m	0.1098 m
Samples per echo	256	4096	1024
Range window	22.5 m	450 m	112.5 m
PRF		2.50-15 kHz	
Operational altitude	1-7 km	100-1400 m	100-1400 m

Table 2.2: Key parameters for the ASIRAS instrument. From Cullen (2010); Lentz et al. (2002); Mavrocordatos et al. (2004)

(a) Instrument rack installed in the cabin.

(b) Antenna mounted under the baggage compartment.

Figure 2.10: The ASIRAS radar installed in the Air Greenland Twin-Otter OY-POF.

data volumes was solved in 2007, with the introduction of the LAM-A, by a reduction of the range window. One major drawback of LAM and LAM-A is that the interferometric capabilities are lost.

The rack with the ASIRAS instrument is shown in Figure 2.10a underneath the GPS receiver used for datation of the ASIRAS observations. Figure 2.10b shows the more than 1.5 m wide ASIRAS antenna assembly. The two antenna elements are 70 cm by 18 cm each and covered by two protective radomes. (Cullen, 2010; Lentz et al., 2002; Mavrocordatos et al., 2004)

2.4 Spaceborne SAR Altimeters

CryoSat was to be the first SAR altimeter in space, but due to a failure in the launcher the satellite never reached its orbit. Almost five years later, CryoSat-2 was launched on April 8 2010 on a Dnepr SS-18 intercontinental ballistic missile from the Baikonur Cosmodrome

in Kazakhstan. Three days later, on April 11, a new era in spaceborne altimetry began with the activation of the altimeter SIRAL.

This section will introduce the CryoSat-2 mission and the features of the on-board radar altimeter. The next planned satellite SAR altimeter mission Sentinel-3 is also introduced. Sentinel-3 is part of the Global Monitoring for Environment and Safety (GMES) program and will provide operational monitoring data in continuation of ENVISAT, as the first long term SAR altimeter mission.

2.4.1 CryoSat-2

CryoSat-2 is an opportunity mission and part of the Earth Explorer Missions under the ESA Living Planet Program. The main focus of the mission is to determine changes in the major land and sea-ice masses. The orbit inclination of 92° was chosen as a compromise between a high number of crossovers and a complete coverage of the Arctic Ocean and Antarctica (Francis, 2007).

SAR Interferometric Radar Altimeter (SIRAL)

The SIRAL instrument is a single frequency radar altimeter operating in the K_u-band and uses the full deramp pulse compression (MacArthur, 1976) as most radar altimeters today. However, SIRAL is capable of operating at a PRF ten times higher than a conventional altimeter. The high PRF ensures coherent sampling and together with pulse to pulse phase coherence, a series of pulses can be combined to form an equal amount of synthetic beams, with footprints much smaller in the along track direction than a conventional altimeter.

Furthermore, SIRAL has two receiver chains and antennas which enable cross track interferometric capabilities. To allow the cross track interferometry it is necessary to place the two antennas next to each other on the satellite. Due to the size restrictions set by the launch vehicle the two antennas had to be reduced in size, but smaller antennas means a loss of gain. To accommodate the size restrictions, while maintaining the highest possible gain, a set of elliptical antennas was designed. The elliptical antennas makes the footprint slightly elongated in the cross track direction (Francis, 2007; Wingham et al., 2006). The key parameters for the SIRAL instrument, are summarised in Table 2.3

Altimeter Modes

The SIRAL instrument is capable of operating in three different modes (Figure 2.11); the low resolution mode (LRM), the synthetic aperture mode (SAR), and the SAR interferometry mode (SARin). Common to all three modes is the radar cycle, with a fixed duration of 46.7 ms, which is used to synchronise datation and to update the on-board tracking software.

Low Resolution Mode (LRM)

The LRM mode is comparable to the operation of a conventional altimeter and is used over the open ocean and the relatively flat central parts of the Greenland and Antarctic inland ice. In this mode the altimeter emits pulses at a constant PRF of 1970 Hz at which rate the echoes are expected to be decorrelated from pulse to pulse, and can be incoherently

	LRM	SAR	SARin
Centre frequency		13.575 GHz	
Bandwidth		350 MHz	
Tramsmit power		25 W	
Antenna beamwidth (along-track)		1.0766°	
Antenna beamwidth (across-track)		1.2016°	
Antenna baseline	-	-	1.172m
Sample interval		0.47 m	
Samples per echo	128	128	512
Range window	60 m	60 m	240 m
PRF	1970 Hz	17.8 kHz	17.8 kHz
Pulses per burst	-	64	64
Azimuth looks per radar cycle	91	240	60

Table 2.3: Key parameters for the SIRAL instrument. From Francis (2007)

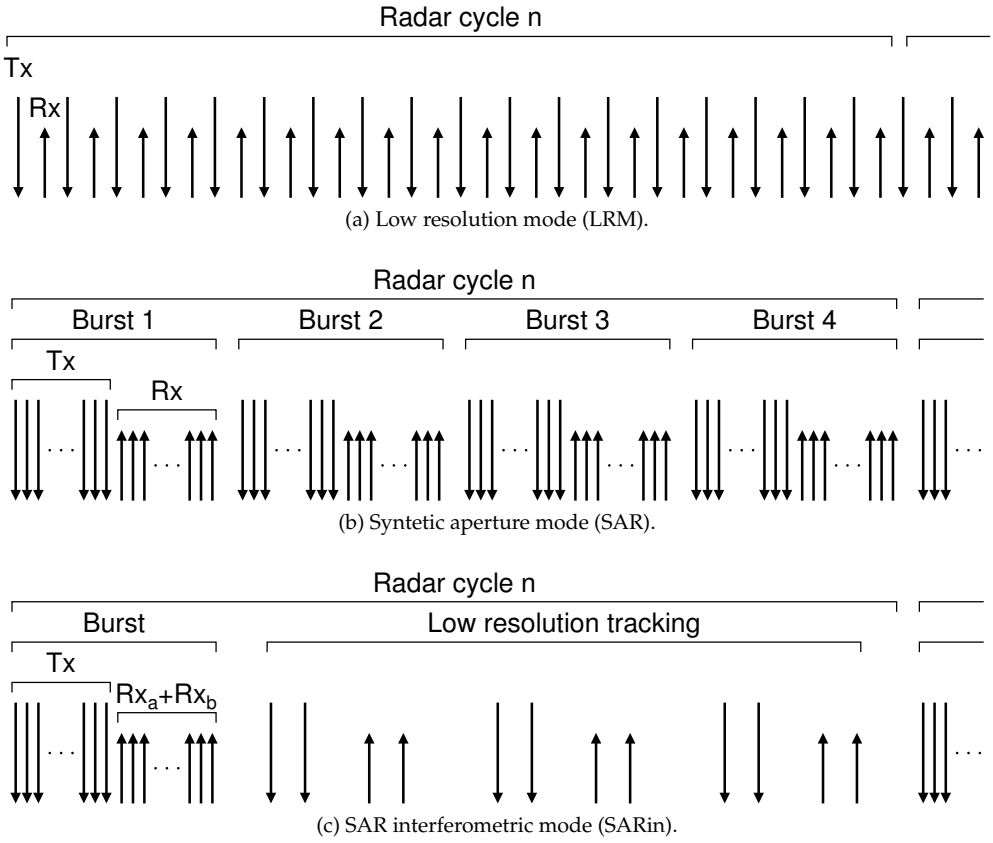

(a) Low resolution mode (LRM).

(b) Syntetic aperture mode (SAR).

(c) SAR interferometric mode (SARin).

Figure 2.11: Concept of transmitting and receiving pulses in the three different modes. To the far right the beginning of the next radar cycle is seen. Adapted from Francis (2007).

averaged on-board to reduce the speckle noise. Each LRM radar cycle consists of 91 pulses which are averaged on-board, to form the 20 Hz product and to update the on-board tracker (Francis, 2007; Wingham et al., 2006).

Synthetic Aperture Mode (SAR)

The SAR mode is intended to be used over the sea-ice and some coastal zones. The radar cycle for the SAR mode is divided into four burst of 11.7 ms duration each (Figure 2.11b). Within each burst 64 pulses are emitted at a PRF of 17.8 kHz and subsequently all 64 pulses are received and the next burst takes place. All echoes in the four burst are sampled and downlinked to the ground station where the data is processed as described in Chapter 2.

SAR Interferometry Mode (SARin)

The SARin mode targets the steep slopes over the margin of the ice sheets and the mountainous regions on land. To keep track over the rapidly varying surface the range window is four times larger than the range window used in LRM and SAR mode. Furthermore, the SARin radar cycle combines one burst of 64 pulses at 17.8 kHz with a series of low bandwidth tracking pulses. The low bandwidth tracking pulses are used to ensure that the SARin sampling window is positioned correctly with respect to the surface.

When operating in SARin mode one transmit chain is used to emit a pulse and both receive chains are used for the reception of the return. By using a combined processing of the two returns, it is possible to calculate the phase difference and thus derive the cross track angle to the scattering surface.

SIRAL Mode Mask

To determine which mode to operate in, CryoSat-2 uses an on-board geographical mask. The mask is dynamical and changes with season to reflect the expected changes in the sea-ice extend. Furthermore, the mask can be changed on demand by the ground control group to accommodate special requests. Figure 2.12 shows an example of the SIRAL mode mask for maximal sea-ice extent in both the northern and southern oceans.

2.4.2 Sentinel-3

The next SAR altimeter mission is already planed by ESA and the satellite Sentinel-3 is currently being build.

Sentinel-3 is part of the Global Monitoring for Environment and Security (GMES) Space Component, which will be providing services primarily for marine monitoring and delivering products in continuation of Envisat. The first Sentinel-3 satellite is expected to be launched in 2013 and will shortly afterwards be followed by a second satellite, thereby providing global coverage in two days. The Sentinel-3 satellite will carry the SRAL altimeter along with a suite of instruments for measuring land and sea-surface temperature and colour (Aguirre et al., 2007; European Space Agency, 2010).

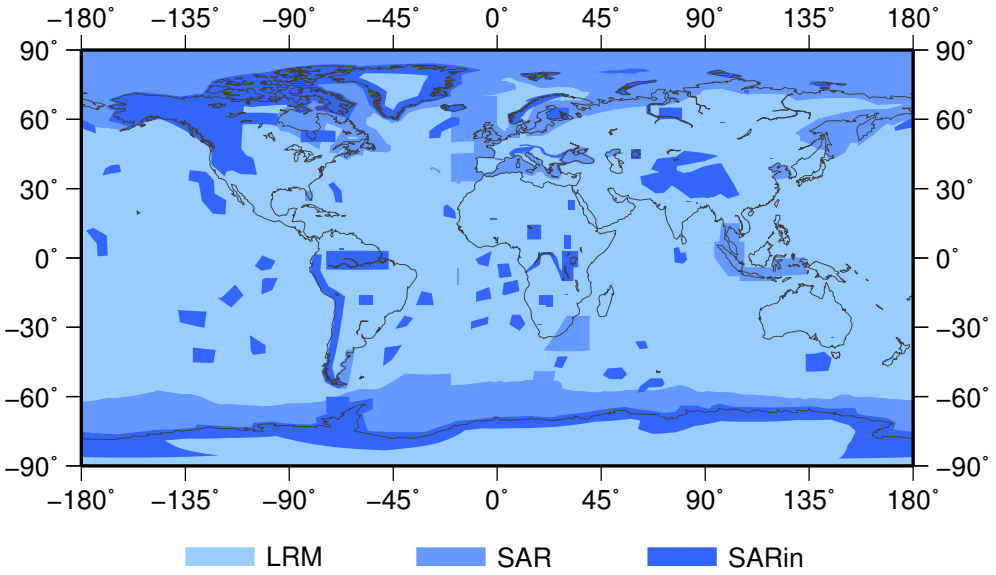

Figure 2.12: CryoSat-2 mode mask, with maximal sea-ice SAR zones at both the South and North Pole.

SAR Radar Altimeter (SRAL)

The Sentinel-3 satellites will carry a dual frequency altimeter operating at K_u- and C-band and with the ability to operate in LRM and SAR mode. The dual frequency altimeter allows a direct measurement of the ionosphere disturbance and thereby allows a very accurate correction. This is furthermore supported by a microwave radiometer, which measures the water vapour and thereby improves the estimate of the tropospheric delay on the altimeter measurements.

2.5 CryoSat Type Datasets

Since 2000 a number of airborne campaigns have been carried out using SAR altimeters. The first campaigns were to prove the SAR altimeter concept and to gather experience with the instruments. Since then several airborne campaigns have taken place primarily in the Arctic around Greenland.

The CryoSat-2 radar instrument SIRAL was activated on April 11 2010 and began the initial check of functionality. After a series of tests CryoSat-2 began to collect data for distribution in mid July 2010 and has since continued the collection of data.

In the following the existing datasets will be introduced and an overview of the data used in this work will be given.

2.5.1 CryoSat Validation Experiment (CryoVEx)

When a new type of measurement is introduced there is a need to understand and describe the uncertainties and their sources. To address this task the CryoSat Calibration, Validation,

Campaign	Period	Area	Reference
CryoVEx 2003	April 1 - April 22 2003	EGIG, Austfonna, and Greenland Sea	Keller et al. (2004)
CryoVEx 2004 Spring	April 19 - May 9 2004	EGIG, Austfonna, and Devon	Helm et al. (2006)
CryoVEx 2004 Autumn	August 30 - September 17 2004	EGIG and Devon	Helm et al. (2006)
CryoVEx 2005	March 13 - March 15 2005	Bay of Bothnia	Helm et al. (2006)
CryoVEx 2006	April 18 - May 18 2006	EGIG, Austfonna, Kongsvegen, Devon, Greenland Sea, and Licoln Sea	Stenseng et al. (2007)
CryoVEx 2007	April 5 - April 24 2007	Austfonna and Kongsvegen	Helm and Steinhage (2008)
CryoVEx 2008	April 15 - May 8 2008	North Greenland, EGIG, Devon, Greenland Sea, and Licoln Sea	Hvidegaard et al. (2009)
CryoVEx 2008 Antarctica	December 18 2008 - January 6 2009	Antarctica	Helm et al. (2009)

Table 2.4: Overview over CryoVEx campaign periods and areas.

and Retrieval Team (CVRT) was formed. Based on the document "CryoSat Calibration & Validation Concept" (Wingham et al., 2001) the CVRT members designed a number of experiments to address various aspects of the validation and calibration of the CryoSat measurements.

The experiments, collectively called CryoVEx, consisted of both in situ and airborne measurement of inland ice and sea-ice. During a campaign the ground teams carry out a suite of measurements of snow and ice properties at various spatial scales, which can be used in the validation process. The ground teams also, when possible, put up radar corner reflectors for calibration of the ASIRAS instrument. The CryoVEx campaigns are summarised in Table 2.4.

In spring 2011 the latest CryoVEx campaign took place and for the first time satellite, airborne and in situ data were collected simultaneous. The airborne data is currently being processed and is expected to be released in the beginning of 2012.

CryoVEx 2006

CryoVEx 2006 was the first grand tour campaign covering all the Arctic sites chosen as CryoSat validations sites (Figure 2.13). The airborne campaign took place in the period from April 20 to May 18 2006 during which approximately 4.5 Tb of raw ASIRAS data was collected, primarily in LAM. Apart from the ASIRAS data, GPS, INS, laser scanner data and aerial photos were also collected during the flights (Stenseng et al., 2007).

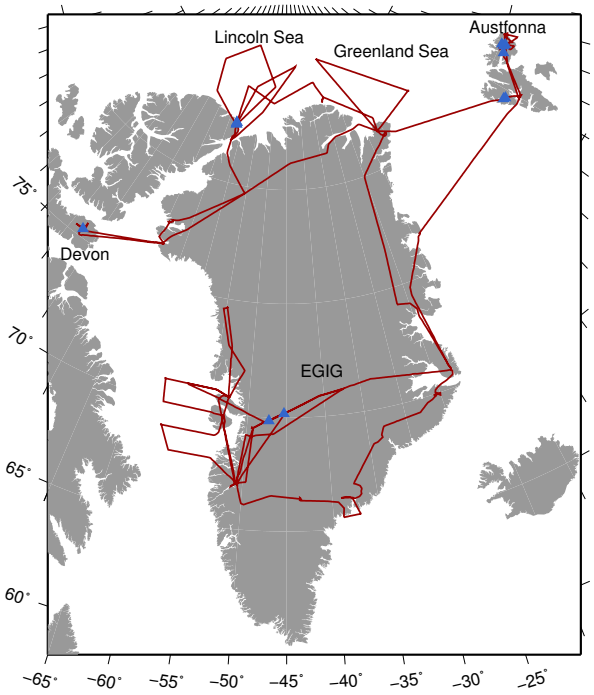

Figure 2.13: Flight routes during CryoVEx 2006 (red) and validation sites with radar corner reflectors (blue triangle).

CryoVEx 2008

The CryoVEx 2008 campaign revisited many of the 2006 sites, but this time including a profile in north-east Greenland instead of the sites on Svalbard (Figure 2.14). A dataset similar to the 2006 dataset was collected in the period from April 17 to May 7 2008, but ASIRAS data was collected in LAM-A which reduced the collected volume of raw ASIRAS data to less than 1.5 Tb.

2.5.2 CryoSat-2 Commissioning Phase Dataset

One of the major goals of the commissioning phase is to estimate various instrument specific parameters such as e.g. internal delays in the transmit/receive chain and the phase difference between the two chains in the interferometer. During this phase a series of soft- and hardware tests are performed on-board the satellite together with specific manoeuvres designed to target various calibrations tasks. During the commissioning phase the first functional processor is used to derive a preliminary version of the level 1b SAR and SARin data, which is distributed to the CVRT.

The data issues identified by ESA and the CVRT is investigated and, if possible, resolved in future versions of the processor. When the level 1b product is considered stable and the instrument parameters have been determined, the higher level products will be generated. For the LRM data the processing methods are well established and it is therefore possible to release both level 1b and level 2 data at an earlier stage.

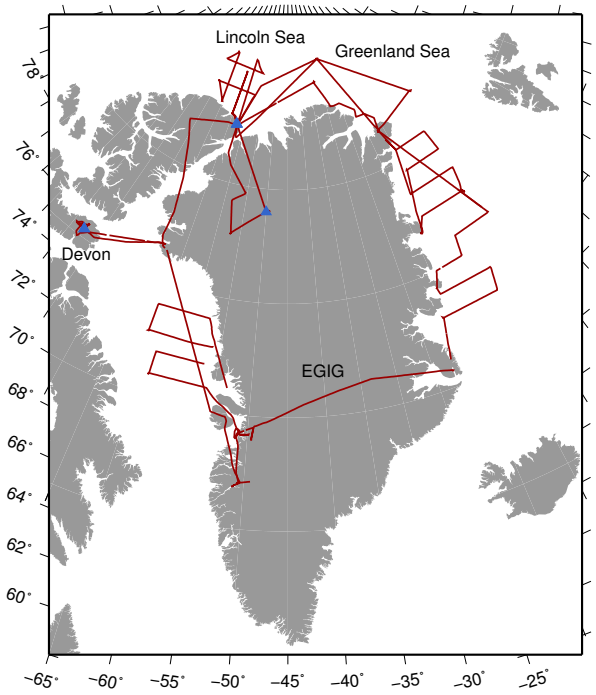

Figure 2.14: Flight routes during CryoVEx 2008 (red) and validation sites with radar corner reflectors (blue triangle).

The presented data from CryoSat-2 is part of the first release (from July 2010 to January 2011) of commissioning phase data to the CVRT. Being the first release to the broader CVRT community, it must be considered preliminary, and therefore incomplete or erroneous datasets must be expected.

The following will provide some comments about general observations made on the level 1b SAR and SARin data products. The observations are made based on the first data release and are therefore likely to be invalid for future data releases.

SAR Data

The SAR waveforms in this first data release is generally of a high quality, with little noise. However, a check of the waveforms reveals that the last part of the trailing edge is missing and replaced by zeroes. Figure 2.15 shows a random picked waveform where the last 28 samples are missing (arrow to the right). A non exhaustive investigation shows that in rare cases a waveform have more than 60 missing samples.

The left arrow in Figure 2.15 marks a toe at the beginning of the leading edge. This toe is found in all SAR and SARin waveforms and is believed to be caused by beams with a high look angle, as described in Section 2.2.2.

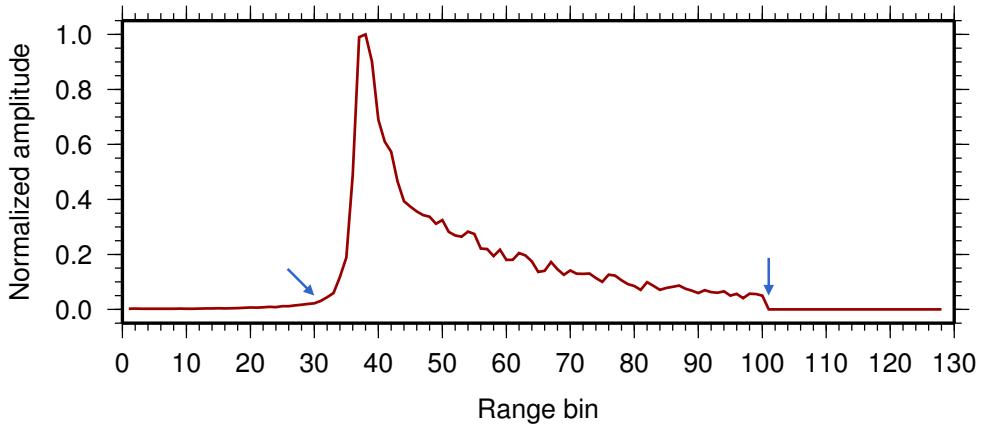

Figure 2.15: Leading toe and zero padding of a SAR waveform obtained over ocean.

SARin Data

The SARin waveforms are generally more noisy than SAR waveforms, which is to be expected as the SAR waveforms are averaged over four times as many echoes. A number of spikes are found in the SARin waveforms around the peak, very similar to speckle noise (left arrows in Figure 2.16a). However, in some waveforms a spike is found in front of the leading edge which is not compatible with speckle noise. Instead the spikes are believed to be an artefact of the data processor.

The interferometer phase difference waveform have a stable phase difference near the leading edge, followed by a gradual increase as the illuminated area moves away from nadir. Since the interferometer has not yet been calibrated the -0.5 π phase difference found in Figure 2.16c must be considered arbitrary.

The coherence between the two channels shown in Figure 2.16c is high around the leading edge, thereby indicating that the two channels see the same signal here. After the leading edge the coherence drops rapidly before slowly rising again as the phase difference approaches the point where the phase difference is π from the phase difference at the leading edge.

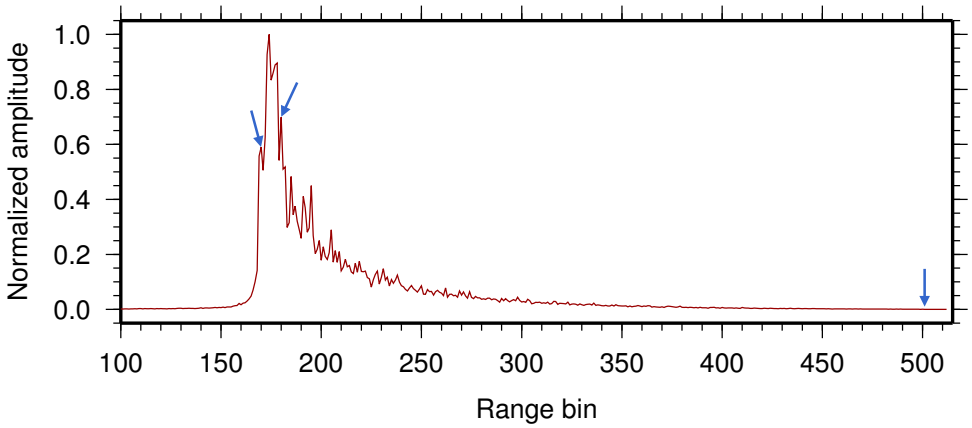

(a) Power waveform.

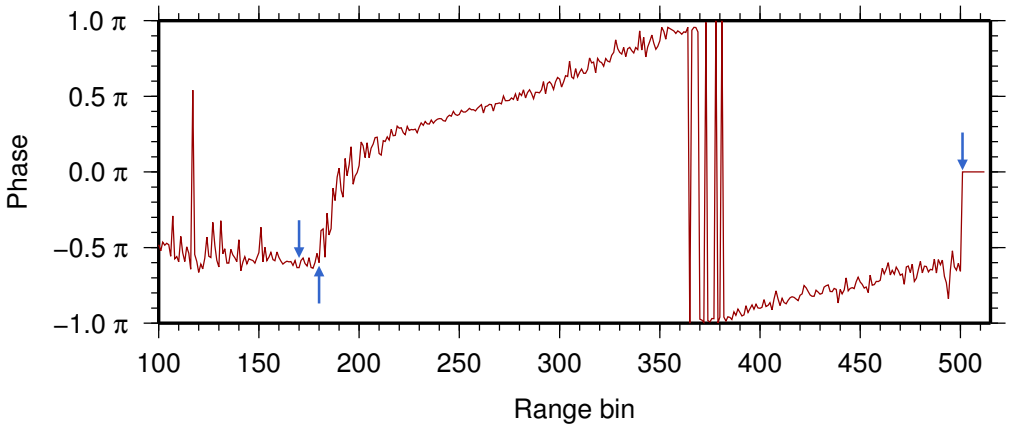

(b) Interferometer phase difference.

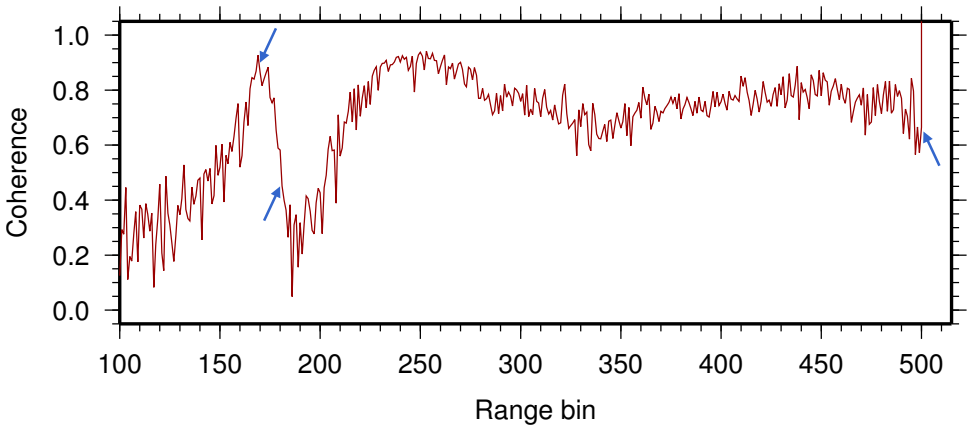

(c) Coherence between the two interferometer channels.

Figure 2.16: Power, interferometer phase, and coherence for a SARin waveform obtained over ocean. The two blue arrows to the left marks spikes in the amplitude and the arrow to the right marks the zero padding.

Chapter 3

Retracking of Radar Altimeter Echoes

In order to retrieve information about the range from the radar to a reflecting surface the radar uses an on-board tracker. The tracker estimates the range to the surface using a simple algorithm, and centres the sampling window at the estimated range. The position of the sampling window is adjusted when needed to keep the surface sample at a fixed position in the sample window, and thereby ensuring a sufficient sampling of the echo. The range to the surface determined by the on-board tracker will be biased by the surface type and quantified by the size of a sampling bin, and is therefore only useful as a rough estimate of the range to the surface.

To obtain a better estimate of the range to the surface the echo must be analysed more thoroughly. The shape of a returned radar echo is a combination of the range to the different illuminated reflectors, their scattering properties and their position within the antenna beampattern. The complexity of the returned echo is therefore related to the complexity of the entire illuminated surface. Finally, the returned echo is affected by thermal and speckle noise as well as the impulse response of the radar.

A whole suite of retrackers for exists to accommodate the various echoes from different surface types (e.g. open ocean, coastal zone, sea-ice and inland ice). The existing retrackers are constantly improved, and new ones are introduced, allowing better estimates of parameters or more information to be extracted. The increasing processing power available on computers has allowed an emerging shift toward physically based models in favour of empirical models. All these retrackers are build for conventional radar altimeters and therefore existing retrackers must be adapted or new ones developed to accommodate the SAR altimeter echoes.

The following sections will give an overview of existing retrackers relevant for SAR altimeter waveforms and will give an introduction to the SAMOSA retracker currently under development and implementation. The author has developed a software suite by implementation of four of the presented retrackers. The performance of the software suite has been tested and compared with each other and with the SAMOSA retracker using a real CryoSat-2 profile from the Davis Strait. The SAMOSA retracking of the profile has kindly been provided by Christine Gommenginger from the National Oceanography Center. Finally, examples of the fitted retracker functions are presented together with the CryoSat-2

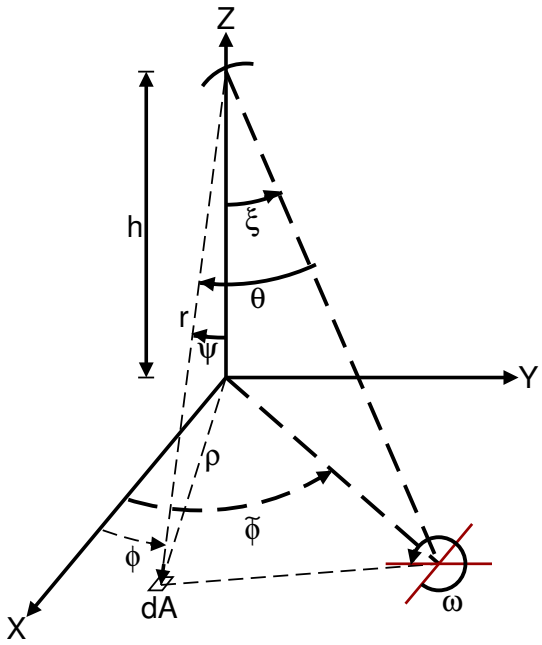

Figure 3.1: Geometry for the flat-surface impulse response. The radar travels in the direction of the x axis at an altitude h above the mean surface spanned by x and y. The Antenna is pointed toward the off-nadir point marked with a red cross (Adapted from Brown (1977)).

waveform being retracked.

3.1 Brown-Hayne's Ocean Model

An analytical model of an open-ocean echo was presented by Brown (1977), and described the returned echo as a function of radar and ocean parameters.

Using the geometry in Figure 3.1, the average backscattered power from a mean flat surface ($P_{fs}(t)$), can be calculated as an integral over the illuminated area (A) containing the carrier wavelength (λ), two-way propagation loss (L_P), antenna gain ($G(\theta,\omega)$) and range (r) to the scattering element (dA) (Equation 3.1).

$$P_{FS}(t) = \frac{\lambda^2}{(4\cdot\pi)^3\cdot L_P}\int_A \frac{\delta(t-2\cdot r/c)\cdot G^2(\theta,\omega)\cdot\sigma^0(\psi,\phi)}{r^4}dA \tag{3.1}$$

Hayne (1980) continued on the Brown formulation, and described the return echo from an ocean surface ($P(t)$) as the convolution of the impulse response of the Earth ($S(t)$), approximated by a smooth sphere, the instrument point target response ($\chi(t)$), and the probability density function of the specular points ($f_{sp}(t)$).

$$P(t) = S(t) * \chi(t) * f_{sp}(t) \tag{3.2}$$

A number of approximations and assumptions have been introduced to reach an expression suitable for implementation in a retracker. Here the commonly used formulation, by Rodriguez (1988), of the three convolved elements is presented.

The impulse response of the mean Earth approximated by a sphere (Equation 3.3), can be expressed as:

$$\begin{aligned} S(t) &= A \cdot e^{-\alpha \cdot t} \cdot I_0 \cdot (\beta \cdot t^{1/2}) \cdot U(t) \\ \alpha &= \frac{ln(4)}{sin^2(\theta/2)} \cdot \frac{c}{h} \cdot \frac{1}{1+h/R} \cdot cos(2 \cdot \xi) \\ \beta &= \frac{ln(4)}{sin^2(\theta/2)} \cdot \left(\frac{c}{h} \cdot \frac{1}{1+h/R} \right)^{1/2} \end{aligned} \tag{3.3}$$

where

I_0 : Modified Bessel function.

$U(t)$: Unit step function.

h : Height above the mean ocean surface.

R : Radius of the Earth.

c : Speed of light.

θ : Antenna beamwidth.

ξ : Off-nadir pointing.

The probability density function describing the specular points:

$$\begin{aligned} f_{sp}(z) &= \frac{1}{(2 \cdot \pi)^{1/2} \cdot \sigma} e^{-\eta^2/2} \left(1 + \frac{\lambda}{6}(\eta^3 - 3\eta) \right) \\ \eta &= \frac{z - z_T}{\sigma} \end{aligned} \tag{3.4}$$

where

σ : Ocean surface standard deviation.

λ : Ocean surface skewness.

z : Height above the mean ocean surface ($z = 0$).

z_T : Tracker bias.

Finally the point target response of the radar can be expressed as a *sinc* function depending on the pulse length ($2T$) and the bandwidth (proportional to a):

$$\chi(t) \sim \frac{sin^2\left((a \cdot t/2) \cdot (T - |t|)\right)}{(a \cdot t/2)^2} \tag{3.5}$$

Assuming that the radar parameters, such as antenna radiation pattern gain, pulse length, etc. are known, it is possible to estimate the ocean parameters through a deconvolution (Rodriguez and Chapman, 1989) and a fitting procedure. Several physical models have been developed by adopting the approach initially suggested by Brown (1977).

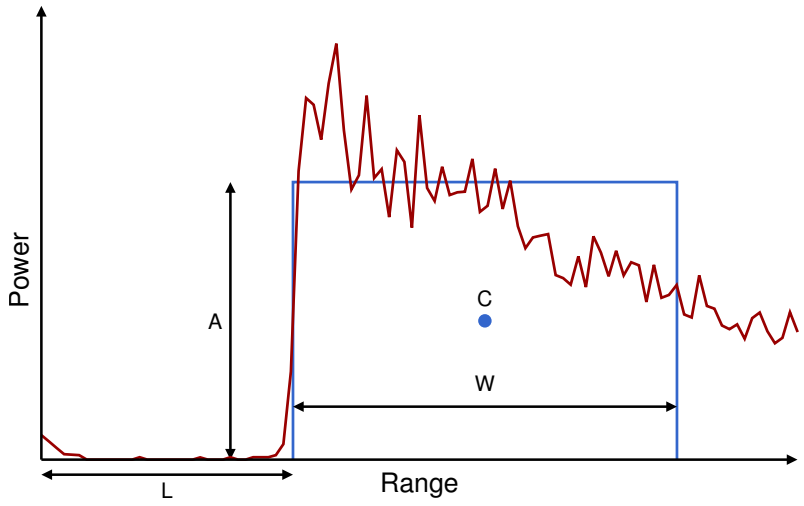

Figure 3.2: OCOG retracker and a typical waveform from conventional altimetry.

3.2 Offset Centre of Gravity (OCOG) Retracker

The OCOG retracker (Wingham et al., 1986) offers a simple and robust retracker based on a purely statistical approach. The OCOG retracker calculates the centre of gravity (C) of the energy in a waveform (excluding aliased samples in the beginning and end of the waveform). The width and amplitude of a rectangle, centred at C, with area equal to the summed power in the waveform, is calculated, see Figure 3.2. From the centre of gravity, and the width of the rectangle, the position of the leading edge can be calculated, see Equation 3.9.

The empirical approach, not related to any physical model, has limited accuracy on the retrieved range. However, due to the robustness and the simplicity of the formulation, the OCOG retracker is widely used, either directly or as an initialization of a more advanced retracker.

$$C = \frac{\sum_n n \cdot P_n^2}{\sum_n P_n^2} \tag{3.6}$$

$$A = \sqrt{\frac{\sum_n P_n^4}{\sum_n P_n^2}} \tag{3.7}$$

$$W = \frac{(\sum_n P_n^2)^2}{\sum_n P_n^4} \tag{3.8}$$

$$L = C - \frac{1}{2} \cdot W \tag{3.9}$$

3.3 Threshold Retracking Algorithm

Davis (1997) proposes a simple approach to obtaining the range over the ice-sheet by estimating the point where the waveform exceeds a chosen threshold. The maximal power in the waveform (A_{max}) is determined, and the thermal noise including any DC bias is found by averaging a number (c) of samples starting at the first unaliased sample (a), see Equa-

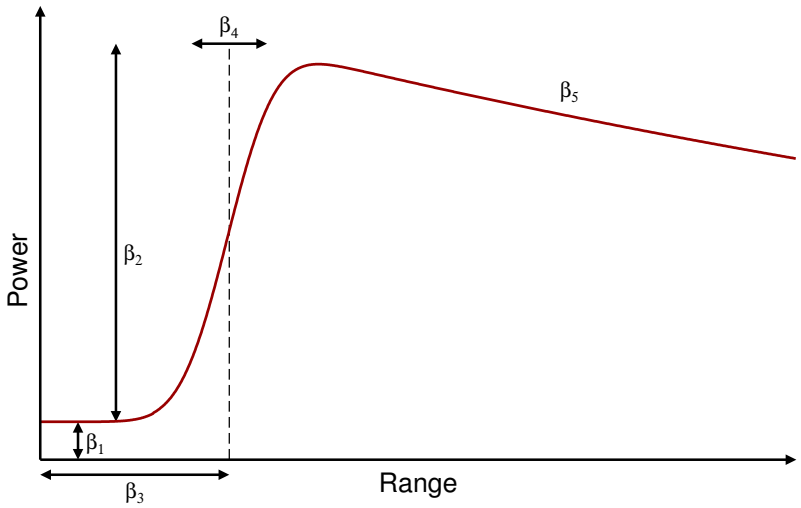

Figure 3.3: An idealized waveform with the five parameters in the Beta retracker overlayed.

tions 3.10 and 3.11.

The threshold coefficient (T_{coeff}) should be chosen with respect to the surface properties (e.g. 50% for areas with dominant surface scatters and 10–20% for areas dominated by volume scattering). The threshold power ($P_{threshold}$) can now be calculated, and the range can be obtained by linearly interpolation between the last sample below and the first sample above the threshold power.

$$A_{max} = max(P_n) \tag{3.10}$$

$$N_{termal} = \frac{1}{c} \sum_{n=a}^{n \leq a+c} P_n \tag{3.11}$$

$$P_{threshold} = N_{termal} + T_{coeff}(A_{max} - N_{termal}) \tag{3.12}$$

$$\tag{3.13}$$

Other variants of the threshold retracker uses the amplitude from the OCOG retracker as the maximal power, or by averaging a number of samples near the end of the leading edge.

3.4 Beta Retracker

The Beta retrackers introduced an empirical function with a shape similar to the Brown-Hayne's ocean model and were constructed to obtain ranges over the inland ice (Martin et al., 1983). The Ice Altrimetry Group at NASA's Goddard Space Flight Centre (GSFC) has continued the development of these retrackers, which are commonly refereed to as the NASA GSFC V4 retracker. The much simpler formulation, compared with the Brown-Hayne's model, allows a simpler fitting procedure, but the parameters are no longer a direct physical property. However, most parameters can be considered a proxy for the properties

in the Brown-Haynes model.

$$P(t) = \beta_1 + \beta_2 \cdot (1 + \beta_5 \cdot Q) \cdot f\left(\frac{t - \beta_3}{\beta_4}\right) \tag{3.14}$$

where

$$f(z) = \frac{1}{\sqrt{2\pi}} \cdot \int_{-\infty}^{z} e^{-\frac{q^2}{2}} dq \tag{3.15}$$

$$Q = \begin{cases} 0 & \text{if } t < \beta_3 + \frac{1}{2} \cdot \beta_4 \\ t - \left(\beta_2 + \frac{1}{2} \cdot \beta_4\right) & \text{if } n \geq \beta_3 + \frac{1}{2} \cdot \beta_4 \end{cases} \tag{3.16}$$

The five estimated parameters in Equation 3.14, and shown in Figure 3.3, are:

β_1 : Thermal noise including DC bias.

β_2 : Return power.

β_3 : Mid point on the leading edge.

β_4 : Leading edge rise time.

β_5 : Slope of trailing edge.

3.4.1 Five Parameter Beta Retracker with Exponential Tail

In a later revision of the Beta retracker the trailing edge was replaced by a exponential decaying function (Deng and Featherstone, 2006; Zwally et al., 1990). The fast decaying trailing edge allowed a better retracking over areas with high beam attenuation beyond the pulse limited footprint (e.g. sea-ice).

The exponential decaying trailing edge can also be applied over areas without high beam attenuation, and has therefore replaced the original five parameter Beta retracker.

$$P(t) = \beta_1 + \beta_2 \cdot e^{-\beta_5 \cdot Q} \cdot f\left(\frac{t - \beta_3}{\beta_4}\right) \tag{3.17}$$

where

$$f(z) = \frac{1}{\sqrt{2\pi}} \cdot \int_{-\infty}^{z} e^{-\frac{q^2}{2}} dq \tag{3.18}$$

$$Q = \begin{cases} 0 & \text{if } t < \beta_3 + k \cdot \beta_4 \\ t - (\beta_3 + k \cdot \beta_4) & \text{if } t \geq \beta_3 + k \cdot \beta_4 \end{cases} \tag{3.19}$$

3.4.2 Double Ramp Beta Retracker

In the marginal zone of the inland ice the topography will often have a high variability, and the echoes will therefore not only represent one but several surfaces at different elevations within the footprint. The nine parameter Beta retracker was introduced to minimize this problem by allowing the fit of two surfaces at different elevations, see Figure 3.4 and Equation 3.20.

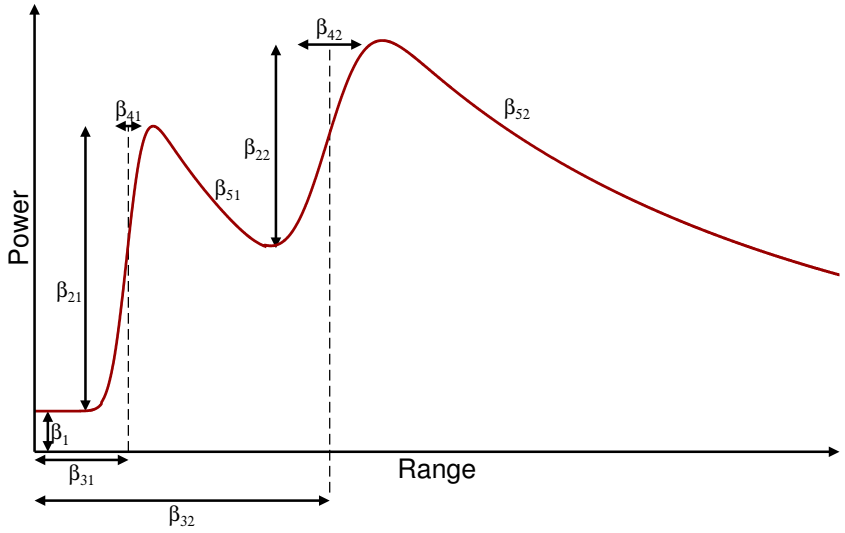

Figure 3.4: An idealized waveform containing returns from two surfaces at different elevations, with the nine parameters in the Beta retracker.

Inspection of Equation 3.20 and 3.17 reveals that the nine parameter Beta retracker is composed of two five parameter Beta retrackers with a common thermal noise parameter.

$$P(t) = \beta_1 + \sum_{i=1}^{2} \beta_{2i} \cdot e^{-\beta_{5i} \cdot Q} \cdot f\left(\frac{t - \beta_{3i}}{\beta_{4i}}\right) \tag{3.20}$$

where

$$f(z) = \frac{1}{\sqrt{2\pi}} \cdot \int_{-\infty}^{z} e^{-\frac{q^2}{2}} dq \tag{3.21}$$

$$Q_i = \begin{cases} 0 & \text{if } t < \beta_{3i} + k \cdot \beta_i 4 \\ t - (\beta_{3i} + k \cdot \beta_{4i}) & \text{if } t \geq \beta_{3i} + k \cdot \beta_{4i} \end{cases} \tag{3.22}$$

3.5 CryoSat Retracker

Wingham et al. (2006) suggest an empirical retracker with six paramters designed to replicate the theoretical model of a multi-looked SAR altimeter echo. The retracker is composed of five different segments describing the various domains of the echo from the leading toe first in the echo, to the trailing edge last in the echo, see Equation 3.24.

$$P(t; a, \sigma, t_0, c, \alpha, n) = a \cdot e^{-h^2\left(\frac{t}{t_p}\right)} \tag{3.23}$$

$$h(s) = \begin{cases} \frac{1}{10}(s - s_0) - 2.5 + \frac{n \cdot \sigma}{10} & \text{if } s < s_0 - n \cdot \sigma \\ b_0 + b_1\left(s - s_0 - \frac{\sigma}{2}\right) + b_2\left(s - s_0 - \frac{\sigma}{2}\right)^2 + b_3\left(s - s_0 - \frac{\sigma}{2}\right)^3 & \text{if } s_0 - n \cdot \sigma < s < s_0 - \frac{\sigma}{10} \\ \frac{1}{\sigma}\left(s - s_0 - \frac{\sigma}{2}\right) & \text{if } s_0 - \frac{\sigma}{10} < s < s_0 + \frac{\sigma}{2} \\ \frac{1}{\sigma}\left(s - s_0 - \frac{\sigma}{2}\right) + a_2\left(s - s_0 - \frac{\sigma}{2}\right)^2 + a_3\left(s - s_0 - \frac{\sigma}{2}\right)^3 & \text{if } s_0 + \frac{\sigma}{2} < s < s_0 + 2\sigma \\ -log^{\frac{1}{2}}\left[\frac{c \cdot e^{\alpha(s - s_0)}}{\sqrt{a(s - s_0)}}\right] & \text{if } s_0 + 2\sigma < s \end{cases} \tag{3.24}$$

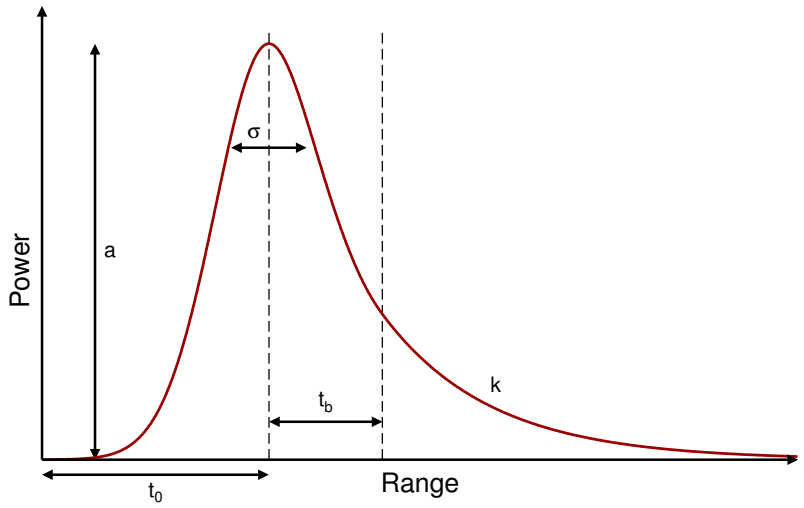

Figure 3.5: The simplyfied CryoSat retracker overlayed with the fitting parameters.

In Equation 3.24 a number of parameters are found, which are not part of the fitted parameters. These parameters can be found by demanding that $h(s)$ and its first derivative are continuous. Some further constrains are introduced on the fit parameters to keep the empirical model within the bound of the theoretical model it replicates:

- $a_{max}/100 < a < 10 \cdot a_{max}$[1]
- $2 < \sigma < 30$
- $-0.1 < \alpha < 0.1$
- $2 < n < 10$
- $0.01 \cdot a_{max} < c < 99 \cdot a_{max}$

3.6 Simplified CryoSat Retracker

A simplified empirical expression for the SAR altimeter echo was derived by Giles et al. (2007) following the method suggested by Wingham et al. (2006). Here the waveform is composed of three segments; a Gaussian leading edge, an exponential decaying trailing edge, and a polynomial function to connect the leading and trailing edge. The simplified expression also contains parameters (i.e. a_2 and a_3), which can be determined by demanding that $f(t)$ and its first derivative are continuous.

$$P_r(t;a,t_0,k,\sigma) = a \cdot e^{-f^2(t)} \tag{3.25}$$

$$f(t) = \begin{cases} \frac{t-t_0}{\sigma} & \text{if } t < t_0 \\ \frac{1}{\sigma}(t-t_0) + a_2(t-t_0)^2 + a_3(t-t_0)^3 & \text{if } t_0 < t < t_0 + t_b \\ \sqrt{k \cdot (t-t_0)} & \text{if } t_0 + t_b < t \end{cases} \tag{3.26}$$

[1] a_{max} is the maximal power found in the echo.

where

a : Maximal return amplitude.

t_0 : Time of maximal return amplitude.

k : Decay of trailing edge.

σ : Width of leading edge.

t_b : Distance between end of leading edge and start of trailing edge.

3.7 SAMOSA Ocean Retracker

The SAMOSA retracker is currently being developed, implemented and refined under the ESA project SAMOSA, and its continuation SAMOSA2. The work is carried out in continuation of the SAMOSA project where theory and models have been developed to exploit SAR altimeter data from CryoSat-2, and the upcoming Sentinel-3 for ocean and water applications (Cotton, 2010).

The SAMOSA retracker uses the Brown approach to describe the returned waveform from the Doppler/pulse limited footprint (Martin-Puig and Ruffini, 2009; Martin-Puig et al., 2009). By considering the multi-looking, a numerical model was created, and later an analytical expression was derived and implemented in MATLAB (Gommenginger and Srokosz, 2009). Because it is a physically based model it can include a number of other parameters such as e.g. significant wave height, σ_0, and antenna mispointing.

The SAMOSA retracker is considered proprietary information, and is therefore not reproduced here. For comparison a CryoSat-2 SAR profile has been retracked using the SAMOSA retracker (courtesy of Christine Gommenginger, National Oceanography Center, Southampton). Furthermore, an investigation of the SAMOSA retracker performance was carried out using ASIRAS HAM data from the Fram Strait (Stenseng and Gommenginger, 2011).

3.8 Implementation of Retrackers

The OCOG and the threshold retrackers were implemented in C++ together with the functions to read the L1b data products (Advanced Computer Systems, 2009) from the CryoSat-2 processing center. Furthermore, the three Beta retrackers and the simplified CryoSat retracker were implemented using the open source LevMar (Lourakis, 2009) implementation of the Levenberg-Marquardt non-linear least squares algorithm (Marquardt, 1963).

To obtain the elevation of the retracked point the total range to a known position in the waveform is needed. This range can be determined from the two-way delay time and by applying geophysical corrections provided by the L1b data products.

Inspection of the Beta retrackers reveals an integral which must be computed as part of the models. Fortunately, the integral can be solved analytical and this leads to the error

function which is available in C++, see Equation 3.27.

$$\begin{aligned} f(z) &= \frac{1}{\sqrt{2\pi}} \cdot \int_{-\infty}^{z} e^{-\frac{q^2}{2}} dq \\ &= \frac{1}{2}(\mathrm{erf}(\sqrt{1/2} \cdot z) - 1) \end{aligned} \tag{3.27}$$

The two variables a_2 and a_3 in the simplified CryoSat retracker were determined by demanding that the function and its first derivative are continuous, see Equation 3.29 and 3.28. The t_b parameter, determining the length of the connecting polynomial, must be estimated beforehand and given as a fixed parameter during processing.

$$a_3 = \frac{-\sqrt{k \cdot t_b} \cdot 2 \cdot \sigma / t_b + 2}{(t_b^2 + 2 \cdot t_0^2 + 2 \cdot t_0 \cdot t_b) \cdot (3 - 2 \cdot \sigma)} \tag{3.28}$$

$$a_2 = \frac{\sqrt{k \cdot t_b}}{t_b^2} - \frac{1}{\sigma \cdot t_b} - a_3 \cdot t_b \tag{3.29}$$

All waveforms are analysed to determine the thermal noise, and any DC bias before the OCOG retracker is applied to obtain some basic information. The range is then estimated with the threshold retracker. In the next step, the estimated parameters from the OCOG retracker and the threshold retracker are used to initialize the retrackers, where parameters are fitted using the Levenberg-Marquardt routine.

3.9 Evaluation and Comparison of Retrackers

To compare the implemented retrackers a CryoSat-2 SAR profile from September 26, 2010 in the Davis Strait was processed with the developed software and retracked at the National Oceanography Center by Christine Gommenginger using the SAMOSA retracker. The DTU10 mean sea surface (Andersen and Knudsen, 2009) was subtracted from the estimated heights to obtain a constant offset containing retracker bias, orbit errors, and sea state added with a varying component consisting of retracker performance, noise in data, and errors in the mean sea surface.

Figure 3.6 shows a large bias in all the retracked results of about -10 m. The large bias could be caused by instrument delays, erroneous geophysical corrections in the datafile or erroneous application of the supplied corrections. The source of the bias is not investigated as this is a commissioning phase dataset, where geophysical corrections and orbits are preliminary, and where instrument corrections are not applied.

The comparison of the estimated heights also reveals an offset between the different retrackers. This is caused by their individual definition of the surface range parameter, as described above. The SAMOSA retracker is based on a physical model describing the SAR waveform based on the state of the observed ocean. The height derived from this retracker could be argued as the best estimate for the true surface height. The mean difference from the mean sea surface and the standard deviation of the mean was calculated for the five retrackers and are presented in Table 3.1. From Table 3.1 it can be seen that the SAMOSA retracker is able to fit 97% of the echoes, the Simple CryoSat retracker 96%, and the five parameter Beta retracker with exponential tail obtains a fit for 93% of the echoes.

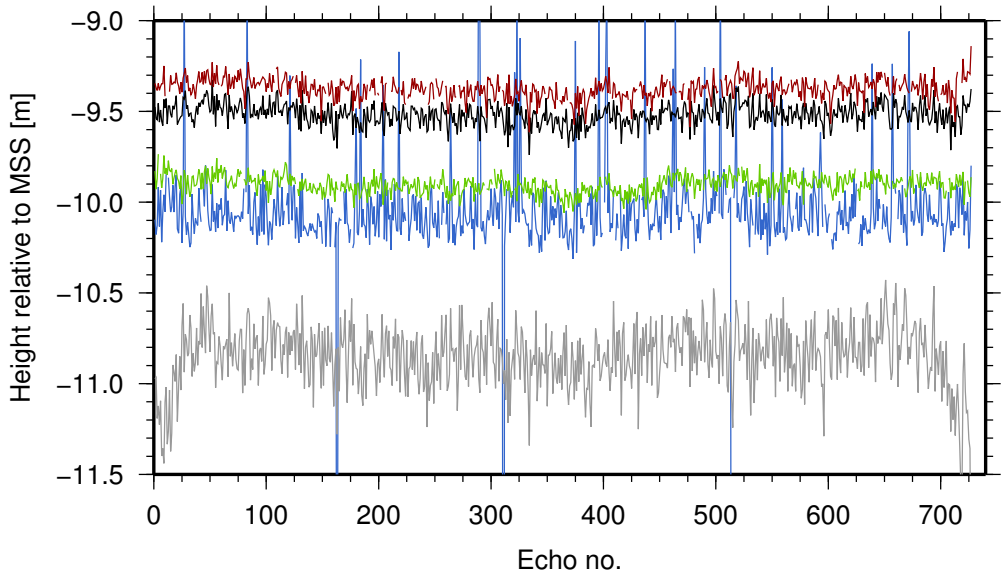

Figure 3.6: Height relative to the mean sea surface derived from a CryoSat-2 SAR profile in the Davis Strait using OCOG (grey), 80% threshold (black), five parameter Beta retracker with exponential tail (red), the simplified CryoSat retracker (blue), and the SAMOSA retracker (green).

Retracker	Mean	Std. dev.	Count
OCOG	-10.848 m	0.1796 m	727
80% threshold	-9.517 m	0.0612 m	727
Simplified CryoSat	-10.056 m	0.4302 m	698
Beta with exp tail	-9.372 m	0.0563 m	686
SAMOSA	-9.903 m	0.0506 m	708

Table 3.1: Mean height difference from the mean sea surface and standard deviation of the mean for the four retrackers.

Based on the standard deviations in Table 3.1 it can be concluded that the SAMOSA retracker is the most consistent, followed closely by the five parameter Beta retracker with exponential tail and the 80% threshold retracker. By comparison the OCOG and the Simplified CryoSat retracker have a factor 2 to 5 higher standard deviation. The high standard deviation on the Simplified CryoSat retracker is caused by a number of spikes, where the retracker estimates an erroneous range.

A number of tests which were performed on the Simple CryoSat retracker revealed that the retracker is very sensitive to the choice of t_b, and initial values for the fitting parameters. Further work on the Simple CryoSat retracker is needed to stabilize its performance and an automated tuning of the initial parameters has not yet been successful.

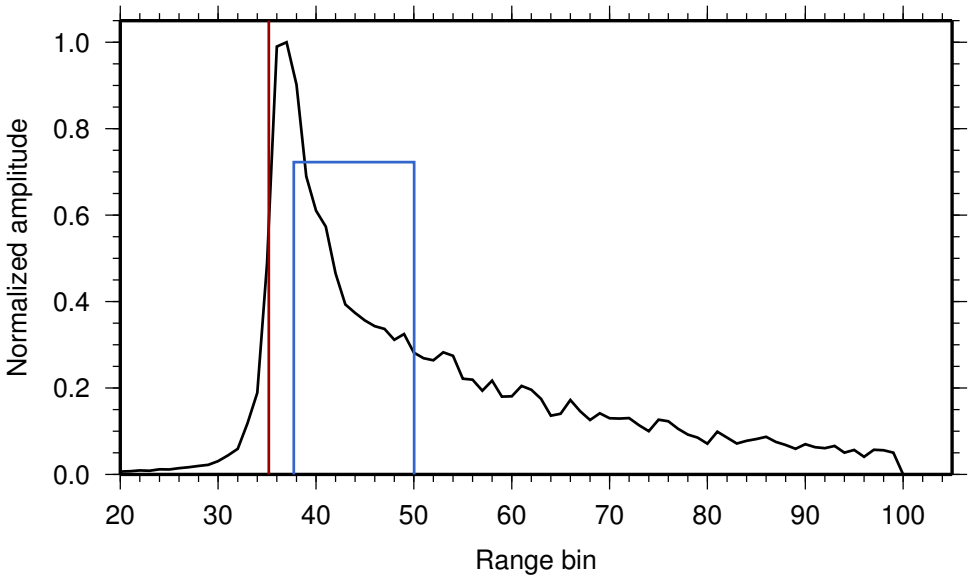

Figure 3.7: Echo number 100 from the Davis Strait profile overlayed with the position of the 80% threshold retracker (red) and the box determined with the OCOG retracker(blue).

3.9.1 Waveform and Retracker Examples

Waveform number 100 was chosen to further illustrate the performance of the SAMOSA retracker and the implemented retrackers. The shape of the chosen waveform is typical for most waveforms in the profile, and can therefore be considered representative for ocean waveforms under similar ocean conditions.

Figure 3.7 shows how the OCOG retracker (blue) misplaces the tracking point (left edge of the blue box). The sharp peak in the first part of the echo has not enough weight to pull the center of gravity away from the slow decaying last part of the tail. This behaviour is expected as the OCOG retracker is developed to handle conventional altimeter echoes, with a steep rising edge followed by a decaying plateau.

The misplacement of the OCOG tracking point is overcome by combining it with the 80% threshold retracker (red), where the tracking point is placed on the leading edge.

The Simple CryoSat retracker fits a function to the waveform, and thereby allows a direct comparison between the shape of the waveform and the model, see Figure 3.8. Except for the toe at the beginning of the leading edge, the leading edge and the first steep part of the trailing edge is well captured by the fitted model. The length (t_b) of the connecting polynomial appears too short, whereby the exponential decaying tail becomes too steep. A series of tests with a longer t_b has been carried out, but lead to an unstable performance of the retracker.

The five parameter Beta retracker with exponential tail also fits a function to the waveform like the Simple CryoSat retracker, see Figure 3.9. The performance in the first part of the leading edge and the last part of the trailing edge is comparable to that of the Simple CryoSat retracker. The sharp peak at the end of the leading edge is, as expected, captured by the five parameter Beta retracker.

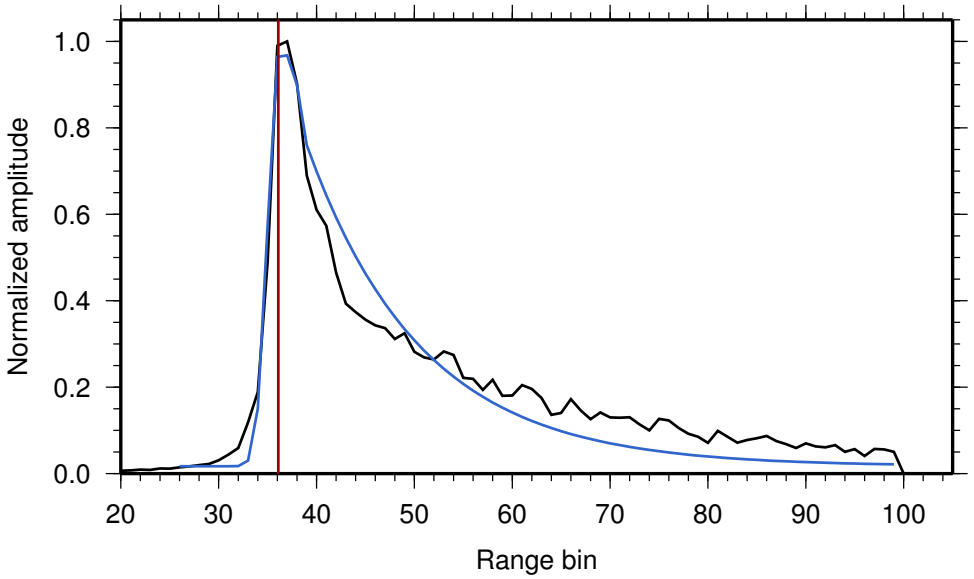

(a) Waveform (black), fitted model (blue) and tracking point (red).

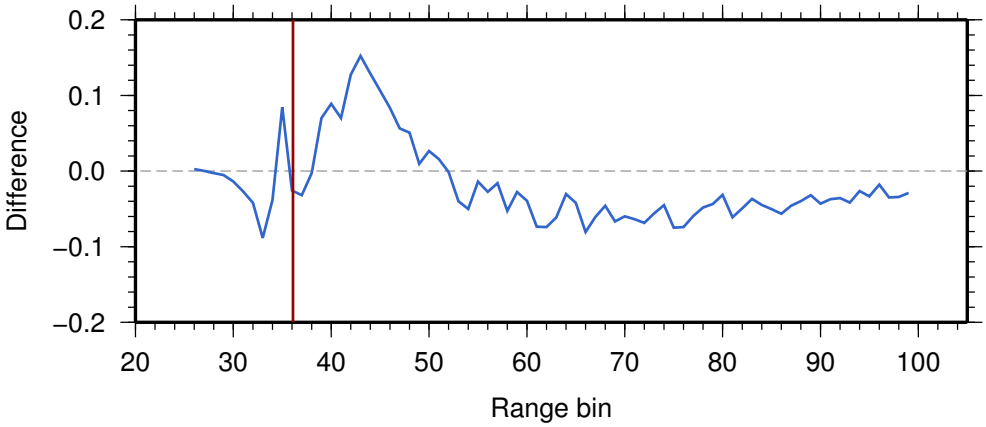

(b) Difference between echo and model (blue). Zero difference (dashed grey) and the t_0 position (red) is added for reference.

Figure 3.8: Echo number 100 from the Davis Strait profile plotted with the fitted Simple CryoSat retracker model.

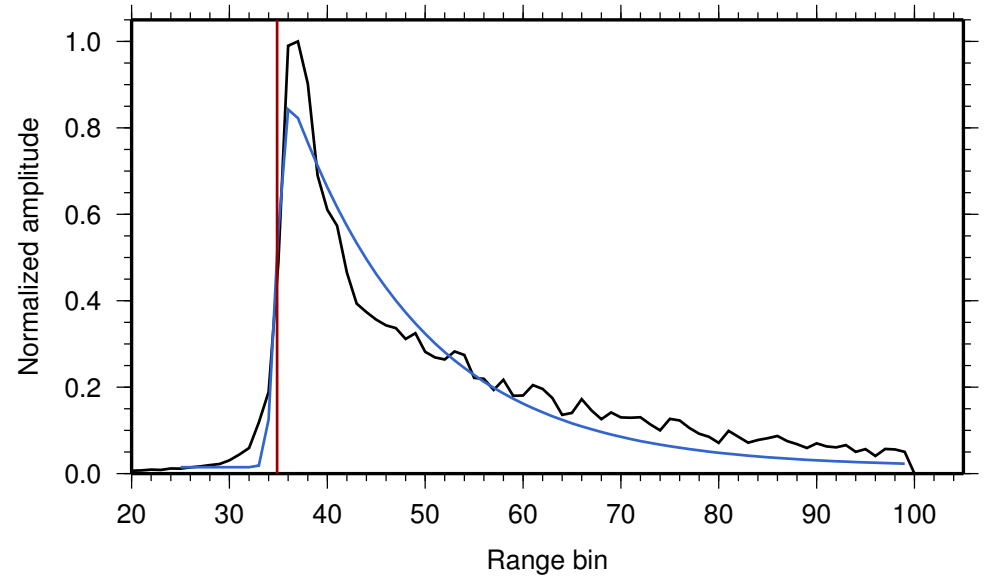

(a) Waveform (black), fitted model (blue) and tracking point (red).

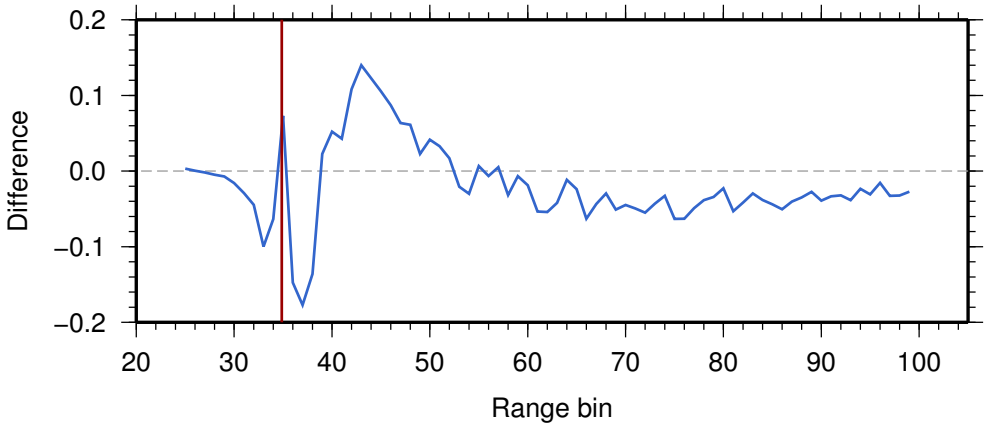

(b) Difference between echo and model (blue). Zero difference (dashed grey) and the β_3 position (red) is shown for reference.

Figure 3.9: Echo number 100 from the Davis Strait profile plotted with the fitted five parameter Beta retracker.

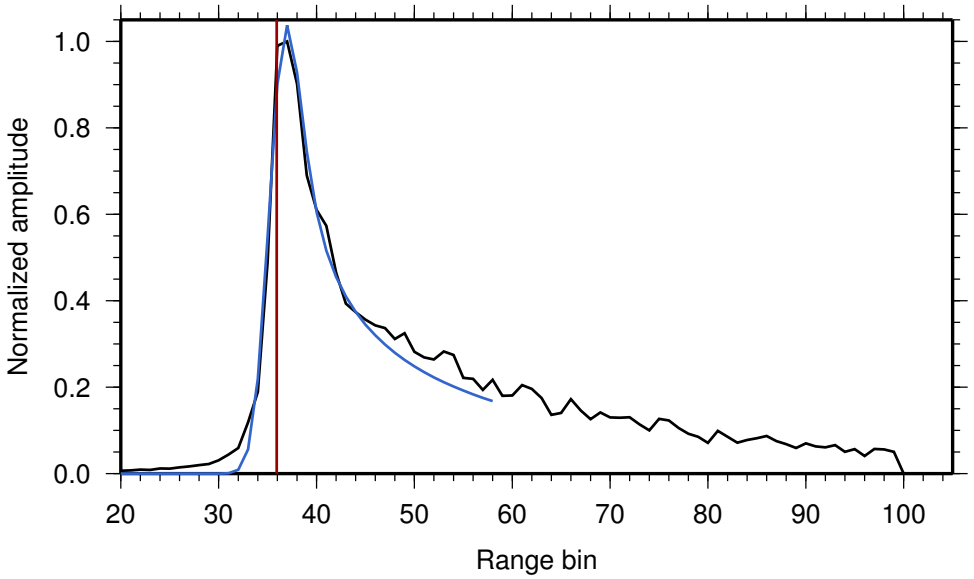

(a) Waveform (black), fitted model (blue) and tracking point (red).

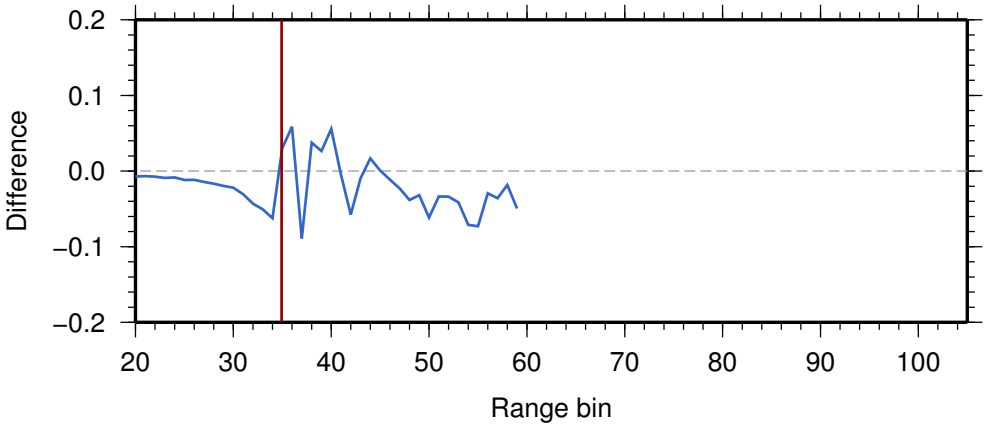

(b) Difference between echo and model (blue). Zero difference (dashed grey) and the tracking position (red) is shown for reference.

Figure 3.10: Echo number 100 from the Davis Strait profile plotted with the fitted SAMOSA retracker.

The complex physical model build into the SAMOSA retracker enables it to obtain an accurate fit of the entire echo and will furthermore estimate ocean state parameters such as the significant wave height.

3.9.2 Evaluations of Retrackers

The examples shown in Figures 3.8, 3.9, and 3.10 clearly favours the SAMOSA retracker as it captures the shape of the waveform very accurately and returns a successful fit for 97% of the echoes. However, the simplicity and ease of implementation makes the five parameter Beta retracker with exponential tail a good choice for preliminary investigations where only the surface height is of interest. The five parameter Beta retracker with exponential tail is found to give an acceptable fit to the waveform as well as having a stable performance.

From Table 3.1 it is seen that the 80% threshold retracker estimates the surface almost as accurately as the five parameter Beta retracker. In addition the 80% threshold retracker obtains a height estimate for all waveforms, whereas the five parameter Beta retracker rejects around 6% of the waveforms.

3.10 Summary

The author has developed a software suite, consisting of four retrackers, for retracking of SAR altimeter echoes. The software suite has been used on real CryoSat-2 SAR data from the Davis Strait to obtain the first test of different retracker approaches, and has been compared with the state of the art SAMOSA retracker developed for CryoSat-2 ocean waveforms.

The simple CryoSat retracker was found to be highly sensitive to the t_b and therefore unstable. Despite the instability the retracker was able to obtain a fit for 96% of the waveforms, but the standard deviation of the mean was 43 cm. The OCOG and 80% threshold retrackers do not attempt to fit a function and will return a value for 100% of the waveforms regardless of their shape. The standard deviation of the OCOG and 80% threshold retrackers were 18 cm and 6 cm respectively. The five parameter beta retracker with exponential tail has a slightly smaller standard deviation of 5.6 cm and is capable of obtaining a fit for 93%. The SAMOSA retracker exhibits the best performance by obtaining a fit for 97% of the waveforms with a standard deviation of 5 cm.

Chapter 4

Detection of Annual Layers in Firn on the Greenland Ice Sheet

Radar altimeters have been used to map various surface heights since the first radar altimeter satellites were launched more than 30 years ago. The majority of the radar altimeter missions have focused on ocean applications such as ocean tide, sea-surface height, wave height, and wind speed.

The long time series and the high availability of radar altimetry data have been widely used to estimate the rate of elevation change over the ice sheets (e.g. Davis et al. (2000)). However, the large footprint of the conventional pulse limited radar altimeters is sensitive to surface slopes, making the height measurements in the marginal zone of the ice sheets unreliable (Brenner et al., 2007). The SAR altimeters small along-track footprint promises a better precision in the marginal zone, which in the case of CryoSat-2 is improved further by the cross-track interferometry available in SARin mode.

The radar pulse penetrates into the snow-pack making the surface height estimate challenging, as strong subsurface reflectors can dominate the waveform. The retracker must therefore take great care in separating a potential weak surface signal from a strong subsurface reflector. This penetration is related to the snow and firn properties and will therefore vary not only from place to place but also from season to season (Lacroix et al., 2008).

Care must be taken when converting the observed volume changes to mass changes, as other processes than mass changes will affect the volume. Part of the observed volume change is caused by compaction of the firn (Sørensen et al., 2010a) and by changes in the firn properties and thereby the reflecting horizon (Zwally et al., 2005).

The following sections present a number of investigations of annual layers and firn properties, primarily in the dry snow zone of the Greenland Ice Sheet using airborne SAR altimetry data. The presented methods have been developed during the PhD by the author and utilizes airborne ASIRAS SAR altimetry data. The methods are compared with in situ density profiles based on Neutron probe measurements (Morris and Cooper, 2003) carried out by Elizabeth M. Morris from Scott Polar Research Institute and a firn compaction model developed by Sebastian B. Simonsen, Centre for Ice and Climate, NBI, University of Copenhagen.

4.1 Radar Propagation in Firn

When a radar pulse is emitted from a satellite it travels at the speed of light through the vacuum until the pulse enters the atmosphere, which has a refractive index (n) slightly above one and therefore lowers the propagation speed. For most airborne radars the correction to the propagation speed, induced by the refractive index of the atmosphere, is negligible due to the short travel time. This correction is much smaller than the range resolution and other errors (e.g. positioning error).

The rapid change in the refractivity[1] (N) at the air/snow interface will refract the radar pulse, returning some energy towards the radar and transmitting the remaining energy into the snow pack. As the radar energy travels through the snow pack it is further refracted by density variations and ice inclusions, but it is also scattered and absorbed by the firn.

Mätzler and Wegmüller (1987) estimated the dielectric properties of ice over a frequency range from 2GHz to 100GHz. They found that the real part of the complex relative dielectric permittivity (ϵ_{ice}) has a weak dependence of the temperature (T in °C).

$$\epsilon_{ice} = 3.1884 + 0.00091 \cdot T \tag{4.1}$$

Ignoring small effects of anisotropy and acknowledging that the imaginary part is much smaller than the real part, the relationship between the complex relative dielectric permittivity and the complex relative refractive index (n_{ice}) can be expressed as:

$$\epsilon_{ice} = n_{ice}^2 \tag{4.2}$$

Assuming that firn can be considered to be a heterogeneous mixture of air and ice with a volume fraction (q_{firn}) proportional to the firn density, the relative permittivity of firn (ϵ_{firn}) can then be calculated as a function of the volume fraction and the relative permittivity of ice. (Looyenga, 1965).

$$q_{firn} = \frac{\rho_{firn}}{\rho_{ice}} \tag{4.3}$$

$$\epsilon_{firn} = \left(1 + q_{firn} \cdot \left(\epsilon_{ice}^{1/3} - 1\right)\right)^3 \tag{4.4}$$

Using Equations 4.1 to 4.4 it is possible to derive the refractive index of firn, and thus the propagation speed of a radar pulse, as a function of firn density and temperature.

$$n_{firn} = \left(1 + \frac{\rho_{firn}}{\rho_{ice}} \cdot \left((3.1884 + 0.00091 \cdot T)^{1/3} - 1\right)\right)^{3/2} \tag{4.5}$$

4.2 Detection of Annual Layers in Firn

This section will elaborate and expand on the method and results presented in Stenseng et al. (2011) (included in Appendix A.1).

Earlier studies (de la Peña et al., 2010; Hawley et al., 2006; Helm et al., 2007; Leuschen and Raney, 2005) have reported the ability to detect internal annual layering in the snow

[1] The refractivity is the refractive index minus one ($N = n - 1$). Note that in some literature the refractivity is multiplied by 10^6 ($N = (n-1) \cdot 10^6$).

pack over the Greenland Ice Sheet using SAR altrimetry data. Common to these studies is an averaging of a number of waveforms before attempting to identify peaks in the return power.

The radar reflections are believed to arise from the sudden change in firn properties when moving from the dense winter snow and down to the less dense autumn hoar where also a change in crystal structure is seen (de la Peña et al., 2010). A closer inspection of Figure 4.8 supports this assumption as the detection peak in most cases is found just below the high density peak associated with the winter snow. For mass balance studies this is an advantage as the detected layers will mark the end of ablation and start of accumulation which is the commonly used change of epoch.

The new method described in Stenseng et al. (2011) detects peaks in the return power in each waveform before any averaging is done. First a common reference height, i.e. the surface, for all waveforms must be obtained. The air/snow interface is determined using the OCOG retracker on the individual waveforms before smoothing. The shape of the ASIRAS waveforms collected over the Greenland Ice Sheet is very similar to conventional altimetry over ocean, and the OCOG retracker was found to give stable estimates of the air/snow interface. Then the part of the waveform below the snow surface is corrected for the slower propagation using Equation 4.5 and a simple density linear increasing profile.

Second, a number of waveforms along a section of approximately 1 km are collected and aligned at the surface before detections in the collected waveforms are counted in 2 cm depth intervals. The number of detections in a chosen depth interval is divided by the number of waveforms in the collection to obtain the probability of detecting a peak in each depth interval.

A Gaussian is then fitted to each layer probability peak giving the mean depth, standard deviation on the estimated depth and peak probability of detecting the layers. Finally, each layer probability peak is integrated to obtain the accumulated probability of detecting a peak belonging to the layer. The standard deviation of the fitted Gaussians is between 1 cm and 15 cm, with an average standard deviation of 7 cm in the dry snow zone. In the percolation zone the standard deviation of the fitted Gaussians is between 3 cm and 1.2 m, with and average standard deviation of 15 cm

Figure 4.1 shows a subset of 11 waveforms with the detected peaks marked with red next to the detection probability for all 401 waveforms in the group. The airborne ASIRAS data was collected on April 29 2006 in the dry snow zone of the Greenland Ice Sheet at T41 on the EGIG line near the ice divide (see Figure 2.13). The individual waveforms are plotted together with the mean depth and two times the standard deviation of the detected layer interfaces. It should be noted that the topmost peak in the figure is associated with the peak found at the end of the leading edge and thus is part of the surface return. It is also seen that the probability of detecting a layer does not decay with depth, and thereby layers can be detected in the entire range of the radar data. In the investigated dataset the limiting factor is therefore the sampling window used by the radar.

4.2.1 Detection of Layers in CryoVEx 2006 and 2008 Data

The described method has been applied to 2006 and 2008 ASIRAS data from an overflight of the EGIG line (Figure 4.2) and a profile in north-west Greenland in 2008 (Figure 4.6). In the EGIG profiles it is clearly seen how the detection of the deeper layers becomes ambiguous when approaching the percolation zone (i.e. west of -44° and east of -32°). In the perco-

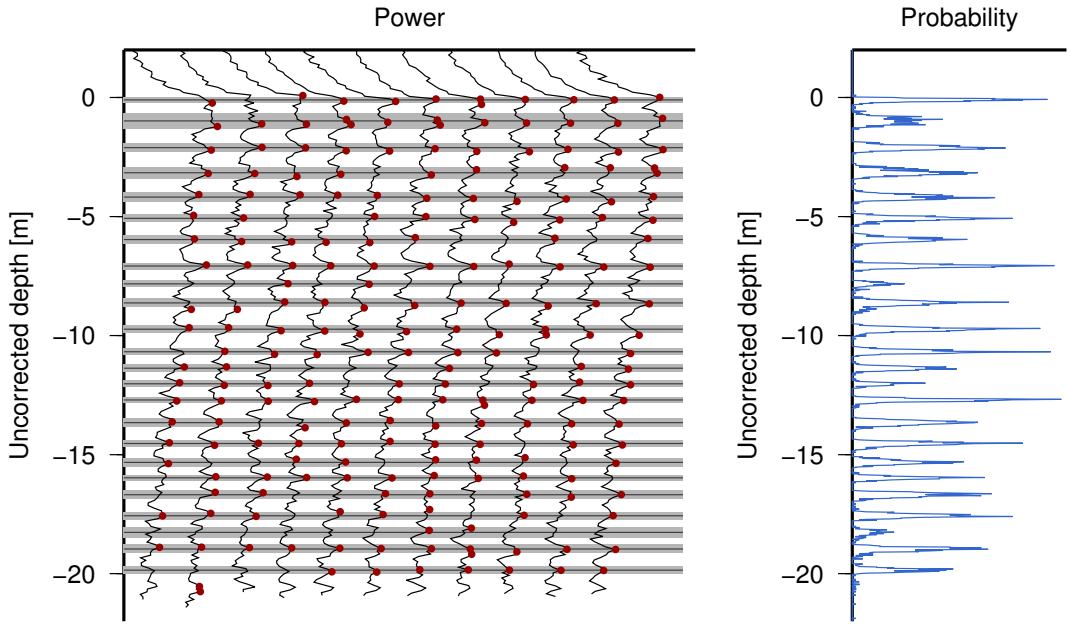

Figure 4.1: A subset of individual waveforms (black) from the dry snow zone, with detected peaks marked in red (left) and the probability of detecting a peak (right) in all waveforms. At this stage the depth is not corrected for the slower propagation speed in firn. The horizontal dark grey lines indicates the mean depth of a layer and the light grey area indicates ± 2 standard deviation.

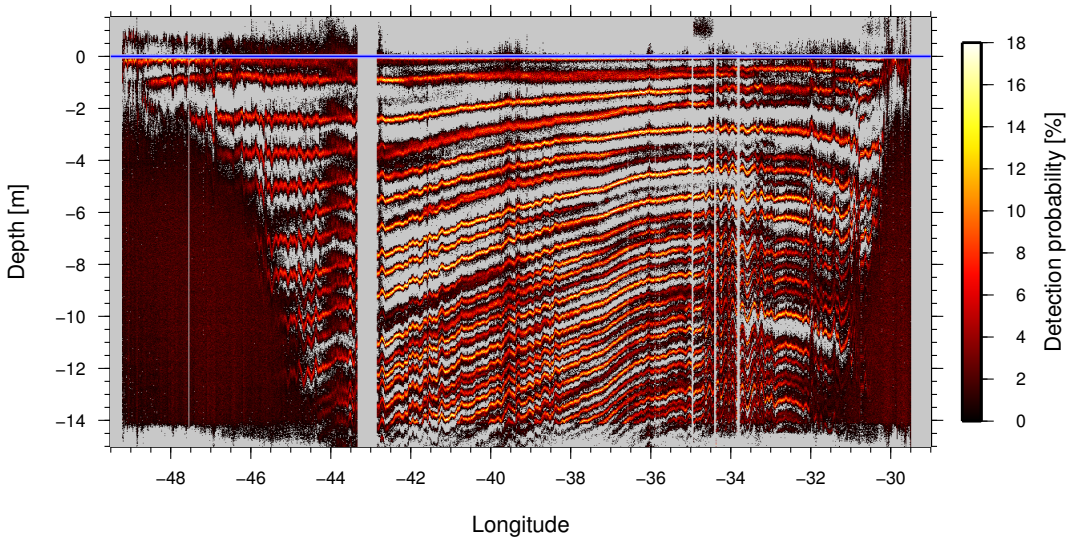

(a) Layers detected along the EGIG line using the 2006 dataset.

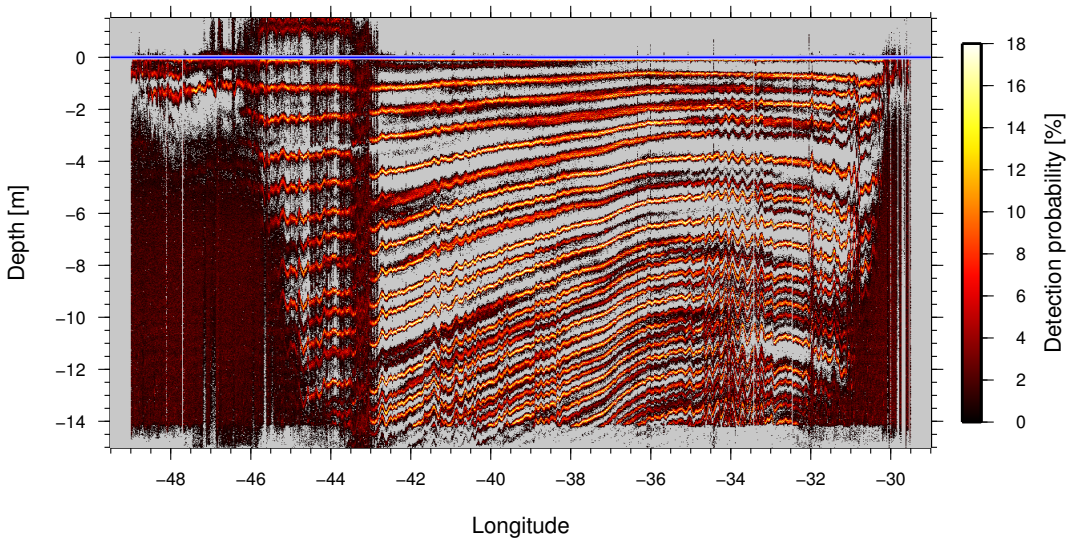

(b) Layers detected along the EGIG line using the 2008 dataset.

Figure 4.2: Layer detection probability in colour coding along the EGIG line as function of depth in 2006 (a) and 2008 (b). Gray indicates zero peak detections or missing data and the blue line marks the surface.

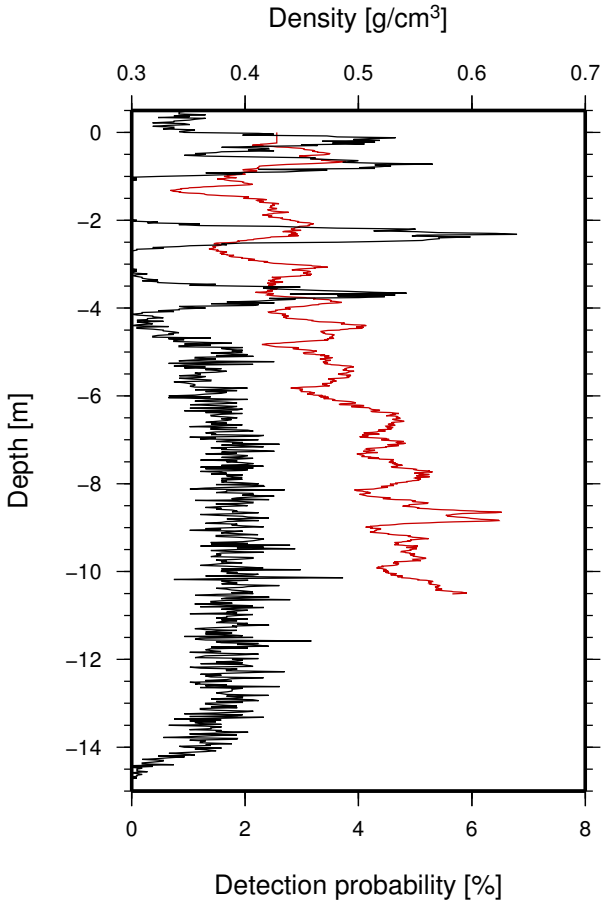

Figure 4.3: Relationship between layer detection probability and layer density at site T9 in the percolation zone observed in spring 2006. The probability (lower axis) for detecting a peak in ASIRAS data at a given depth relative to the surface (black) and the density (upper axis) as function of depth derived from N-Probe observations (red). From Stenseng et al. (2011).

lation zone surface melt and refrozen melt water masks the deeper layers as described in Stenseng et al. (2011), see also Figure 4.3.

When comparing the layer detection in Figure 4.2 with the surface slope and the standard deviation on the mean surface elevation in Figure 4.4, a clear correlation is seen. Not surprisingly, the large changes in surface slopes at -41° and -34° give rise to an increase in the standard deviation. The variation in surface slope at these positions also affects the thickness of the detected layers which is in agreement with the findings of Hamilton (2004).

The statistics from 2006 and 2008 obtained at a fixed location is shown in Figure 4.5. It is seen that the statistical properties, particular the integrated probability and maximal probability, of the of the detected layer is conserved in the two dataset indicating that these reflect physical properties of the reflecting layer in the firn. Furthermore, the statistical properties can be used to identify a layer, thereby allowing a more reliable tracing of a selected layer over long distances.

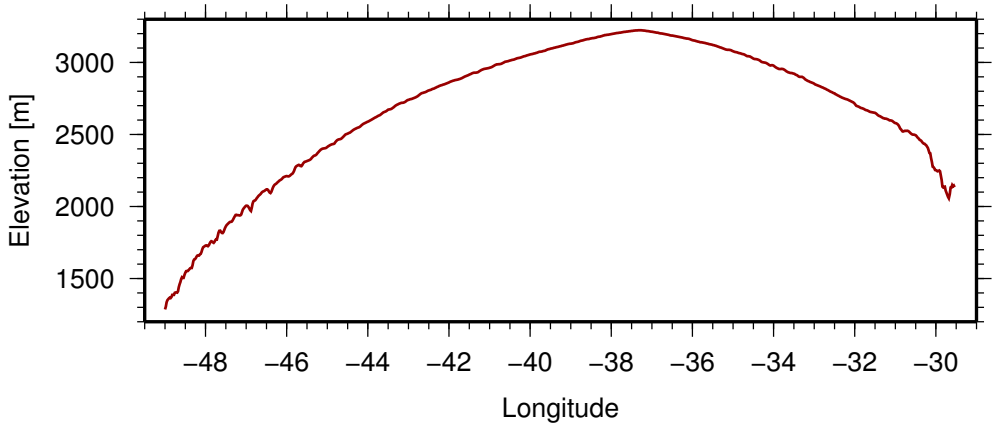

(a) Mean ellipsoidal surface elevation.

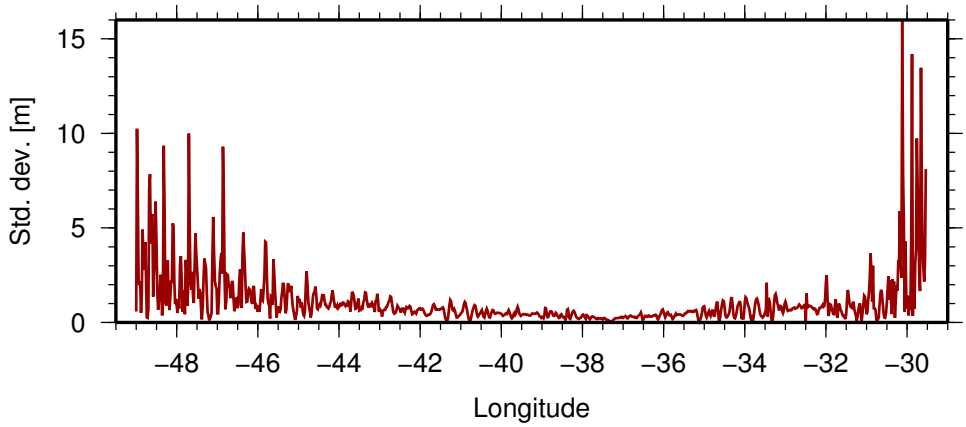

(b) Standard deviation of the mean elevation.

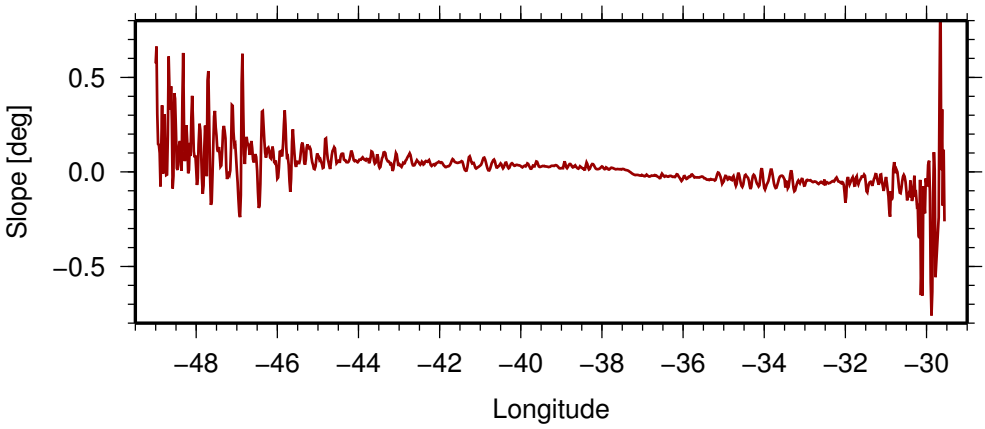

(c) Surface slope along the profile.

Figure 4.4: Surface elevation (a), standard deviation of the elevation (b) and surface slope (c) derived from 2008 ASIRAS data along the EGIG line.

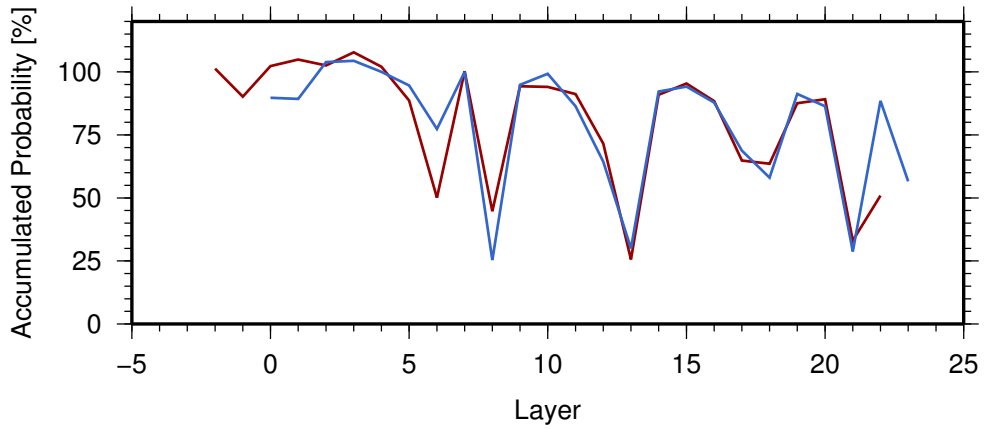

(a) The accumulated probability of detecting a specific layer.

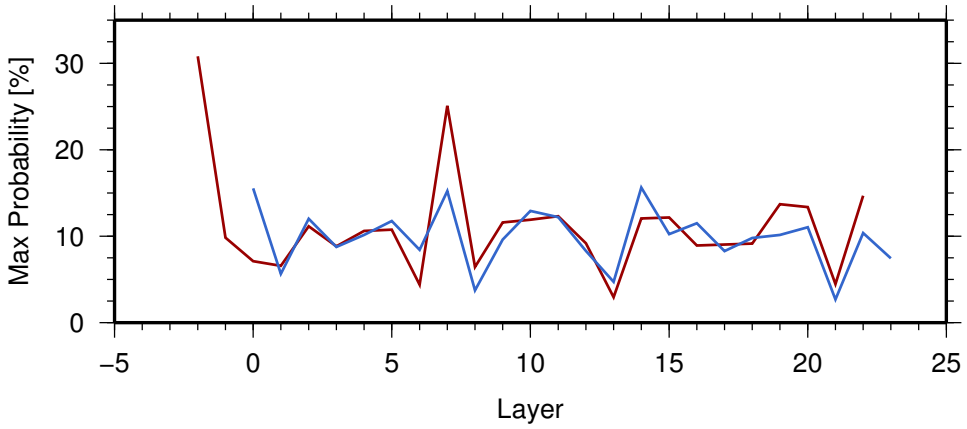

(b) The maximal probability of detecting a specific layer.

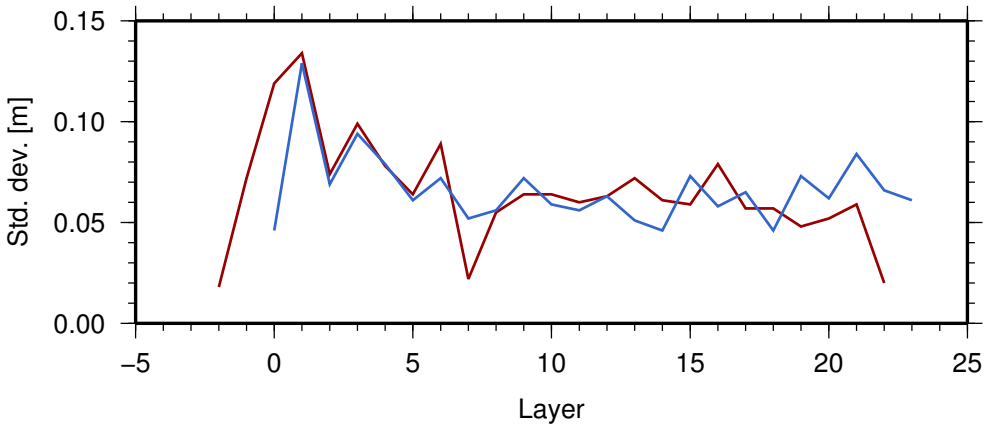

(c) Standard deviation of mean depth of a layer.

Figure 4.5: Accumulated probability of layer detection (a), maximal probability for layer detection (b) and standard deviation of the mean depth (c) for layers at T41 using 2006 (blue) and 2008 (red) data. 2008 data has been shifted two layers upwards to align layers from the same years. The maximal probability and standard deviation are determined from the fitted Gaussian.

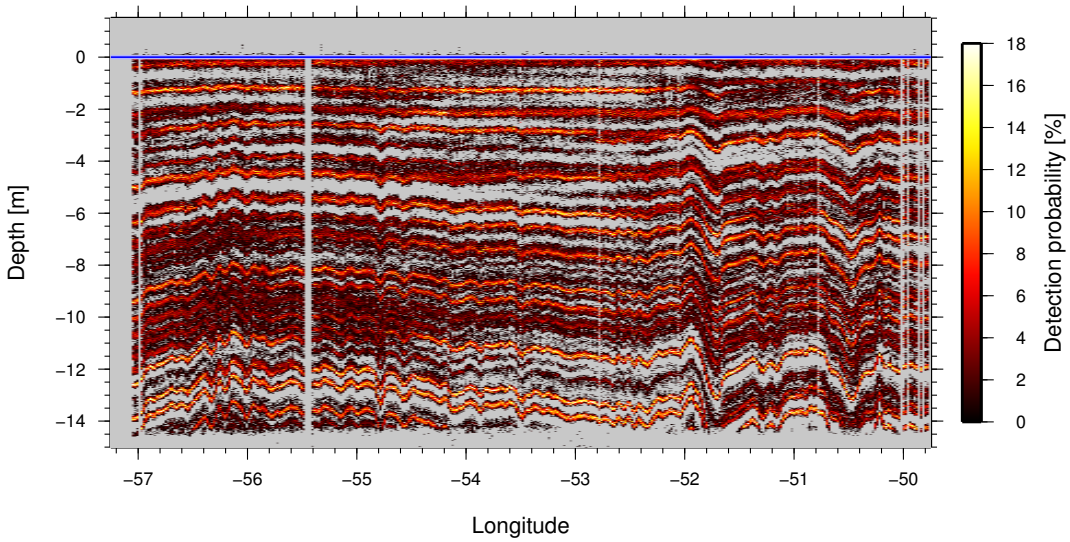

Figure 4.6: Layer detection probability along the north-west Greenland line as function of depth in color coding. Gray indicates zero peak detections or missing data and the blue line marks the surface.

The north-west Greenland profile was chosen because the snow properties in this area was expected to differ from the general snow properties in Greenland and to be more similar to the snow properties found in large part of Antarctica. When comparing the north-west Greenland profile in Figure 4.6 with the EGIG profiles in Figure 4.2 it is clear that the north-west profile is more noisy and the depth of detected layers is ambiguous in some parts of the profile. Unlike in the percolation zone refrozen melt water or heavily surface melt is not expected to be found in this area, and therefore the noisy layer detections are believed to be caused by the weak or lacking formation of autumn hoar in this area.

4.2.2 Estimation of Density Gradients from Repeated Observations

Using repeated ASIRAS observations of the layering in a chosen area allows for studies of firn densification. Figure 4.7 illustrates layers detected at a fixed position in two different years. The mass of a given layer i (e.g. layer 1 marked with gray in Figure 4.7a) per unit surface area in a epoch a can be calculated as:

$$m_i = T_i^a \cdot (\rho_0 + \delta\rho \cdot d_i^a) \tag{4.6}$$

Assuming that all mass is conserved within the given layer the densification can be observed as a thinning of the layer at a later epoch (see layer 1 marked with gray in Figure 4.7b).

Inserting the observed thickness and depth of a layer in Equation 4.6 for two epochs leads to two equations for the mass of layer i. Setting these two equations equal to each other and rearranging will lead to Equation 4.7. Using this equation it is possible to determine the density gradient ($\delta\rho$), if the surface density (ρ_0) is known. The assumption of mass conservation within a layer is only valid above the percolation zone and thus the method is

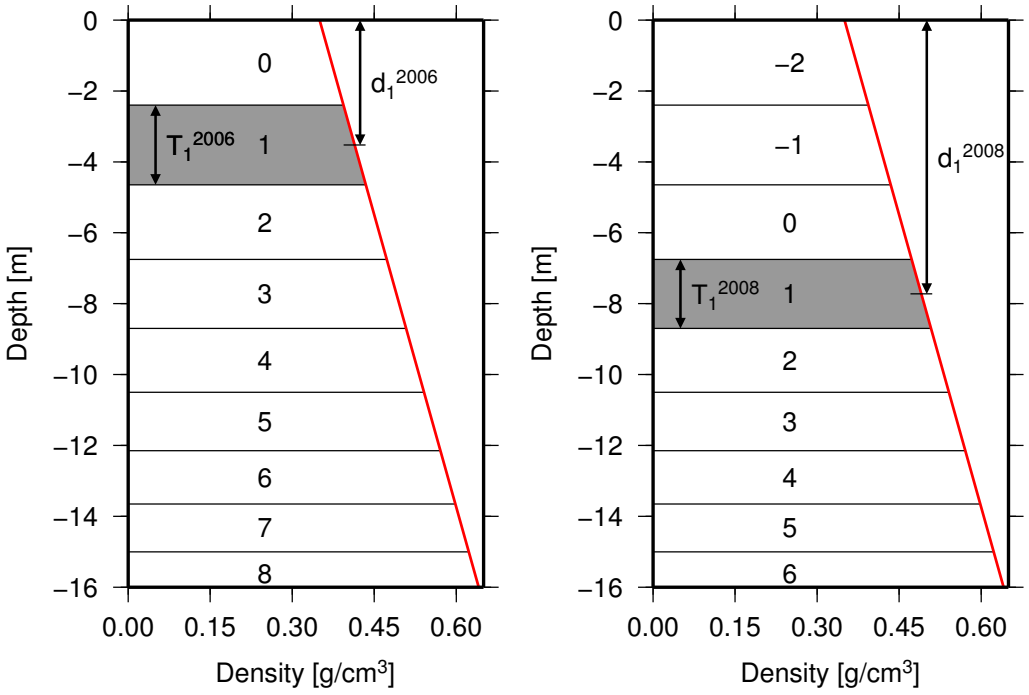

(a) Layers observed in 2006.

(b) Layers observed in 2008.

Figure 4.7: Layers observed in 2006 (a) and 2008 (b). The simple density profile is marked in red and the firn layers between two observed interfaces is marked with numbers indicating their horizontal place in 2006.

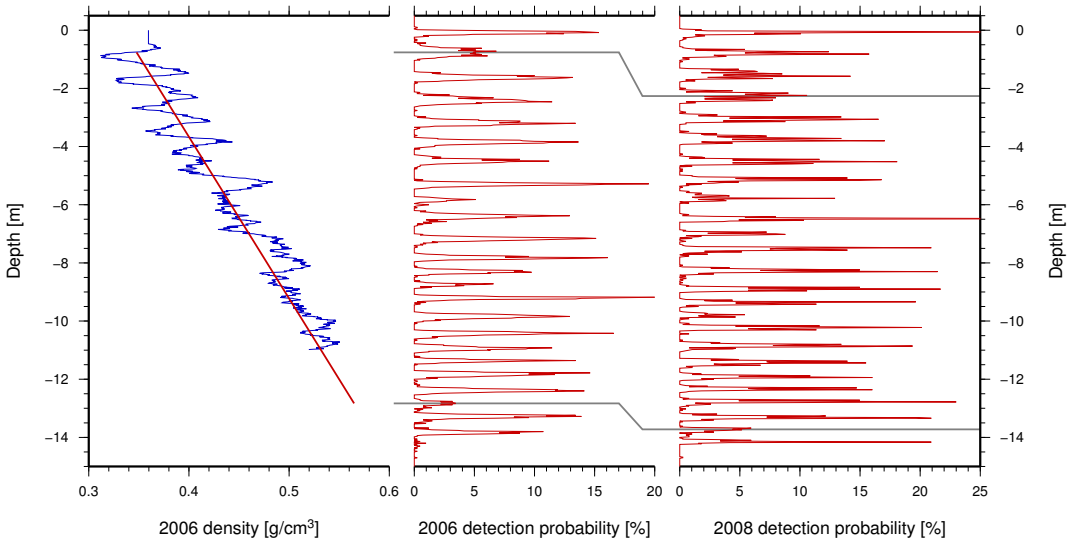

Figure 4.8: Comparison of in situ density profile, detected layers in ASIRAS data and estimated compaction. The left plot shows the measured density profile (blue) at T41 derived from N-probe data and the density profile derived from ASIRAS data (red). The middle and right plot shows the derived layer detection probabilities for 2006 and 2008 respectively (red). The two gray lines indicate the top and bottom layer used to derive the compaction. From Stenseng et al. (2011).

only reliable in the dry snow zone.

$$\delta\rho = \frac{\rho_0 \cdot (T_i^{2006} - T_i^{2008})}{d^{2008} - d^{2006} + (T_i^{2008} - T_i^{2006})/2} \tag{4.7}$$

In Stenseng et al. (2011) the method has been applied on the 2006 and 2008 datasets at T41 and here a good agreement between the density gradient estimated from ASIRAS data and in situ N-probe measurements of a density profile is found (See Figure 4.8).

4.3 Comparing Detected Layers with a Firn Compaction Model

In this section new results and further work in continuation of the Sørensen et al. (2010b) publication (included in Appendix A.3) will be presented. The work has been carried out in collaboration with Sebastian B. Simonsen, Centre for Ice and Climate, NBI, University of Copenhagen and Louise Sandberg Sørensen, DTU Space, National Space Institute.

In order to assess the effect of firn compaction on the volume to mass conversion, a firn compaction model has been developed (Sørensen et al., 2010a). The model uses temperature, runoff, snowfall and precipitation produced by dynamically downscaling the European Center for Medium-Range Weather Forecast (ECMWF) ERA-Interim reanalysis with the HIRHAM5 regional climate model (RCM). Using these variables, the depth and density of a series of layers can be modelled at a given epoch.

Figure 4.9 shows the layers detected in the 2006 EGIG profile together with the modelled layers. West of -39° the model is generally in good agreement with the layers detected in

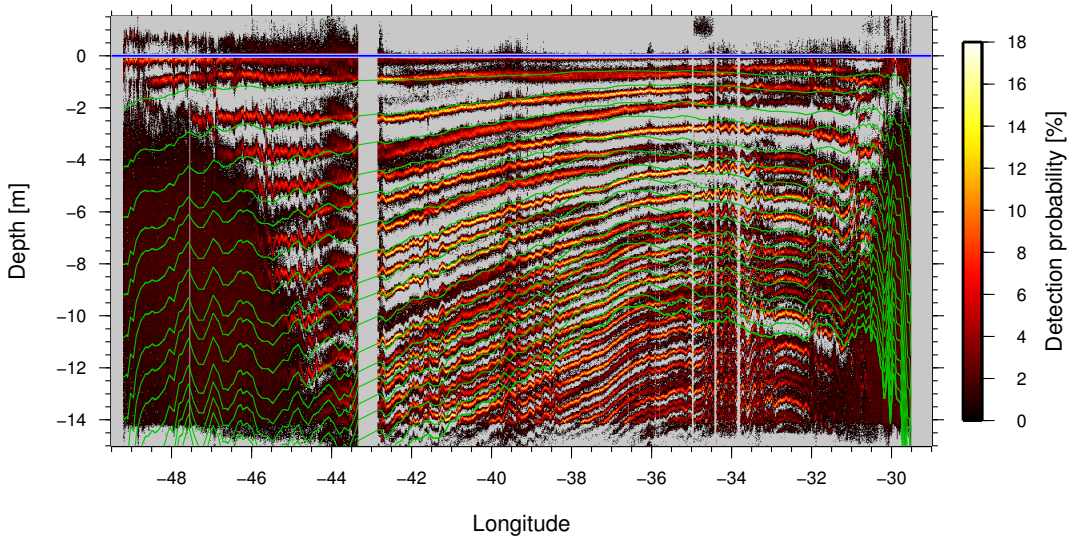

Figure 4.9: Layer detection probability along the EGIG line (2006) as function of depth in color coding. Gray indicates zero peak detections or missing data, the blue line marks the surface and the green lines indicates the modelled layers.

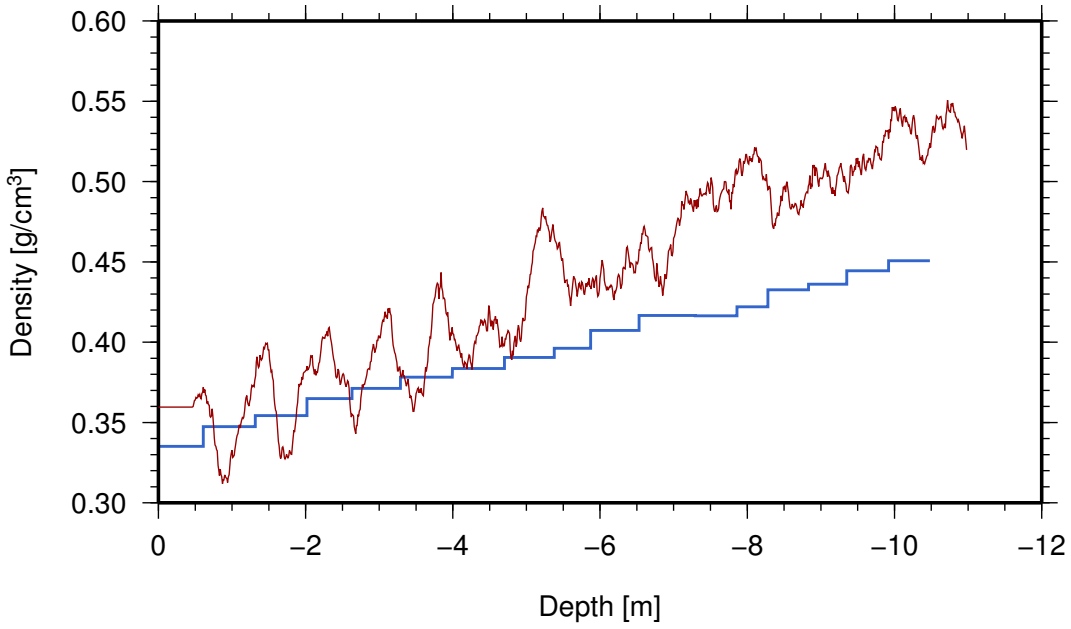

Figure 4.10: Comparison of density modelled (blue) and in situ N-probe measured (red) density profiles at T41 in 2006.

the radar data. In the central part of the ice sheet between -39° and -34.5° longitude, the model underestimates layer thickness and in the eastern part, the model switches to an overestimation of layer thickness. Unfortunately in situ measurement are only available from T41 and west (i.e. west of -37.9°). In Figure 4.10 it is seen that the model underestimates both the thickness and the density of the layers in this area.

By using the new methods for layer detection in ASIRAS data it it possible to derive the layer thickness and density gradients, and thereby provide a useful dataset for validation and improvement of the modelled densification. The knowledge gained from this investigation can be propagated back to the regional climate model and the re-analysed dataset and thus improve the understanding of the regional climate and how it is modelled.

4.4 Layer Detection in CryoSat-2 Data

This section will explore the possibilities of adapting the layer detection method from airborne ASIRAS data to space borne CryoSat-2 data. At the moment the default operation mode of CryoSat-2 over the dry snow zone in Greenland is LRM (see Figure 2.12) and SAR data is therefore not collected on a regular basis in this area.

Assuming first that the autumn hoar acts as a specular reflecting layer within the firn, the area contributing to the peak will be that of the first Fresnel zone. The radius of Fresnel zone number n can be calculated from the wavelength of the radar (λ) and the distance to the reflecting layer (h):

$$F(n) = \frac{1}{2} \cdot \sqrt{n \cdot h \cdot \lambda} \tag{4.8}$$

The radius of the first Fresnel zone is then calculated by inserting an average height above the surface of 720 km for CryoSat-2 and 300 m for ASIRAS and a wavelength of 2.2 cm for both.

For ASIRAS the typical along-track Doppler limited footprint is 2 m and the across-track beam limited footprint is 13 m. With a radius of 1.8 m for the first Fresnel zone the layer area contributing to the peak will be around 40% of the total illuminated area. For CryoSat-2 the typical along-track Doppler limited footprint is 250 m and the across-track pulse limited footprint is on the order of 1.6 km. The radius of the first Fresnel zone can be calculated to 89 m. It is, however, considered unlikely that the depth of the autumn hoar layer will be constant within the first Fresnel zone of the CryoSat-2 footprint.

Instead, the curvature of the pulse is considered. For a plan wave the power in one sample will be the average of the energy returned from the volume spanned the pulse length, the along-track size, and the across-track size. If the wave is spherical the volume is draped over a sphere and thereby it will span a depth interval larger than the pulse length. The curvature will therefore be comparable to a vertical smoothing of the layers.

The curvature, for ASIRAS, of the pulse front is less than 2 mm in the along-track direction and 5 cm in the across-track direction, both in firn. For CryoSat-2 the curvature of the pulse front is 5 cm in the along-track direction. In the top of the firn the across-track curvature of the pulse front will be 35 cm, equal to the compressed pulse length corrected for the lower propagation speed in firn. However, as the pulse propagates downwards in the firn the illuminated area will expand beyond the pulse limited footprint and thereby increase the curvature.

Using the new method on ASIRAS data it is possible to separate consecutive layers

which are more than 20 cm apart. The CryoSat-2 range resolution is 47 cm in air which is more than four times the ASIRAS range resolution. Assuming that the ability to separate layers can be transferred to CryoSat-2 data suggests that consecutive layer should be more than 80 cm apart to be detectable. The layer thickness in the dry snow zone is found to be between 20 cm and 1.5 m with an average around 75 cm. Furthermore, for CryoSat-2 the part of the autumn hoar layer contributing to a peak in the waveform is reduced by the changed geometry. It is therefore considered unlikely that CryoSat-2 can be used to map the autumn hoar layers in the dry snow zone on the Greenland Ice Sheet.

4.5 Summary

A new automatic method for the detection of annual layers in firn on the Greenland Ice Sheet has been developed by the author. The method detects peaks from layers in a number of individual echoes resulting in the probability of detecting a layer as function of depth. This new method offers a high resolution mapping of the annual layers associated with the autumn hoar. In the dry snow zone layers are detected within the full range of the radar i.e. it is only limited by the size of the radar's sampling window. When moving from the dry snow zone and into the percolation zone the number of detectable layers decreases as the deeper layer are masked by surface melt and refrozen melt water. The average standard deviation on the depth of a detected layer is 7 cm in the dry snow zone and 15 cm in the percolation zone. Using this new method it is furthermore possible to derive the average firn density gradient from two sets of ASIRAS data obtained at the same location a few years apart.

The derived layers and firn density gradient was compared with in situ N-probe measurements of the density profile. For the upper layers there is good agreement between the layers determined by N-probe and the layers found using the new method. In the deeper layers the difference between winter and summer firn density is less apparent in the N-probe data. This leads to an ambiguous identification of the layering and N-probe data is no longer useful for validation. In the dry snow zone the average density gradient derived from two ASIRAS dataset is in good agreement with the average density gradient derived from N-probe data. However it should be noted that the density variation within one year is large and therefore it is only possible to compare the density gradient average over several years.

West of the ice divide the agreement between layer derived from ASIRAS data and the layers derived from a firn compaction model driven by a regional climate model and re-analysed weather data. Near the ice divide the model underestimates the layer thickness compared to both the N-probe measurements and the ASIRAS derived layers. East of the ice divide the model generally overestimates the layer thickness. The new presented method can be used to gain a better understanding of the regional climate model and the re-analysed dataset and thereby be useful for future improvement of both the model and the re-analysed dataset.

Finally the possibilities of applying the new method to CryoSat-2 data is considered. Due to the higher range sample spacing it is unlikely that the new method will be able to separate autumn hoar layers closer than 80 cm when applied on CryoSat-2 data. Furthermore, the part of the autumn hoar layer contributing to a peak in the waveform is reduced due to the change in geometry when going from ASIRAS to CryoSat-2 data.

Chapter 5

Detection of Leads in Sea-Ice

One of the two main objectives for CryoSat-2 is to improve the estimates of the sea-ice mass and monitor its changes. Earlier studies have shown that the sea-ice thickness can be estimated from conventional pulse limited altimetry (Giles et al., 2008; Laxon et al., 2003). However, this is complicated by the fact that a small fraction of open water within the footprint can dominate the return, whereby the number of measurements available for freeboard estimation is lowered significantly (Peacock and Laxon, 2004). The high along-track resolution offered by SAR altimetry is believed to acquire more well behaved echoes. This will make more measurements available for freeboard estimation and allowing detailed studies of freeboards at smaller spatial scales.

In this chapter a new method, developed by the author, for automatic detection of leads in airborne SAR altimetry data over sea ice is presented. The 80% threshold retracker implemented in the software suite developed by the author has been applied to the airborne SAR data, and combined with the new lead detection method to derive the freeboard height. The automatic detection method is compared to a manual detection of leads using the same SAR dataset, and to laser scanning data also collected during the airborne campaigns. Furthermore, the joint laser and radar datasets are used for a study of the relationship between the properties of snow on the sea ice and the apparent penetration depth of the radar signals, compared to laser. The manual detection has been carried out by Stefan Hendricks from Alfred Wegener Institute for Polar and Marine Research. The comparison and analysis of the two detection methods, three different retrackers and the apparent penetration depth has been carried out by Stefan Hendricks and the author in collaboration with the co-authors of the Hendricks et al. (2011) paper.

The newly developed method has been tested on a single profile of real CryoSat-2 data. The method shows some shortcomings when applied to satellite borne SAR altimeter data resulting in an ambiguous detection. In an attempt to improve the detection the author has adapted the method to include some of the parameters unique to a SAR altimeter waveform. The adapted method is compared with an ASAR image in collaboration with Stine K. Poulsen, DTU Space, National Space Institute.

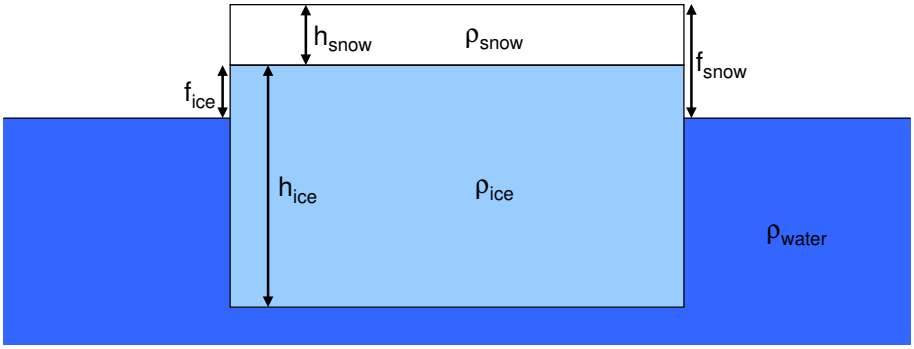

Figure 5.1: Ice floe covered with snow flowing in isostatic equilibrium with the ocean.

5.1 Estimating Sea-Ice Thickness from Freeboard

Direct measurement of the sea-ice thickness is not possible with the current satellite remote sensing techniques. Instead, the thickness can be derived indirectly by measuring the freeboard of the sea-ice floes and converting this observation into thickness by making a number of assumptions for the ocean, sea-ice, and snow. The conversion from freeboard to thickness is achieved with a multiplication, and the conversion is therefore highly sensibly to errors in the freeboard height. The most fundamental assumption needed for the thickness conversion is that the ice floe is in isostatic equilibrium with the surrounding ocean, as shown in Figure 5.1.

Using co-located airborne laser altimetry measurements of the freeboard (f_{snow}) and the draft from a submarine equipped with upward looking sonar, Comiso et al. (1991) established a relationship, depending on the water density and the mean snow/ice density, between the two measurements. Continuing this, Wadhams et al. (1992) obtains a slightly more complicated expression for the conversion factor. They are using a model containing typical values for the density of the ocean water (ρ_{water}), the sea-ice (ρ_{ice}), the snow cover (ρ_{snow}), and thickness of the snow cover (h_{snow}), and the sea-ice (h_{ice}). A number of typical conversion factors for different seasons and water densities were derived, ranging from 4.6 to 8.9.

With this relationship between freeboard and draft Giles et al. (2007) derived two expressions for the ice thickness (h_{ice}) directly from the assumption of isostatic equilibrium. The first (Equation 5.1) uses the freeboard measurement to the air/snow interface, which is the surface measured by a laser altimeter. The second (Equation 5.2) uses the freeboard measured to the snow/ice interface, which has previously been considered the surface observed by a radar altimeter (Beaven et al., 1995; Laxon et al., 2003).

$$\begin{aligned}(h_{ice} + h_{snow} - f_{snow}) \cdot \rho_{water} &= h_{ice} \cdot \rho_{ice} + h_{snow} \cdot \rho_{snow} \\ h_{ice} &= \frac{f(snow) \cdot \rho_{water} + h_{snow}(\rho_{snow} - \rho_{water})}{\rho_{water} - \rho_{ice}} \end{aligned} \tag{5.1}$$

$$h_{ice} = \frac{f_{ice} \cdot \rho_{water} + h_{snow} \cdot \rho_{snow}}{\rho_{water} - \rho_{ice}} \tag{5.2}$$

Typical values for thickness of the snow cover and the density of water, snow, and ice are needed, and are estimated from field measurement and climatology data (e.g. Wadhams et al. (1992) and Warren et al. (1999)).

5.2 Apparent Radar Penetration into the Snow Cover on Sea Ice

This section and section 5.3.1 will summarise and elaborate on the method and results, derived from ASIRAS data, presented in Hendricks et al. (2011) (included in Appendix A.4) and summarized in Hendricks et al. (2010) and Nicolaus et al. (2010).

In a controlled laboratory experiment, Beaven et al. (1995) investigated the radar backscatter of bare and snow covered ice, and concluded that the scattering surface was the air/ice or the snow/ice interface. Field experiments carried out with a ground based K_u-band radar showed a more complex picture, with only 30% of the returns originating from the snow/ice interface, 43% from the air/snow interface, 23% from layers within the snow layer, and the rest from unidentified sources (Willatt et al., 2010). This finding was confirmed by airborne ASIRAS data at a number of sites (Willatt et al., 2011).

The penetration of K_u-band radar into the snow on sea-ice was investigated in five areas using several thousand kilometres of coincident airborne laser and ASIRAS radar data collected in the Baltic Sea (2005), Greenland Sea (2006 and 2008), and Lincoln Sea (2006 and 2008). Leads are detected manually using both laser and radar data, and used as a reference for the instantaneous sea surface height. The leads are furthermore used to calibrate the height offset between the laser and the radar. This ensures a consistent and unambiguous determination of the instantaneous sea surface height for both sensors.

The detected leads are used to generate a model for the instantaneous sea surface height for all profiles, by spline interpolation. The model of the instantaneous sea surface are then subtracted from the laser and radar profiles to obtain laser and radar freeboard profiles. Figure 5.2, shows the freeboard probability distribution histograms for laser and radar in the five areas, where the first mode at zero meter freeboard shows the amount of leads found in the datasets. Comparison of the second mode of the laser and radar histograms indicates that some penetration of the radar occurs in the Greenland Sea in both 2006 and 2008. The higher laser freeboard above the second mode in the Lincoln Sea in 2006 suggests some penetration.

A further investigation of these findings are performed by a point to point comparison of laser and radar freeboard measurements. Figure 5.3 presents 2-D histograms of the height difference between the laser and the radar versus the laser freeboard for the five areas. The histogram from the Greenland Sea in 2006 confirms a penetration for the majority of measurements of less than 10 cm over ice with 50 cm laser freeboard. However, this is only about one third of the expected snow thickness in this area (Warren et al., 1999). For the Lincoln Sea in 2006 and the Greenland Sea in 2008 the difference between the laser and the radar freeboard is slightly positive, indicating a moderate radar penetration.

Based on the work presented in Hendricks et al. (2011) it must be concluded, that the reflecting surface observed by the K_u-band radar in late spring is not the snow/ice interface but closer to the air/snow interface.

5.3 Detection of Leads

To derive the freeboard from the altimetry data over sea-ice knowledge about the instantaneous sea surface height at the position of the measurement is needed. Models of the mean sea surface or the geoid will only give a rough estimate of the instantaneous sea surface

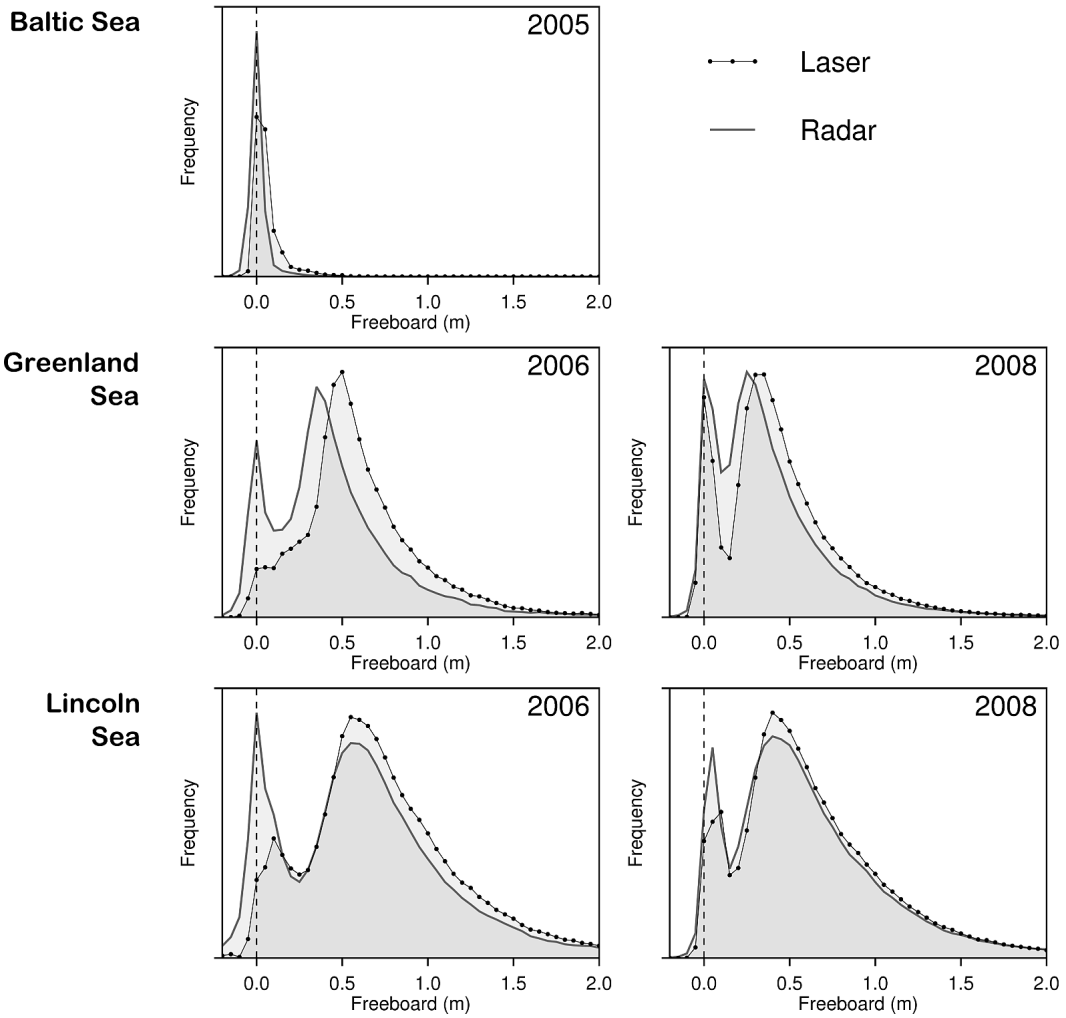

Figure 5.2: Probability distribution of differences between laser and radar freeboard (laser minus radar). The frequency at zero meters freeboard difference indicate the amount of leads in the dataset. From Hendricks et al. (2011).

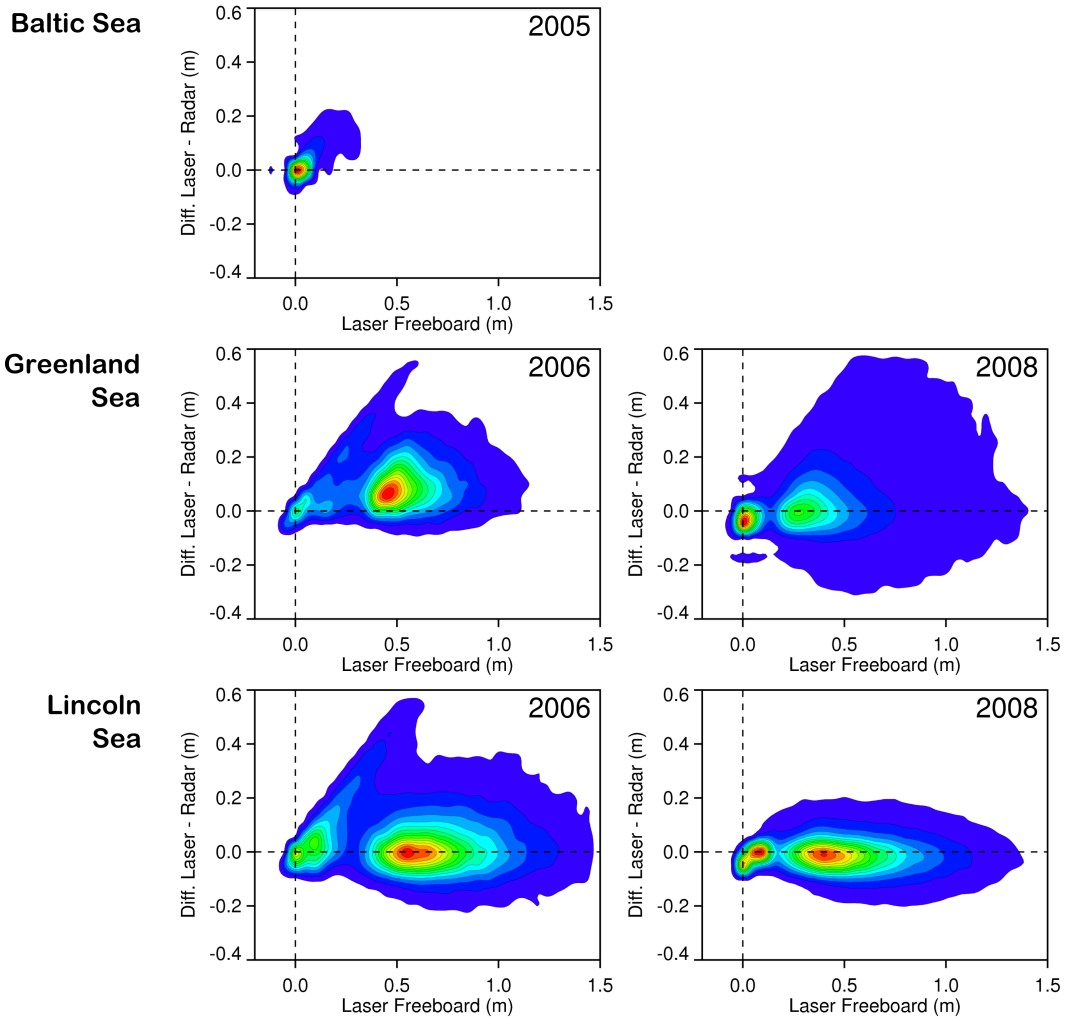

Figure 5.3: Scatter plot of difference between point to point heights measurements derived from laser and radar data against laser freeboard. From Hendricks et al. (2011).

height. Instead the instantaneous sea surface height needs to be derived directly from the altimetry data.

Waveforms returned from an ice covered ocean shows a high variability in shape, depending on the sea-ice type, and the fraction of water within the footprint. Some of these waveforms are highly specular and can be associated with leads or newly frozen leads and are thereby useful for deriving the instantaneous sea surface height. A specular reflection can occur if more than 1% of the footprint satisfies the Rayleigh criterion, which for K_u-band is equivalent to a surface roughness of less than 3 mm. The peak power can be as much as three orders of magnitude higher than that of an average ocean echo (Drinkwater, 1991; Fetterer et al., 1992).

Peacock and Laxon (2004) used the pulse peakiness parameter to identify leads in the Arctic Ocean and was thereby able to derive a mean sea surface from European Remote Sensing satellite (ERS) data. The pulse peakiness parameter is the scaled fraction of the most powerful sample over the summed power in the waveform.

$$PP = \frac{31.5 \cdot p_{max}}{\sum_{i=5}^{64} p_i} \tag{5.3}$$

The SAR echoes are peaky by nature, and therefore this empirical approach will most likely become sensitive to small changes in the echo.

Another approach, applicable to laser altimetry, is presented by Forsberg and Skourup (2005). Here the approach is more of a statistical nature, and fits an instantaneous sea surface to the lowest height observations in the profile. This method is highly sensitive to strong off nadir reflectors which will have an apparent lower height and will therefore wrongly be interpreted as sea surface.

5.3.1 Detection of Leads in ASIRAS Data

A new method for lead detection in airborne ASIRAS data was developed by the author. The method uses a combination of waveform parameters, and a lowest level filter to mark waveforms believed to originate from leads.

First, the distribution of power and waveform width, determined from the OCOG retracker, is analysed for the selected profile. Threshold values for the width and power, indicating an echo from a lead, are selected based on the distributions. The echoes, which exceeds the power threshold and are below the width threshold, are marked as lead candidates. Second, the determined height of all lead candidates are compared to the height of nearby echoes and rejected if it is not the lowest measurement.

The developed method has been tested on a 380 km long profile obtained north of Greenland on April 27 2008 and compared with a manual picking of leads using a laser derived digital elevation model (DEM) (Figure 5.4a). This profile has been chosen as it contains areas of open water suitable for accurate determination of the bias between the different methods. Furthermore the profile contains both first year ice and some multi year ice.

A histogram of the difference between the automatic and the manual picking of leads is shown in Figure 5.4b. From the histogram it can be seen that for 95% of the detections the discrepancy are below 7 cm, and for 50% of the detections the discrepancy are below 2 cm, which is better than the accuracy of the DEM.

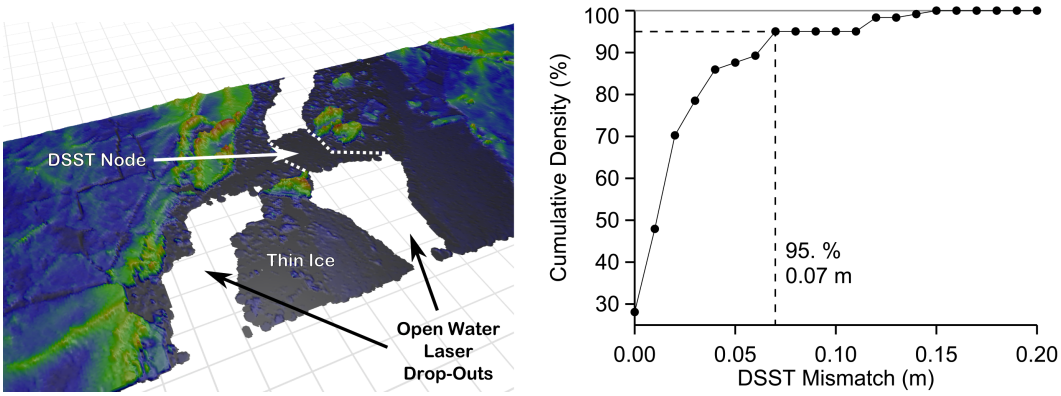

(a) Part of the laser DEM over an open water lead. Off nadir the lead acts as a mirror and reflects the laser pulse away from the laser scanner leaving a gap in the DEM.

(b) Cumulative distribution of the height difference between the manual and the automatic lead detection methods.

Figure 5.4: Example of laser DEM over an open water lead (a) and the cumulative height difference between the automatic and the manual lead detection methods. From Hendricks et al. (2011).

The difference between the manual and automatic method is most likely primarily linked to the range resolution of the radar. Some of the leads found in the airborne SAR data will behave like a delta function with all power concentrated in one single sample. In these cases it is not possible to perform a prober retracking of the radar data and the height determination will not be accurate. The combination of radar and laser data on the other hand does not suffer from the same problem as both the range resolution and spatial resolution of the laser is higher.

5.3.2 Detection of Leads in CryoSat-2 SAR Data

The lead detection method developed for ASIRAS data has been tested on CryoSat-2 data. The maximal return power in a waveform is a good indicator of a possible lead, and for the tested profile the power alone appears to be sufficient to detect leads, but this needs to be confirmed with a much larger dataset. The distribution of the width parameter on the other hand was too narrow to allow a stable detection for the tested profile.

Instead parameters unique to SAR altimetry data was investigated. When CryoSat-2 passes over a target it samples the reflected power as a function of incident angle. Figure 5.5 shows simulations of the power summed in the range direction during a pass over a diffuse reflecting surface (Figure 5.5a) and a specular target (Figure 5.5b). Over the diffuse target the shape of the power as a function of incident angle reassembles that of the two-way antenna pattern, which is in agreement with the findings of Stenseng (2009), using ASIRAS data over ocean. Figure 5.5b shows how the power rapidly drops when moving away from the normal incident angle over the specular target.

In the CryoSat-2 level 1b product the shape of the stack is expressed using the first four moments of the power distribution. When CryoSat-2 approaches a specular target the shape of the stack will change from a diffuse to a specular shape, which is equivalent to an

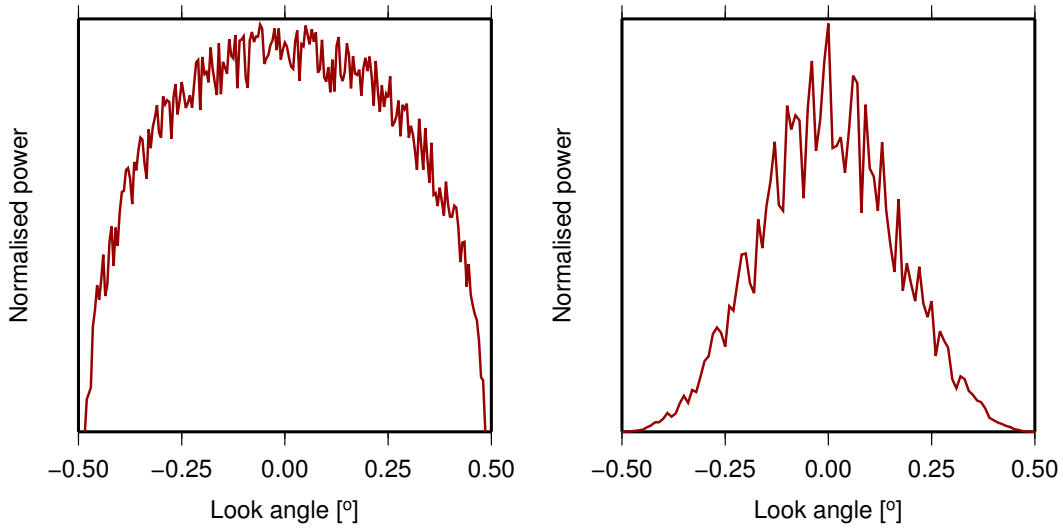

(a) Beams from a uniform rough surface.

(b) Beams from a surface with a specular reflector near nadir.

Figure 5.5: Power in the stack as a function of look angle over a diffuse and a specular target. Adapted from Wingham et al. (2006)

increase in the kurtosis of the distribution. The mean of the stack will move forward due to the powerful return from the specular target ahead, and this will also increase the skewness of the distribution.

Based on these considerations a new scheme for lead detection is made to pick echoes with power, skewness, and kurtosis above a set of thresholds. The new scheme is tested on a CryoSat-2 SAR altimeter profile obtained on October 8 2010 in the Wandel Sea north of Greenland. In the first commissioning phase release of CryoSat-2 SAR data the tail of the waveform is truncated, as shown in Figure 2.15. The combination of peaky SAR waveforms and a varying number of truncated samples, as shown in Figure 2.15, makes the pulse peakiness method unsuitable for comparison. Instead the profile is tested against an Envisat ASAR (ESA, 2011) scene obtained over the same area within 15 minutes of the CryoSat-2 overpass.

Comparison of CryoSat-2 Data with Envisat ASAR

The comparison with ASAR data has been carried out in collaboration with Stine K. Poulsen, DTU Space, National Space Institute and presented in Poulsen et al. (2011).

In Figure 5.6b the retracked height, the returned power and three stack parameters are plotted for a section of the CryoSat-2 profile, and Figure 5.6a shows a zoom on the ASAR scene with the same CryoSat-2 track plotted in light grey. Using the scheme presented above leads are detected and marked with a shaded background in the lower plot and red dots in the upper plot. When inspecting the ASAR scene it is seen that all major and some minor leads are detected, which is promising for the detection scheme. It is noted that a number of candidates between echo 1450 and 1550 were not picked and this suggests that the scheme could be improved.

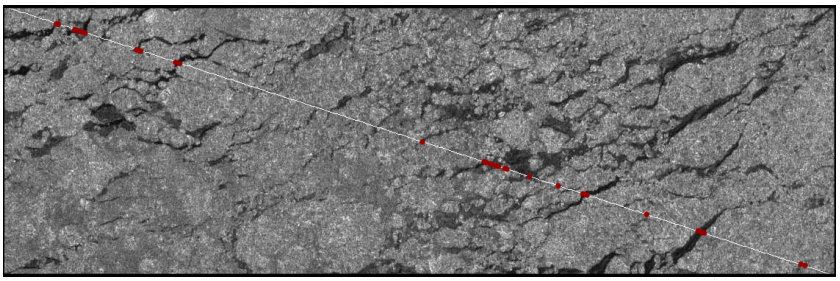

(a) Envisat ASAR image overlayed with CryoSat-2 track. Red dots indicates detected leads.

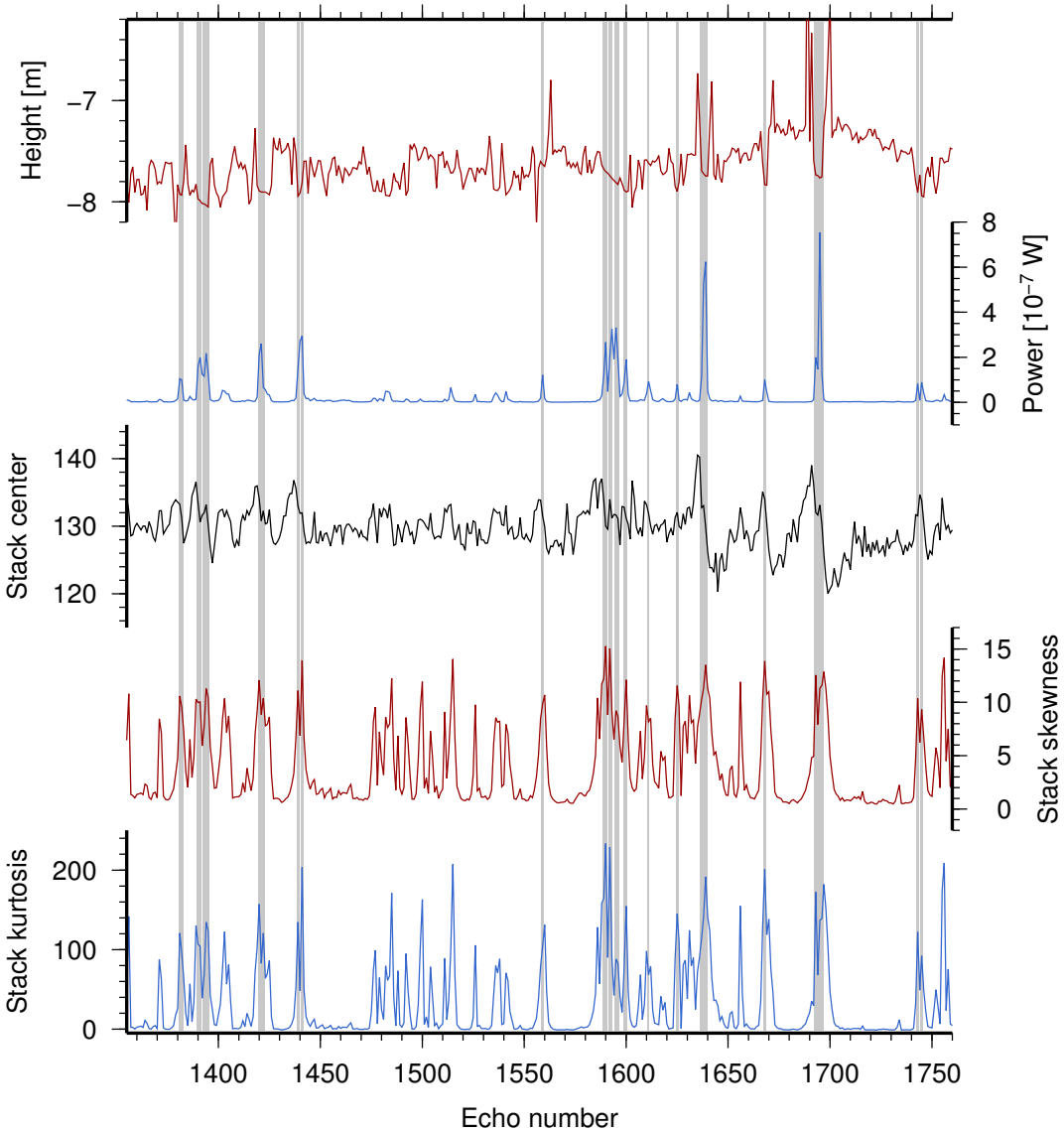

(b) Height (top red), return power (top blue), and stack parameters; center (black), skewness (red), and kurtosis (blue). Shaded areas indicate detected leads.

Figure 5.6: Envisat ASAR image compared with 80% threshold retracked height, return power, and stack parameters from CryoSat-2 SAR data.

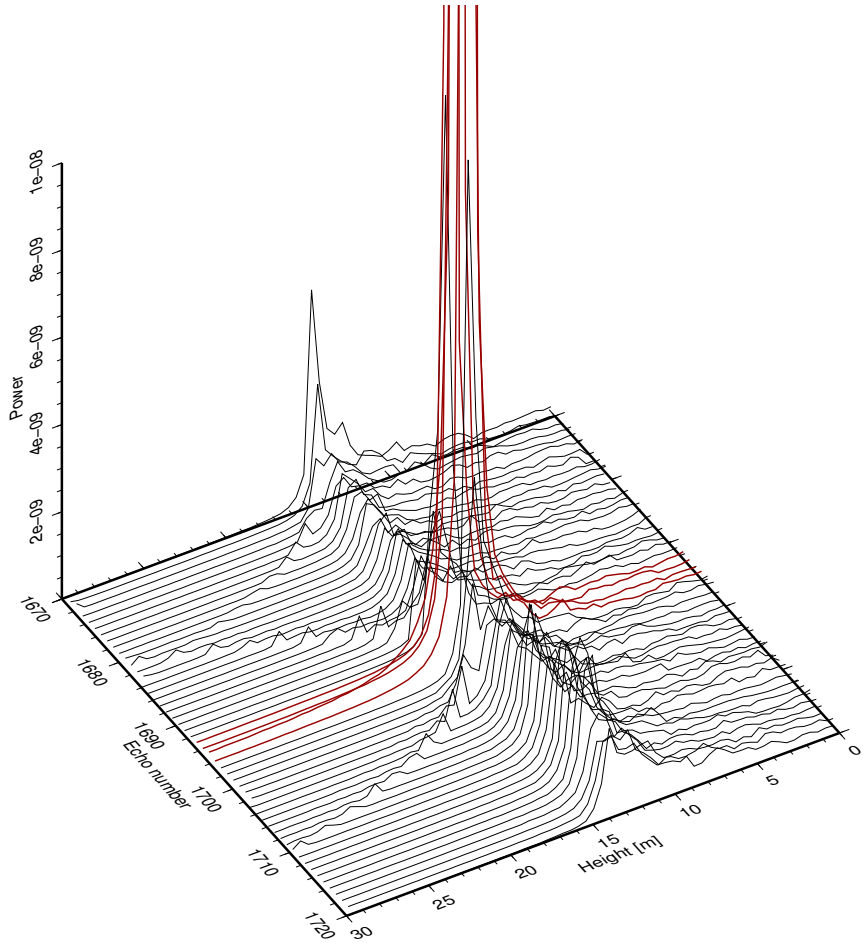

Figure 5.7: CryoSat-2 SAR waveforms near and above the lead at echo 1695 (flagged waveforms are red). The peak power in the four echoes over the lead exceeds $7 \cdot 10^{-7}$ W and were clipped to enhance the details in the other echoes.

In Figure 5.6b the signal from the two big leads near echoes 1640 and 1695 exhibit the expected behaviour, with increasing skewness and kurtosis near the center of the lead and a stack center shifted forwards before, and backwards after, passing the center of the lead. The retracked height on the other hand have some high sharp peaks just before, and after, the two big leads which was not expected, therefore the lead at echo 1695 is investigated further.

Figure 5.7 show the four echoes flagged as originating from leads in red together with the nearby echoes in black. The powerful return in echo 1695 reaches a peak power of $7.5 \cdot 10^{-7}$ W, more than two orders of magnitude larger than the average surrounding echoes. The reason for the unexpected high retracked heights are also visible as a hyperbola of power leaking from the very powerful echo 1695. Close to the lead the leaking power will blend with the surface return and erroneously be retracked as the surface height. This hyperbola is caused by the side lobes of the synthetic aperture and is expected to be reduced in future releases of CryoSat-2 data.

5.4 Summary

The author has developed a new automatic method for detection of leads in airborne SAR altimetry data collected over sea ice. In the method lead candidates are found based on the maximal returned power and the width of the returned waveform. The surface height of the candidates are then compared with the height of the nearby surface and accepted if the lead candidate is the lowest. The automatic method designed for airborne SAR altimetry data is compared with a manual detection of leads based on the same SAR dataset and coincident laser scanning altimetry along a 380 km profile north of Greenland. For 95% of the detected leads the discrepancy between the two methods is below 7 cm, and for 50% of the detections below 2 cm. This discrepancy is primarily an effect of adding the laser altimetry data in the manual method which improves the height determination. However, for 50% of the detections the discrepancy is less than the estimated accuracy of the DEM.

The combined radar and laser dataset has been used to study apparent penetration of the radar signal to investigate the snow layer on top of the sea ice. The largest apparent penetration is found in the Greenland Sea profile from 2006, but the penetration is less than one third of the expected snow thickness. For the 2008 and the Lincoln Sea datasets the apparent penetration is even less. This indicates that the reflecting surface observed by the K_u-band radar in late spring is not the snow/ice interface but closer to the air/snow interface.

The developed automatic lead detection method has been adapted and extended to CryoSat-2 data by the author. In the adapted method the parameters which describes the power distribution of the individual looks forming the final waveform are included in the detection scheme. The author has applied the adapted method on a single profile of real CryoSat-2 data, which has been compared with an ASAR image obtained within 15 minutes of the CryoSat-2 overpass. In the comparison no false detections were identified, which is very promising for this method. Finally the author has identified a problem in the first release of commissioning phase data resulting in power leaking from echoes over leads and into nearby echoes making the retracking of the nearby echoes ambiguous.

Chapter 6

SAR Altimetry for Sea Level and Gravity Field Mapping

When the first radar altimeter satellites were launched in the 1970's oceanographers for the first time got a global snapshot of the sea surface, an impossible task for the previous years ship based oceanography missions. Since followed a range of spaceborne radar altimeters with various orbit configurations and instrumentations each targeting prime goals such as the geoid determination, ocean currents, or the tides. Radar altimeters are constantly being improved and each new generation of altimeters offers a higher precision, better signal to noise ratio, and better orbit determination.

However, the physical nature of the conventional altimeter has its limitation and new concepts are needed in order to continue the rate of improvements and to achieve better ocean altimetry in the future. The introduction of the SAR altimeter principle offers a possible way to improve radar altimeters now and in the future. The SAR altimeter features a much smaller footprint which is independent of significant wave height. Furthermore, it increases precision in the determination of sea surface elevation, significant wave height, and wind speed (Jensen and Raney, 1998). CryoSat-2 will lead the way for SAR altimetry and will in the near future be followed by the Sentinel-3 mission.

In this study the retracker software suite, developed by the author, has been used on real data from CryoSat-2 to investigate the performance of the SAR altimeter for sea level mapping. To get an independent evaluation of the sea level measurement, gravity fields are derived from the measurements and compared to marine gravity field measurements. The gravity field determination and comparison with marine gravity field measurements have been carried out in collaboration with Ole Baltazar Andersen, DTU Space, National Space Institute.

6.1 Marine Gravity Field Derived from Altimetry

To the first approximation the sea surface will follow the geoid, thus the geoid can be derived over the ocean from satellite altimetry. From the geoid height (N) and the normal gravity (γ_0) the disturbing potential (T) can be calculated using Bruns formula, and by applying the fundamental equation of physical geodesy the gravity anomaly (Δg) can be

related to the disturbing potential (T) (Heiskanen and Moritz, 1999; Torge, 1991).

$$\Delta g = -\frac{\partial T}{\partial r} - \frac{2 \cdot T}{r} \qquad , \qquad T = \gamma_0 \cdot N \tag{6.1}$$

However, the instantaneous sea surface height ($\xi(t)$) is a combination of the geoid and a range of phenomenons such as e.g. ocean currents, wind, barometric pressure, and ocean temperature. Therefore the instantaneous sea surface height measurement ($h_{ssh}(t)$) should be considered the sum of the geoid height (N), the instantaneous dynamic sea surface height, and the error (e) (Andersen and Knudsen, 2009; Andersen et al., 2010).

The instantaneous dynamic sea surface can further be decomposed into the mean dynamic topography (ξ_{MDT}), which is mainly a result of the ocean currents, and the rapid varying dynamic sea surface topography (ξ_D), caused mainly by meteorological interaction with the ocean. Likewise the geoid height can be split into a known reference model (N_{EGM}), e.g. the earth gravity field model 2008 (EGM08) (Pavlis et al., 2008), and a residual (ΔN).

$$\begin{aligned} h_{ssh}(t) &= N + \xi(t) + e \\ &= N_{EGM} + \Delta N + \xi_{MDT} + \xi_D(t) + e \end{aligned} \tag{6.2}$$

The dynamic sea surface topography is assumed to average out when using a long period of altimetry from exact repeat missions (e.g. Envisat, ERS-2, and Jason-1). For non-exact repeat missions or missions with a long repeat period the dynamic sea surface topography will be too sparsely sampled to average to zero. Instead segments of altimetry tracks shorter than the typical wavelength of the disturbances can be fitted to a reference surface by removal of a bias and a tilt from the individual tracks and this way minimize the dynamic sea surface topography. The fitting procedure will not only minimize the dynamic sea surface topography but also orbit errors.

The ocean currents and general ocean temperature pattern (i.e. warm equatorial and cold polar waters), causing the main part of the mean dynamic topography, is constant over long time scales and will therefore not average to zero but remain as a signal. Thus the mean dynamic topography can only be derived from the mean sea surface if the geoid is known, and the geoid can only be derived from the mean sea surface if the mean dynamic topography is known.

In the following it is assumed that the mean dynamic topography is known (e.g. from a oceanographic model) and thus the residual geoid height can be determined from the instantaneous sea surface height.

Sandwell and Smith (1997) propose that the north-south and east-west deflection is determined at the track crossover point and use this information to derive the gravity field. The CryoSat-2 orbit is almost polar and the tracks are therefore close to parallel most places and the east-east deflection is poorly determined.

Instead the method proposed in Andersen et al. (2010) is considered. First the mean dynamic topography and the Earth Gravitational Model (EGM) 2008 is removed and each track is corrected for bias and tilt to minimize the effect of the dynamic sea surface topgraphy and orbit errors. Next the tracks are crossover adjusted using bias and tilt on each track before outliers are removed. The tracks are then gridded onto a regular grid and the residual gravity signal is computed using FFT techniques, and finally the EGM2008 is restored to obtain the gravity field.

	LRM (area S)				SAR (area N)		
	OCOG	Threshold	Beta	L2	OCOG	Threshold	Beta
Points (Before edditing)	28444	28444	28139	18182	72925	72925	68824
Points (removed gross error)	28060	28127	27941	18180	68664	71653	68176
Std. dev.	1.008 m	0.998 m	1.027 m	0.760 m	1.231 m	1.237 m	1.279 m
Std. dev. (removed tilt and bias)	0.250 m	0.085 m	0.110 m	0.076 m	0.349 m	0.254 m	0.363 m
Points (resampled 5 Hz)	6921	6958	6921	4421	16974	17786	16585
Mean (obs-ref)	0.003 m	0.000 m	0.003 m	0.000 m	0.000 m	0.000 m	0.000 m
Std. dev. (obs-ref)	0.130 m	0.051 m	0.066 m	0.044 m	0.232 m	0.171 m	0.187 m
ERS-1 GM std. dev.	0.09 m				0.141 m		

Table 6.1: Effect of the data editing and choice of the retrackers in comparison with ERS-1 geodetic mission. From Stenseng and Andersen (2011).

6.1.1 Sea Level and Gravity Field Mapping in the Baffin Bay Using SAR Altimetry Data

This section will elaborate and expand on the method and results presented in Stenseng and Andersen (2011) (included in Appendix A.2). The gravity field determination and comparison with marine gravity field measurements presented in this section has been carried out in collaboration with Ole Baltazar Andersen, DTU Space, National Space Institute.

Three months of CryoSat-2 data from the Baffin Bay has been investigated to derive a sea surface over the area. The sea surface has been used to derive a gravity field using the method by Andersen et al. (2010) described above. The derived gravity field is compared to marine ship gravity data to evaluate the improvement that can be expected from a marine gravity field based on CryoSat-2 data (Andersen, 2008).

The Residual Sea Surface Derived from CryoSat-2 Data

The SAR tracks in the Baffin Bay from September to November 2010 is retracked using the developed software suite presented in Chapter 3. First, outliers were removed from the track by rejecting points more than three times the standard deviation from local mean difference to the DTU10 mean sea surface. Next, the mean dynamic topography and the EGM2008 geoid are removed from the derived heights before bias and tilt is removed from each individual track. To ensure consistency in the tracks a crossover adjustment of the tracks is carried out using bias and tilt terms. The CryoSat-2 tracks are finally resampled using an overlapping six measurements window rejecting the two samples that depart the most from the average. The remaining signal will be the residual sea surface used in the further computation of the gravity field. The performance of the different retrackers and the effect of the steps in the pre-processing is given in Table 6.1.

It should be noted here that the ERS-1 data is resampled from 20 Hz to 1 Hz (6.7 km along-track) and the CryoSat-2 data from 20 Hz to 5 Hz (1.1 km along-track). ERS-1 is a conventional altimeter and the footprint size is in the order of 2 - 10 km depending on the significant wave height and therefore no additional information is gained by resampling to 5 Hz. The used CryoSat-2 SAR data has a Doppler limited footprint in the along-track direction equal to approximately 250 m independent of the significant wave height. A study performed on simulated SAR data suggest that 5 Hz is the optimal sampling for gravity field determination from CryoSat-2 data (Andersen, 2008).

Figure 6.1 show the residual sea surface obtained from the CryoSat-2 data plotted on

top of a similar dataset obtained from the ERS-1 Geodetic Mission. When comparing the CryoSat-2 data with the ERS-1 a good overall agreement is found, but it is also noticed that short profiles looses its information when the bias and tilt terms are removed.

The track, obtained on October 11 2010 and marked with blue arrows in Figure 6.1, passing through both the maximal and minimal extremes is used for a more detailed comparison. Figure 6.2 shows the selected CryoSat-2 track travelling from south to north in red on top of ERS-1 data in grey. ERS-1 and CryoSat-2 have different orbit configurations and it is therefore not possible to compare tracks from the two satellites directly. Instead ERS-1 data within ± 5 km across-track is projected onto the CryoSat-2 track and plotted as a function of the along-track distance.

A good agreement is also found between the ERS-1 and the CryoSat-2 dataset, see Figure 6.2. Apparently the ERS-1 data is much more noisy than the CryoSat-2 track however one should be careful when comparing the one CryoSat-2 track with the combination of ERS-1 tracks used in the figure. Small peaks are found in the profile between 250 and 350 km along-track and is believed to be caused by the resampling. This resampling is not optimized toward the increased resolution of CryoSat-2 and the steep slope is therefore not represented well. Upon inspection a linear increasing offset between the two datasets is found when moving toward the northern part of the track. This trend is believed to be an artefact of the few crossovers giving a looser constraint on the three months of CryoSat-2 data compared to the one year of ERS-1 data.

A closer inspection of Figure 6.1 reveals some noisy tracks in the western part of the area. The noise is believed to be caused by the sea-ice building up in the Baffin Bay and flowing down from the Nares Strait. Sea-ice concentration derived from passive microwave data obtained with the Special Sensor Microwave Imager/Sounder (SSMIS) instrument has been used to investigate the extent of sea-ice in the test area in the three month period (Nolin et al., 1998).

Figure 6.3 shows the evolution of the sea-ice concentration during the period of interest. During the first two month (Figures 6.3a and 6.3b) the test area is almost free of sea-ice. In the beginning of November (Figure 6.3c) the sea-ice concentration begins to increase in the western part of the area, and during the next 10 days the sea-ice rapidly spreads covering more than half of the area (Figure 6.3d). This small investigation of the sea-ice concentration clearly stresses the importance of using other datasets to mask unwanted signals which could influence the quality of the derived gravity field.

Deriving and Evaluating the Gravity Field

The three months of CryoSat-2 data is insufficient to derive a gravity field, therefore the ERS-1 data is used as a base and the improvement gained by adding the CryoSat-2 data is evaluated. To obtain the gravity field the tracks representing the residual sea surface are gridded and converted to a gravity field using FFT techniques as described in Andersen et al. (2010).

First, a gravity field is calculated using only ERS-1 data. This will be the benchmark to evaluate the added CryoSat-2 data against. Next, two gravity fields are derived from the combination of ERS-1 and CryoSat-2 data. In the first combined gravity field the added CryoSat-2 is treated as the ERS-1 data with no changes to the processing. For the second combined gravity field the error on the CryoSat-2 data has been reduced and the reduced footprint size has been accounted for.

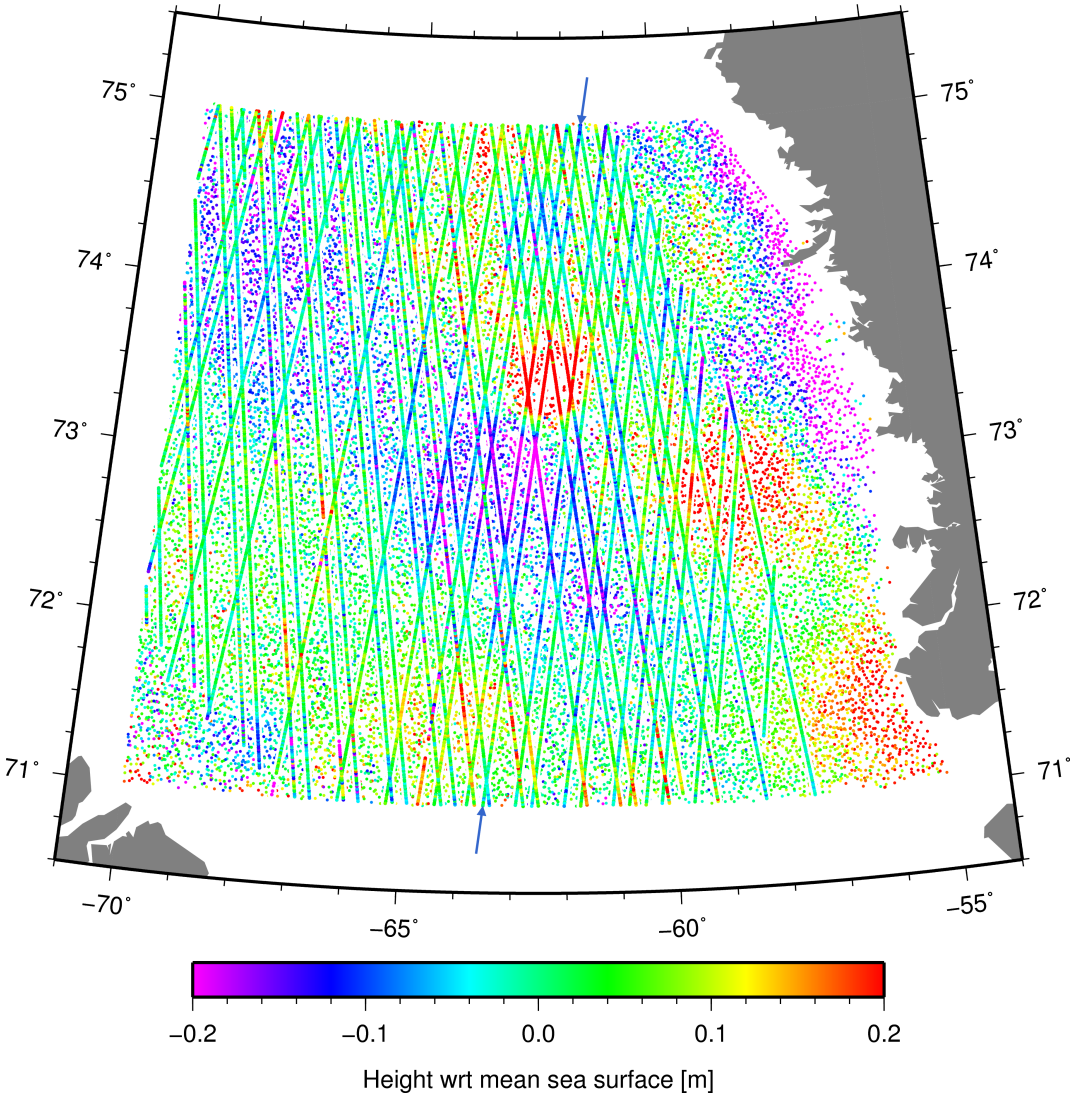

Figure 6.1: Height with respect to the mean sea surface of ERS-1 data from the geodetic mission and overlayed with CryoSat-2 data. A track passing through the large positive and negative anomalies is marked with blue arrows.

Altimetry data	Std. dev.
ERS-1 GM	6.130 mGal
ERS-1 GM + CryoSat-2 standard	6.106 mGal
ERS-1 GM + CryoSat-2 tuned	5.449 mGal

Table 6.2: Standard deviation of the difference between marine gravity and gravity estimated from altimetry.

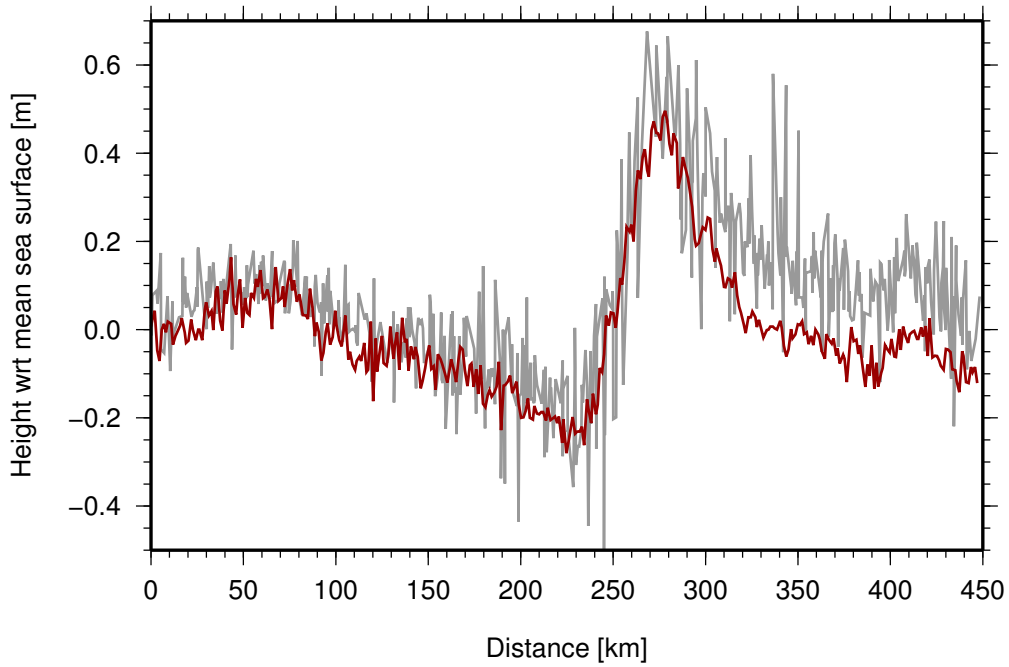

Figure 6.2: Height of the selected CryoSat-2 SAR track (red) and ERS-1 measurements within 5 km from the SAR track (grey), with respect to the mean sea surface.

The three gravity fields derived from ERS-1 and CryoSat-2 altimetry are evaluated against a set of more than 5000 marine gravity field observations extracted from the Nordic gravity field database (see Figure 6.4). The standard deviation of the difference between the three altimetry derived gravity fields and the marine gravity field observations is presented in Table 6.2.

The improvement gained by adding the CryoSat-2 data without taking advantage of its improved features is marginal and the improvement could probably be gained by adding a equal amount of ERS-1 data. However, when taking the special features of the SAR data into account the improvement is almost 0.7 mGal, which is very promising. When more CryoSat-2 data becomes available and sea-ice is masked properly chances are that the SAR altimeter derived marine gravity field will improve even further.

6.2 Summary

The investigation carried out by the author using the new retracker software suite shows that improvements can be gained for gravity fields derived from SAR altimetry. The standard deviation of the difference between 5000 marine gravity field observations and gravity fields derived from a combination of traditional altimetry and SAR altimetry is found to be approximately 5.5 mGal. This is an improvement of 0.7 mGal compared to a gravity field derived from traditional altimetry only. This improvement should be seen in the light of the fact that the selected area has a highly dynamic gravity field. Furthermore, the effective along-track resolution of the new SAR altimeter data is increased by a factor of five compared to conventional altimetry data, leading to gravity fields of higher resolution. Finally,

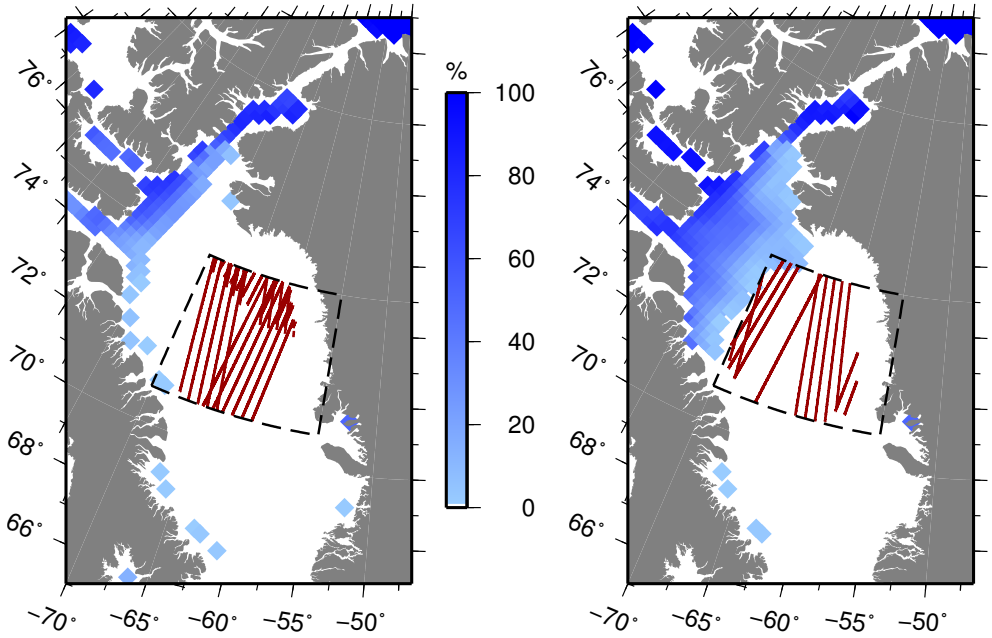

(a) Sea-ice concentration on October 15 (blue) and CryoSat-2 data from September 1 to October 15 (red).

(b) Sea-ice concentration on October 30 (blue) and CryoSat-2 data from October 16 to October 30 (red).

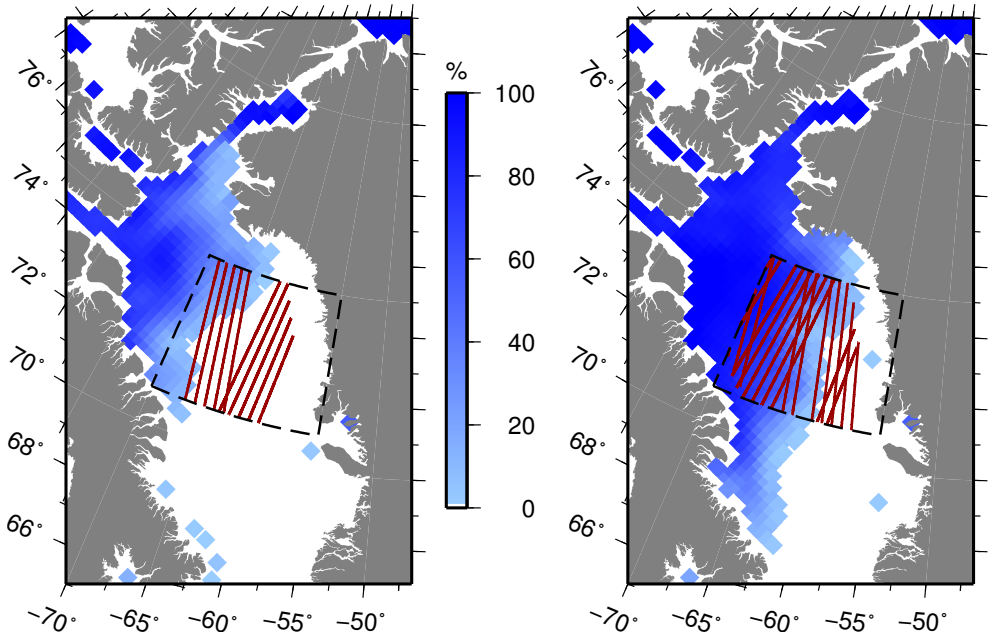

(c) Sea-ice concentration on November 10 (blue) and CryoSat-2 data from November 1 to November 10 (red).

(d) Sea-ice concentration on November 20 (blue) and CryoSat-2 data from November 11 to November 30 (red).

Figure 6.3: Sea-ice concentration in percent (blue color scale) on four selected dates and CryoSat-2 SAR tracks during the intermediate periods.

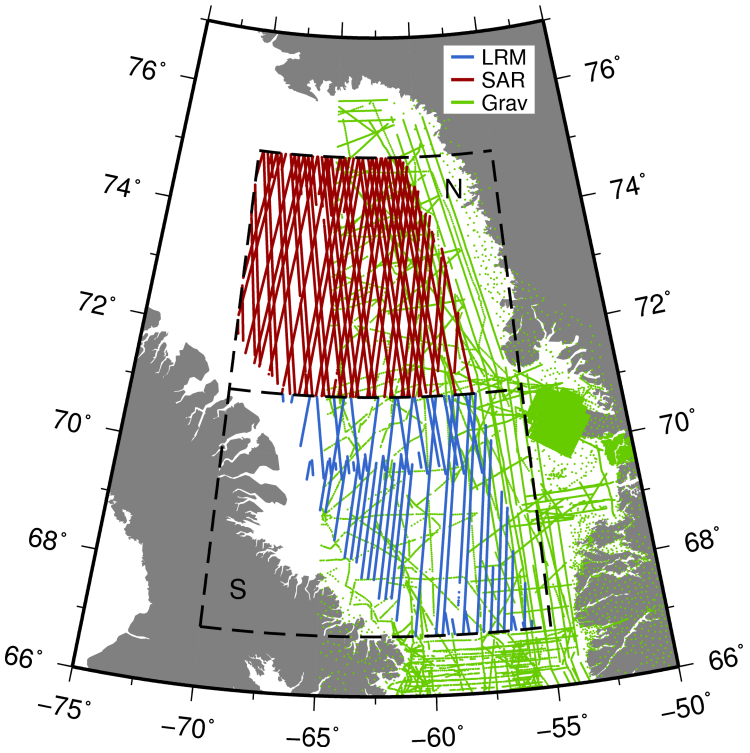

Figure 6.4: SAR (red), LRM (blue), and marine gravity data (green) in the Baffin Bay. From Stenseng and Andersen (2011).

the author has indicated a method to mask out errors caused by the presence of sea ice and sea ice debris in the altimetry data.

Chapter 7

Summary and Conclusion

The conventional radar altimeter have now had more than 30 years to mature and a whole suite of product is routinely being derived from the altimeter data. On April 11 2010, three days after the launch, the altimeter instrument on-board CryoSat-2 was switched on and marked the beginning of a new era in spaceborne radar altimetry. However, the road towards the SAR altimeter becoming a mature instrument is still long and many questions needs to be answered. The results presented in this work are an important step forward towards the understanding and utilization of SAR altimetry data.

In this thesis important properties of the new SAR radar altimeters were investigated and new methods to exploit the SAR altimeter data have been developed by the author and presented. The CryoSat-2 low level processor is still being updated to improve the performance and overcome the problems identified in the commissioning phase dataset.

During the PhD study a large suit of software tools has been developed by the author to handle the various data types, process data, and extract information. The tools range from simple routines to read the binary data files, over visualisation tools, to the implementation of the retracker suite, and the other methods developed by the author. In total, more than 20,000 lines of C++ code were written to enable the investigations presented in this thesis. The C++ code was written using the LGPL version of Qt Creator and the associated libraries (Nokia, 2011) and compiled using the GNU compiler (GCC steering committee, 2011). All figures, produced by the author, in this thesis were produced using the Generic Mapping Tool (Wessel and Smith, 2011).

7.1 Summary

The following will give a short summery of the newly developed methods and of the new results from the four focus areas; retracking of SAR waveforms, detection of annual layers in snow, detection of leads in sea-ice, and sea level mapping for marine gravity field determination.

7.1.1 Retracking of SAR Waveforms

The author has developed a software suite consisting of four retrackers and evaluated the performance with respect to CryoSat-2 SAR waveforms obtained over ocean. The performance of the developed retracker software suite has been tested and compared with the SAMOSA retracker, which is a state of the art SAR altimeter retracker based on a physical model.

The retracker suite has been tested on a set of real CryoSat-2 SAR data obtained September 26, 2010 over the Davis Strait and compared with the SAMOSA retracker. The OCOG and 80% threshold retrackers operate directly on the L1b samples and will return a value for all waveform regardless of the quality of the echo. The standard deviation of the OCOG and 80% threshold retrackers were 18 cm and 6 cm respectively. The five parameter beta retracker with exponential tail has a slightly smaller standard deviation of 5.6 cm and is capable of obtaining a fit for 93%. The simple CryoSat retracker was found to be unstable, resulting in a standard deviation of the mean of 43 cm for the 96% of the echoes where a fit could be obtained. Finally, the SAMOSA retracker exhibits the best performance by obtaining a fit for 97% of the waveforms with a standard deviation of 5 cm.

Is was shown that the five parameter Beta retracker with exponential tail and the 80% threshold retracker both performed well and was able to give reliable height estimates comparable to the SAMOSA retracker. However, the SAMOSA retracker is preferable if other parameters, like e.g significant wave height, is needed.

7.1.2 Detection of Annual Layers in Snow

A new method for detection of annual layers, associated with the autumn hoar, in the snow on the inland ice using ASIRAS data has been developed by the author. The method estimates the probability distribution for detection of layers as a function of depth. From these probability distributions individual layers can be identified, whereby the depth and uncertainty of the depth of the individual layers can be determined.

Using this new method, layers can be detected down to 15 m depth in the dry snow zone, which corresponds to the full range of the level 1b waveform. The maximal depth of 15 m is limited only by the size of the radar's sampling window and could potential detect deeper layers if the sampling window was increased. The average standard deviation of the depth of a detected layer is 7 cm in the dry snow zone and 15 cm in the percolation zone. Furthermore, it is found that two consecutive layers can be separated if the vertical distance is more than 20 cm.

It has been demonstrated that observations of the layering, from different years, can be used to determine the compaction of snow pack. Thereby, for the first time, giving the possibility of studying snow compaction on large scales using remote sensing techniques.

Due to the higher range sample spacing it is considered unlikely that the method can separate layers closer than 80 cm in CryoSat-2 SAR data.

7.1.3 Detection of Leads in Sea-Ice

Based on the return power and echo shape a new automatic lead detection method for ASIRAS data has been developed by the author. The method also includes a lowest level

filter to reject ambiguous and false lead detections, which would result in an erroneous instantaneous sea surface. Comparison with manual detected leads, using both airborne laser and SAR altimeter data, reveals that the difference between the two methods is less than 7 cm for 95% of the data and less than 2 cm for 50% of the data. The 2 cm corresponds to the estimated accuracy of the derived DEM. The discrepancy is primarily an effect of adding the laser altimetry data in the manual method, which improves the height determination.

The new automatic method has been applied on CryoSat-2 SAR data, but the waveform parameters were not considered to give a stable detection. Instead a new method was introduced by the author, where the return power and parameters describing the beam stack were used to detect leads. The lead detections were compared with an Envisat ASAR image, showing that all the major leads were detected and no false detections were made.

7.1.4 Sea Level and Marine Gravity Field Mapping Using SAR Altimetry

Three months of CryoSat-2 SAR data from the Baffin Bay were retracked, with the software suite developed by the author, and combined with ERS-1 data from the Geodetic Mission to derive a number of sea surfaces. From the sea surfaces three gravity fields were constructed; based on ERS-1 data only, based on ERS-1 and CryoSat-2 data in a standard processing, and based on ERS-1 and CryoSat-2 data in a optimised processing. The derived gravity fields were evaluated against 5000 marine gravity field observations obtained from ship.

When using the standard processing the improvement gained by adding CryoSat-2 data is marginal. However, the addition of CryoSat-2 data in an optimize processing gives an improvement of 0.7 mGal on the standard deviation, which is a significant improvement considering the highly dynamic gravity field in this area. As well as the improvement in the standard deviation, the along-track resolution is increased by a factor of five when using CryoSat-2 data. Finally, an investigation of the sea ice concentration obtained from SSMIS indicates that further improvements can be made by a careful rejection of data, which could be contaminated by sea ice.

7.2 Conclusion

With focus on retracking, snow on inland ice, the sea ice, and the ocean, the possibilities in the new SAR altimeters have been investigated by the author. For all focus areas methods for data exploitation have been presented and promising results have been obtained, even though the available amount of data is still sparse.

The retracker software suite developed by the author was tested on real Cryosat-2 data and the height determination capabilities were found to be comparable with the state of the art SAMOSA retracker.

A new automatic method for detection of annual layers in the firn on the Greenland Ice Sheet using ASIRAS data has been developed by the author. With this method it is, for the first time, possible to study the annual layer thickness at high vertical and horizontal resolution over large areas using remote sensing techniques. Furthermore, the author has developed a method to derive the compaction of the firn layers from repeated measurements.

The author has developed a new automatic method to detect leads in ASIRAS data with a performance comparable to manual identification of leads in a combined laser and

ASIRAS dataset. The automatic lead detection has been adapted to CryoSat-2 data, by the author, and the results showed that the new method is very promising, but that it needs a more thorough investigation using data from a longer period of time in order to capture the general changes in the sea ice over the four seasons.

The developed retracker software suite has been applied on three months of real CryoSat-2 data from the Baffin Bay to derive sea surface and gravity field maps. In order to obtain an independent validation of the sea surface, the data has been used to calculate a gravity field and compared with in situ measurements of the gravity field. The investigation shows that the spatial resolution can be increased and that a significant improvement of the gravity field can be gained by adding CryoSat-2 SAR data.

The CryoVEx 2011 was the first major campaign, which combined airborne and spaceborne SAR altimetry observations with in situ measurements. The dataset obtained will provide an important insight into the scaling between the three sets of observations. Furthermore, with a third measurement of the snow layering along the EGIG line, it will be possible to verify the found compaction and to give an independent estimate of the uncertainties on the compaction.

The new version of the SAR and SARin processor for the CryoSat-2 data is expected to solve the issues found in the SAR and SARin data and thereby provide data of an even higher quality than the first data release used in this work. The improvement in the processor will, at some stage, be complemented by the implementations of the instrument corrections obtained during the commissioning phase.

7.3 Outlook

The new methods developed by the author contribute to ensure a successful utilization of data from the Cryosat-2 mission. The developed software suite may be used for retracking Cryosat SAR data for a variety of applications.

With continued ASIRAS observations over the dry snow zone of the Greenland Ice Sheet it will be possible to accurately map the accumulation and changes in the accumulation pattern. These accumulation maps could play a significant role in the understanding and improvement of the climate models and the numerical weather models in the Arctic. The identification of leads in SAR altimeter data, made possible by the method developed by the author, is crucial not only for sea ice freeboard determination but also for an improved determination of the Arctic sea surface height. Also the recovery of high resolution sea level data is expected to become important in studies of the ocean circulation and the marine gravity field in the coastal zones.

The Sentinel-3 satellites will be launched in the near future carrying, amongst several other instruments, a dual frequency altimeter with SAR capabilities. Sentinel-3 is part of the EU GMES initiative and will be providing observations of the sea surface height, sea ice thickness, as well as other marine observations. The sea surface height and sea ice thickness can be derived by applying some of the methods and tolls developed by the author. The experiences gained from the analysis of similar data from Cryosat-2 are important for the implementation of the Sentinal-3 mission into the relevant GMES services.

The presented investigations and new methods developed by the author will be important for the understanding and use of CryoSat-2, ASIRAS, Sentinel-3, and other SAR altimeter products now and in the future.

Bibliography

Advanced Computer Systems (2009). *CryoSat Ground Segment. Instrument Processing Facility L1b. Product Specification Format.* European Space Agency, 4.6 edition. Ref.: CS-RS-ACS-GS-5106.

Aguirre, M., Berruti, B., Bezy, J.-L., Drinkwater, M., Heliere, F., Klein, U., Mavrocordatos, C., Greco, B., and Benviniste, J. (2007). Sentinel-3. the ocean and medium-resolution land mission for GMES operational services.

Andersen, O. B. (2008). SAMOSA WP3 technical note. recovery of short wavelength geophysical signals and short spatial scale sea surface height/slope signals. Technical report, DTU-Space.

Andersen, O. B. and Knudsen, P. (2009). DNSC08 mean sea surface and mean dynamic topography models. *Journal of Geophysical Research - Part C - Oceans*, 114(11).

Andersen, O. B., Knudsen, P., and Berry, P. A. M. (2010). The DNSC08GRA global marine gravity field from double retracked satellite altimetry. *Journal of Geodesy*, 84(3):191–199.

Beaven, S. G., Lockhart, G. L., Gogineni, S. P., Hosseinmostafa, A. R., Jezek, K., Gow, A. J., K.Perovich, D., Fung, A. K., and Tjuatja, S. (1995). Laboratory measurements of radar backscatter from bare and snow-covered saline ice sheets. *International Journal of Remote Sensing*, 16(5):851.

Brenner, A. C., DiMarzio, J. P., and Zwally, H. J. (2007). Precision and accuracy of satellite radar and laser altimeter data over the continental ice sheets. *IEEE Transactions on Geoscience and Remote Sensing*, 45(2):321–331.

Brown, G. (1977). The average impulse response of a rough surface and its applications. *IEEE Transactions on Antennas and Propagation*, 25(1):67–74.

Comiso, J. C., Wadhams, P., Krabill, W. B., Swift, R. N., Crawford, J. P., and III, W. B. T. (1991). Top/bottom multisensor remote sensing of arctic sea ice. *Journal of Geophysical Research*, 96(C2):2693–2709.

Cotton, P. D. (2010). SAMOSA (SAR Altimetry MOde Studies and Applications). http://www.satoc.eu/projects/samosa/.

Cullen, R. (2010). *CryoVEx Airborne Data Product Description*. European Space Agency, 2.6.1 edition. Ref.:CS-LI-ESA-GS-0371.

Cullen, R., Wingham, D. J., Viau, P., Francis, C. R., and Mavrocordatos, C. (2007). Esa's CryoSat-2 multi-mode level 0 to level 1b science processors–algorithm design and prelaunch verification with ASIRAS. In Agency, E. S., editor, *Envisat Symposium 2007*.

Cullen, R. A. and Wingham, D. J. (2002). CryoSat level 1b processing algorithms and simulation results. In *Geoscience and Remote Sensing Symposium, 2002. IGARSS '02. 2002 IEEE International*, volume 3, pages 1762–1764. Centre for Polar Obs. & Modelling, Univ. Coll. London, UK, IEEE.

Davis, C. H. (1997). A robust threshold retracking algorithm for measuring ice-sheet surface elevation change from satellite radar altimeters. *IEEE Transactions on Geoscience and Remote Sensing*, 35(4):974–979.

Davis, C. H., Kluever, C. A., Haines, B. J., Perez, C., and Yoon, Y. T. (2000). Improved elevation-change measurement of the southern greenland ice sheet from satellite radar altimetry. *IEEE Transactions on Geoscience and Remote Sensing*, 38(3):1367–1378.

de la Peña, S., Nienow, P., Shepherd, A., Helm, V., Mair, D., Hanna, E., Huybrechts, P., Guo, Q., Cullen, R., and Wingham, D. J. (2010). Spatially extensive estimates of annual accumulation in the dry snow zone of the greenland ice sheet determined from radar altimetry. *The Cryosphere*, 4(4):467–474.

Deng, X. and Featherstone, W. E. (2006). A coastal retracking system for satellite radar altimeter waveforms: Application to ers-2 around australia. *Journal of Geophysical Research*, 111(C6).

Drinkwater, M. (1991). Ku band airborne radar altimeter observations of marginal sea ice during the 1984 marginal ice zone experiment. *Journal of Geophysical Research*, 96(C3):4555–4572.

ESA (2011). ESA earthnet: ASAR. http://envisat.esa.int/instruments/asar/.

European Space Agency (2010). GMES medium resolution land and ocean mission. data sheet. E-published.

Fetterer, F., Drinkwater, M., Jezek, K., S.W.C.Laxon, Onstott, R., and Ulander, L. (1992). Sea ice altimetry. *Geophysical Monograph*, 68:111–135.

Forsberg, R. and Skourup, H. (2005). Arctic ocean gravity, geoid and sea-ice freeboard heights from icesat and grace. *Geophysical Research Letters*, 32(L21502).

Francis, C. R. (2007). CryoSat mission and data description. Technical Report CS-RP-ESA-SY-0059, European Space Agency.

GCC steering committee (2011). GCC, the GNU compiler collection. http://gcc.gnu.org/.

Giles, K. A., Laxon, S. W., and Ridout, A. L. (2008). Circumpolar thinning of arctic sea ice following the 2007 record ice extent minimum. *Geophysical Research Letters*, 35(22):L22502.

Giles, K. A., Laxon, S. W., Wingham, D. J., Wallis, D. W., Krabill, W. B., Leuschen, C. J., McAdoo, D., Manizade, S. S., and Raney, R. K. (2007). Combined airborne laser and radar altimeter measurements over the fram strait in may 2002. *Remote Sensing of Environment*, 111:182–194.

Gommenginger, C. and Srokosz, M. (2009). SAMOSA WP5.3 technical note. development & testing of SAR altimeter waveform theoretical retracker. Technical report, National Oceanography Center, Southampton.

Hamilton, G. S. (2004). Topographic control of regional accumulation rate variability at south pole and implications for ice-core interpretation. *Annals of Glaciology*, 39:214–218(5).

Hawley, R. L., Morris, E. M., Cullen, R., Nixdorf, U., Shepherd, A. P., and Wingham, D. J. (2006). Asiras airborne radar resolves internal annual layers in the dry-snow zone of greenland. *Geophysical Research Letters*, 33.

Hayne (1980). Radar altimeter mean return waveforms from near-normal-incidence ocean surface scattering. *IEEE Transactions on Antennas and Propagation*, AP-28(5):687–692.

Heiskanen, W. A. and Moritz, H. (1999). *Physical Geodesy*. Institute of Physical Geodesy, Technical University, Graz, Austria.

Helm, V., Hendricks, S., Goebell, S., Rack, W., Haas, C., Nixdorf, U., and Boebel, T. (2006). CryoVex 2004 and 2005 (BoB) data acquisition and final report. Technical report, Alfred Wegener Institute.

Helm, V., Rack, W., Cullen, R., Nienow, P., Mair, D., Parry, V., and Wingham, D. J. (2007). Winter accumulation in the percolation zone of greenland measured by airborne radar altimeter. *Geophysical Research Letters*, 34(L06501).

Helm, V. and Steinhage, D. (2008). CryoVEx 2007. data accquisition and final processing report. Technical report, Alfred Wegener Institute for Polar and Marine Research.

Helm, V., Steinhage, D., Dietrich, R., and Rülke, A. (2009). CryoVEx 08/09 - antarctica. data acquisition and final processing report. (draft). Technical report, Alfred Wegener Institute and Technische Universität Dresden.

Hendricks, S., Stenseng, L., Helm, V., and Haas, C. (2010). Effects of surface roughness on sea ice freeboard retrieval with an airborne ku-band sar radar altimeter. In *Geoscience and Remote Sensing Symposium (IGARSS), 2010 IEEE International*, pages 3126 –3129.

Hendricks, S., Stenseng, L., Helm, V., Hvidegaard, S. M., Haas, C., and Hanson, S. (2011). K_u-band radar penetration into snow over arctic sea ice derived from airborne laser and radar altimeter freeboard retrievals. *Journal of Geophysical Research*.

Hvidegaard, S. M., Forsberg, R., Helm, V., Hendricks, S., Skourup, H., Stenseng, L., Hanson, S., and Haas, C. (2009). CryoVEx 2008. final report. Technical Report 2, DTU-Space, National Space Institute.

Hvidegaard, S. M., Forsberg, R., Skourup, H., and Stenseng, L. (2010). Airborne campaigns for cryosat pre-launch calibration and validation. In *Living Planet Symposium 2010*. European Space Agency.

Jensen, J. R. and Raney, R. K. (1998). Delay doppler radar altimeter: better measurement precision. In *IEEE Geoscience and Remote Sensing Symposium IGARSS'98*.

Keller, K., Hvidegaard, S. M., Forsberg, R., Dalå, N. S., Skourup, H., and Stenseng, L. (2004). Airborne lidar and radar measurements over sea ice and inland ice for cryosat validation: CryoVEx 2003 - final report. Technical Report 25, National Survey and Cadastre.

Lacroix, P., Dechambre, M., Legrésy, B., Blarel, F., and Rémy, F. (2008). On the use of the dual-frequency envisat altimeter to determine snowpack properties of the antarctic ice sheet. *Remote Sensing of Environment*, 112:1712–1729.

Laxon, S. W., Peacock, N., and Smith, D. (2003). High interannual variability of sea ice thickness in the arctic region. *Nature*, 425(6961):947–950.

Lentz, H., Braun, H.-M., Younis, M., Fischer, C., Wiesbeck, W., and Mavrocordatos, C. (2002). Concept and realization of an airborne SAR/Interferometric radar altimeter system (ASIRAS). *IEEE International Geoscience and Remote Sensing Symposium*, 6:3099–3101 vol.6.

Leuschen, C. J. and Raney, R. K. (2005). Initial results of data collected by the apl d2p radar altimeter over land and sea ice. *Johns Hopkins APL Technical Digest*, 26(2):114–122.

Looyenga, H. (1965). Dielectric constants of heterogeneous mixtures. *Physica*, 31(3):401–406.

Lourakis, M. (December 2009). levmar: Levenberg-marquardt nonlinear least squares algorithms in C/C++. [web page] `http://www.ics.forth.gr/~lourakis/levmar/`. Last accessed on August 23, 2010.

MacArthur, J. (1976). Design of the SEASAT-A radar altimeter. *OCEANS*, 8:222–229.

Marquardt, D. W. (1963). An algorithm for least-squares estimation of nonlinear parameters. *Journal of the Society for Industrial and Applied Mathematics*, 11(2):431–441.

Martin, T. V., Zwally, H. J., Brenner, A. C., and Bindschadler, R. A. (1983). Analysis and retracking of continental ice sheet radar altimeter waveforms. *Journal of Geophysical Research*, 88(C3):1608–1616.

Martin-Puig, C. and Ruffini, G. (2009). SAMOSA WP5 technical note. SAR altimeter retracker performance bound over water surfaces. Technical report, STARLAB.

Martin-Puig, C., Ruffini, G., and Marquez, J. (2009). SAMOSA WP4 technical note. theoretical model for SAR altimeter mode processed echoes over ocean surfaces - revised. Technical report, STARLAB.

Mätzler, C. and Wegmüller, U. (1987). Dielectric properties of fresh-water ice at microwave frequencies. *Journal of Physics D: Applied Physics*, 20(12):1623–1630.

Mavrocordatos, C., Attema, E., Davidson, M., Lentz, H., and Nixdorf, U. (2004). Development of ASIRAS (airborne SAR/Interferometric altimeter system). In *IGARSS 2004: IEEE INTERNATIONAL GEOSCIENCE AND REMOTE SENSING SYMPOSIUM PROCEEDINGS, VOLS 1-7*, pages 2465–2467.

Morris, E. M. and Cooper, J. D. (2003). Instruments and methods. density measurements in ice boreholes using neutron scattering. *Journal of Glaciology*, 49(167):599–604.

Nicolaus, M., Hendricks, S., Stenseng, L., Helm, V., Gerdes, R., and Haas, C. (2010). Cryosat-2 pre-launch validation measurements on arctic sea ice. In *Living Planet Symposium 2010*. European Space Agency.

Nokia (2011). Qt. http://qt.nokia.com.

Nolin, A., Armstrong, L., and Maslanik, J. (1998). Near-real-time SSM/I-SSMIS EASE-Grid daily global ice concentration and snow extent. Digital Media. Data from September to October 2010.

Pavlis, N. K., Holmes, S. A., Kenyon, S., and Factor, J. K. (2008). An earth gravitational model to degree 2160: Egm2008. In *the 2008 General Assembly of the European Geosciences Union*. European Geosciences Union. presented at the 2008 General Assembly of the European Geosciences Union, Vienna, Austria, April 13-18, 2008.

Peacock, N. R. and Laxon, S. W. (2004). Sea surface height determination in the arctic ocean from ers altimetry. *Journal of Geophysical Research*, 109(C7):14 pp.

Poulsen, S. K., Stenseng, L., Skourup, H., Pedersen, L. T., Forsberg, R., and Sørensen, L. S. (2011). Initial results of CryoSat-2 data from the arctic. In *CryoSat-2 Validation Workshop*. European Space Agency.

Raney, R. (1998). The Delay/Doppler radar altimeter. *IEEE Transactions on Geoscience and Remote Sensing*, 36(5):1578–1588.

Raney, R. K. (2010). CryoSat-2 SAR-mode looks revisited. In Lacoste-Francis, H., editor, *Living Planet Symposium 2010*, ESTEC, PO Box 299, 2200 AG Noordwijk, The Netherlands. European Space Agency, ESA Communications.

Rodriguez, E. (1988). Altimetry for non-gaussian oceans: height biases and estimation of parameters. *Journal of Geophysical Research*, 93(C11):14107–14120.

Rodriguez, E. and Chapman, B. (1989). Extracting ocean surface information from altimeter returns: the deconvolution method. *Journal of Geophysical Research*, 94(C7):9761–9778.

Sandwell, D. T. and Smith, W. H. F. (1997). Marine gravity anomaly from geosat and ERS 1 satellite altimetry. *Journal of Geophysical Research*, 102(B5):10039–10054.

Skourup, H., Forsberg, R., Hanson, S., Hvidegaard, S. M., Morris, E. M., Nienow, P., Poulsen, S. K., and Stenseng, L. (2011). Airborne campaigns for CryoSat prelaunch calibration and validation. In *CryoSat-2 Validation Workshop*. European Space Agency.

Sørensen, L. S., Simonsen, S. B., Nielsen, K., Lucas-Picher, P., Spada, G., Adalgeirsdottir, G., Forsberg, R., and Hvidberg, C. S. (2010a). Mass balance of the greenland ice sheet – a study of icesat data, surface density and firn compaction modelling. *The Cryosphere Discussions*, 4:2103–2141.

Sørensen, L. S., Stenseng, L., Simonsen, S. B., Forsberg, R., Poulsen, S. K., and Helm, V. (2010b). Greenland ice sheet changes from space using laser, radar and gravity. In Lacoste-Francis, H., editor, *Living Planet Symposium 2010*, ESTEC, PO Box 299, 2200 AG Noordwijk, The Netherlands. European Space Agency, ESA Communications.

Stenseng, L. (2009). SAMOSA WP8 technical note. validation using airborne ASIRAS data. Technical report, DTU-Space.

Stenseng, L. and Andersen, O. B. (2011). First results of recovery of short wavelength gravity field signals from CryoSat-2 data. In *CryoSat-2 Validation Workshop*. European Space Agency.

Stenseng, L. and Gommenginger, C. (2011). SAMOSA2 WP2300 technical note. validation against ASIRAS. Technical Report 1.1, DTU-Space.

Stenseng, L., Hvidegaard, S. M., Skourup, H., Forsberg, R., Andersen, C. J., Hanson, S., Cullen, R., and Helm, V. (2007). Airborne lidar and radar measurements in and around Greenland, CryoVEx 2006. Technical Report 9, Danish National Space Center.

Stenseng, L., Morris, E. M., and Helm, V. (2011). High resolution detection of annual layers in firn using airborne asiras radar data. *Geophysical Research Letters*. In preparation.

Torge, W. (1991). *Geodesy*. Walter de Gruyter, 2nd edition.

Vignudelli, S., Kostisanoy, A. G., Cipollini, P., and Benviniste, J., editors (2011). *Coastal Altimetry*. Springer-Verlag.

Wadhams, P., III., W. B. T., Krabill, W. B., Swift, R. N., Comiso, J. C., and Davis, N. R. (1992). Relationship between sea ice freeboard and draft in the arctic basin, and implications for ice thickness monitoring. *Journal of Geophysical Research*, 97(C12):20325–20334.

Walsh, E. J. (1982). Pulse-to-pulse correlation in satellite radar altimetry. *Radio Science*, 17:786–800.

Warren, S. G., Rigor, I. G., Untersteiner, N., Radionov, V. F., Bryazgin, N. N., Aleksandrov, Y. I., and Colony, R. (1999). Snow depth on arctic sea ice. *Journal of Climate*, 12(6):1814–1829.

Wessel, P. and Smith, W. H. F. (2011). The generic mapping tools. GMT. http://www.soest.hawaii.edu/gmt.

Willatt, R. C., Giles, K. A., Laxon, S. W., Stone-Drake, L., and Worby, A. P. (2010). Field investigations of ku-band radar penetration into snow cover on antarctic sea ice. *IEEE Transactions on Geoscience and Remote Sensing*, 48(12):365–372.

Willatt, R. C., Laxon, S. W., Giles, K. A., Cullen, R., Haas, C., and Helm, V. (2011). Ku-band radar penetration into snow cover on arctic sea ice using airborne data. *Annals of Glaciology*, 52(57):197–205.

Wingham, D. J., Forsberg, R., Laxon, S. W., Lemke, P., Miller, H., Raney, R. K., Sandven, S., Scharroo, R., Vincent, P., and Rebhan, H. (2001). CryoSat calibration & validation concept. Technical report, Center for Polar Observation & Modelling.

Wingham, D. J., Francis, C. R., Baker, S., Bouzinac, C., Brockley, D., Cullen, R., de Chateau-Thierry, P., Laxon, S. W., Mallow, U., Mavrocordatos, C., Phalippou, L., Ratier, G., Rey, L., Rostan, F., Viau, P., and Wallis, D. W. (2006). CryoSat: A mission to determine the fluctuations in earth's land and marine ice fields. *Advances in Space Research*, 37:841–871.

Wingham, D. J., Rapley, C. G., and Griffiths, H. (1986). New techniques in satellite altimeter tracking systems. In *Proceedings of the IGARSS Symposium, Zurich*, pages 1339–1344. IEEE.

Zwally, H. J., Brenner, A. C., Major, J. A., and Bindschadler, R. A. (1990). Satellite radar altimetry over ice, volumes 1, 2, and 4. Reference publication 1233, NASA.

Zwally, H. J., Giovinetto, M. B., Li, J., Cornejo, H. G., Beckley, M. A., Brenner, A. C., Saba, J. L., and Yi, D. (2005). Mass changes of the greenland and antarctic ice sheets and shelves and contributions to sea-level rise: 1992-2002. *Journal of Glaciology*, 51(175):509.

Appendix A

Publications

A.1 High Resolution Detection of Annual Layers in Firn Using Airborne ASIRAS Radar Data

Paper submitted to Geophysical Research Letters. Submitted 28-01-2011. Stenseng et al. (2011)

High resolution detection of annual layers and densification in firn using airborne ASIRAS radar data

Lars Stenseng[1], Elizabeth M. Morris[2] and Veit Helm[3]

A new, automatic, high-resolution method is introduced to map annual layers in snow down to 15 m depth. Using this method on a set of ASIRAS profiles collected over the Greenland Ice Sheet in 2006 and 2008, we have been able to estimate the rate of densification of snow as it moves downwards relative to the ice-sheet surface and thus derive density gradients along the flight profile.

Processing of individual waveforms before along-track averaging allows reliable detection of radar peaks even when their depth is highly variable from waveform to waveform. This increases the number of traceable layers dramatically compared to other studies.

A statistical approach is used to estimate the depth and likelihood of detecting a layer, together with the uncertainty in the estimated depth.

The method is shown to work from the percolation zone through the dry snow zone at the ice-divide and the derived layers compare well with in situ field measurements of density profiles.

1. Introduction

Converting ice sheet volume changes observed from satellite altimetry to mass changes is a major challenge and requires detailed knowledge of the compaction processes in the snow layer. Studies by *Sørensen et al.* [2010] indicate that neglecting snow compaction introduces an error of up to 57 GT/yr over the Greenland Ice Sheet. Validation of firn compaction models is therefore needed to improve the accuracy of mass balance estimates. Furthermore accumulation rates are important to constrain climate models.

The ASIRAS instrument [*Mavrocordatos et al.*, 2004] was built as an airborne calibration and validation instrument for the SAR/Interferometric Radar Altimeter (SIRAL) instrument on CryoSat-2 [*Wingham et al.*, 2006]. The two instruments have similar properties, but ASIRAS features a higher bandwidth and thus better range resolution.

A relationship between ASIRAS return power and snow density has been demonstrated by *Hawley et al.* [2006] and used to estimate winter accumulation in the percolation zone [*Helm et al.*, 2007] and accumulation rates in the dry snow zone [*de la Peña et al.*, 2010].

The layers derived using the new method introduced here are compared with neutron-probe measurements of the density profile [*Morris and Cooper*, 2003] in the percolation zone and the dry snow zone.

[1]DTU-Space, Technical University of Denmark, Juliane Maries Vej 30, DK-2100 Copenhagen, Denmark

[2]Scott Polar Research Institute, University of Cambridge, Lensfield Road, Cambridge CB2 1ER, England

[3]Alfred Wegener Institute for Polar and Marine Research, Am Handelshafen 12, 27570 Bremerhaven, Germany

0094-8276/11/$5.00

2. Airborne and In situ Data

The EGIG line crosses the Greenland Ice Sheet from East to West in the central part covering all major regimes of the ice-sheet. Having a combination of a long history and large amount of existing data, the traverse is an ideal choice of validation area for CryoSat-2. As part of the ESA CryoSat Validation Experiment (CryoVEx) campaigns, radar data were collected along the EGIG line during spring 2006 and 2008 [*Stenseng et al.*, 2007; *Hvidegaard et al.*, 2009]. Neutron-probe data were collected in spring 2006 at several sites along the airborne track, whereof data from two sites are included for validation.

3. Determination of Layer Depth

To obtain the respective depth of the layers all waveforms must be aligned, using the surface as a common zero reference. The surface is estimated from the individual radar waveforms using a threshold retracking of the leading edge. Outliers are removed from the surface estimations and the remaining estimates are smoothed to obtain a reference height which is subtracted from the individual waveforms to align them at the surface.

Assuming the density is known for the entire profile and that the snow is a mixture of small ice particles and air, the density can be converted to permittivity and the refractive index can be estimated [*Looyenga*, 1965; *Mätzler and Wegmüller*, 1987]. This allows the radar time-of-travel of a layer to be converted to depth below the surface. An iterative method is used to determine the density, starting with the assumption that density at all depths is constant and equal to the surface density (ρ_0).

The depths of all peaks with respect to the surface are found in each waveform using a local maximum routine. The local maximum routine operates in a small sliding window and are thus not sensitive to variations in layer thickness.

Waveforms are collected in groups along-track and peaks are counted in 2 cm depth intervals for the entire range of all waveforms in the group. To get reliable statistic, waveforms are collected in groups of approximate 450 waveforms equal to 1 km along-track. Counts in a group are normalized using the number of waveforms in the group to obtain the probability for detecting a layer at a given depth.

Finally a Gaussian is fitted to the distribution of each detected layer to obtain a mean depth and standard deviation on the depth. The standard deviation of the mean is generally less than 6 cm at T41 rising to more than 10 cm at T09.

All waveforms from the 2006 radar profile are plotted in Figure 1 which shows, in color coding, the probability of detecting an annual layer as a function of depth and longitude along the profile. In the dry snow zone, layers are easily detected within the entire range of the processed radar waveform (Figures 1 and 3 middle and right) and layers spaced

less than 20 cm vertically are clearly separated. West of -44° the increasing amount of refrozen melt-water and surface melt start to mask out the deeper layers, making them undetectable in the radar data. At the T09 site in the percolation zone (Figures 1 and 2) layers are detectable down to -4.5 m; below this depth detections are randomly scattered and no longer associated with a layer.

4. Estimation of Compaction

Aligning the layer probability functions at T41 from 2006 and 2008 and comparing layer thickness (T_i) and depth (d_i) (Figure 3 center and right) it is possible to estimate the average compaction as a linear increasing density ($\delta\rho$), expressed in Equation 1.

$$\delta\rho = \frac{\rho_0 \cdot (T_i^{2006} - T_i^{2008})}{d^{2008} - d^{2006} + (T_i^{2008} - T_i^{2006})/2} \quad (1)$$

The linear increasing density profile is used to perform a fine correction of the layer depths, before the final density gradient is determined.

5. Validation Against N-probe Data

In the upper 6 m at the T41 site (Figure 3) the high density layers in the in situ data and the layer detection probability peaks are aligned in an almost one to one correspondence. Below this depth the annual density contrast starts to fade in the in situ density profile, but the layers are still clearly detectable in the radar data. The density gradient derived from ASIRAS data at T41 (Figure 3 left) captures the mean density gradient found in the in situ density profile.

In the percolation zone at T09 (Figure 2) there is a good agreement between the detected layers at -0.8 m and -2.3 m and the in situ data, but below this the layering is disturbed.

6. Discussion and Conclusion

A good agreement between the detected layer distributions in 2006 and 2008 is found (Figure 3), when neglecting the first detection associated with the peak found at the end of the leading edge. It is noted that the distribution of layer probability from a given year is conserved and thereby recognisably when comparing different years and this strongly indicates that the shape of the distribution from a given year can be used as a proxy for the snow properties.

Furthermore, a good agreement between layers detected in radar and neutron-probe data is found in the upper layers, with clear density contrasts between the summer and the winter snow. At larger depth the layers detected with the method presented here gives a clear unambiguous identification of the layers and can thus be used as isocrons for dating the in situ density profiles or other datasets along the profile.

This new approach to analyse the radar data enables detailed studies on accumulation and compaction at high resolution in the dry snow zone of Greenland using airborne ASIRAS data, offering a remote sensing dataset to evaluate and calibrate mass balance models and regional climate models.

Acknowledgments. The authors would like to thank ESA and the entire CVRT for the huge effort put into the CryoVEx campaigns.

References

Cullen, R. (2010), *CryoVEx Airborne Data Product Description*, European Space Agency, 2.6.1 ed.

de la Peña, S., P. Nienow, A. Shepherd, V. Helm, D. Mair, E. Hanna, P. Huybrechts, Q. Guo, R. Cullen, and D. J. Wingham (2010), Spatially extensive estimates of annual accumulation in the dry snow zone of the greenland ice sheet determined from radar altimetry, *The Cryosphere*, *4*(4).

Hawley, R. L., E. M. Morris, R. Cullen, U. Nixdorf, A. P. Shepherd, and D. J. Wingham (2006), Asiras airborne radar resolves internal annual layers in the dry-snow zone of greenland, *Geophysical Research Letters*, *33*.

Helm, V., W. Rack, R. Cullen, P. Nienow, D. Mair, V. Parry, and D. J. Wingham (2007), Winter accumulation in the percolation zone of greenland measured by airborne radar altimeter, *Geophysical Research Letters*, *34*.

Hvidegaard, S. M., R. Forsberg, V. Helm, S. Hendricks, H. Skourup, L. Stenseng, S. Hanson, and C. Haas (2009), Cryovex 2008. final report, *Technical Report 2*, DTU-Space.

Looyenga, H. (1965), Dielectric constants of heterogeneous mixtures, *Physica*, *31*.

Mätzler, C., and U. Wegmüller (1987), Dielectric properties of fresh-water ice at microwave frequencies, *Journal of Physics D: Applied Physics*, *20*(12).

Mavrocordatos, C., E. Attema, M. Davidson, H. Lentz, and U. Nixdorf (2004), Development of ASIRAS (airborne SAR/Interferometric altimeter system).

Morris, E. M., and J. D. Cooper (2003), Instruments and methods. density measurements in ice boreholes using neutron scattering, *Journal of Glaciology*, *49*(167).

Sørensen, L. S., S. B. Simonsen, K. Nielsen, P. Lucas-Picher, G. Spada, G. Adalgeirsdottir, R. Forsberg, and C. S. Hvidberg (2010), Mass balance of the greenland ice sheet ? a study of icesat data, surface density and firn compaction modelling, *The Cryosphere Discussions*, *4*(4).

Stenseng, L., S. M. Hvidegaard, H. Skourup, R. Forsberg, C. J. Andersen, S. Hanson, R. Cullen, and V. Helm (2007), Airborne lidar and radar measurements in and around Greenland, CryoVEx 2006, *Technical Report 9*, Danish National Space Center.

Wingham, D. J., C. R. Francis, S. Baker, C. Bouzinac, D. Brockley, R. Cullen, P. de Chateau-Thierry, S. W. Laxon, U. Mallow, C. Mavrocordatos, L. Phalippou, G. Ratier, L. Rey, F. Rostan, P. Viau, and D. W. Wallis (2006), CryoSat: A mission to determine the fluctuations in earth's land and marine ice fields, *Advances in Space Research*, *37*.

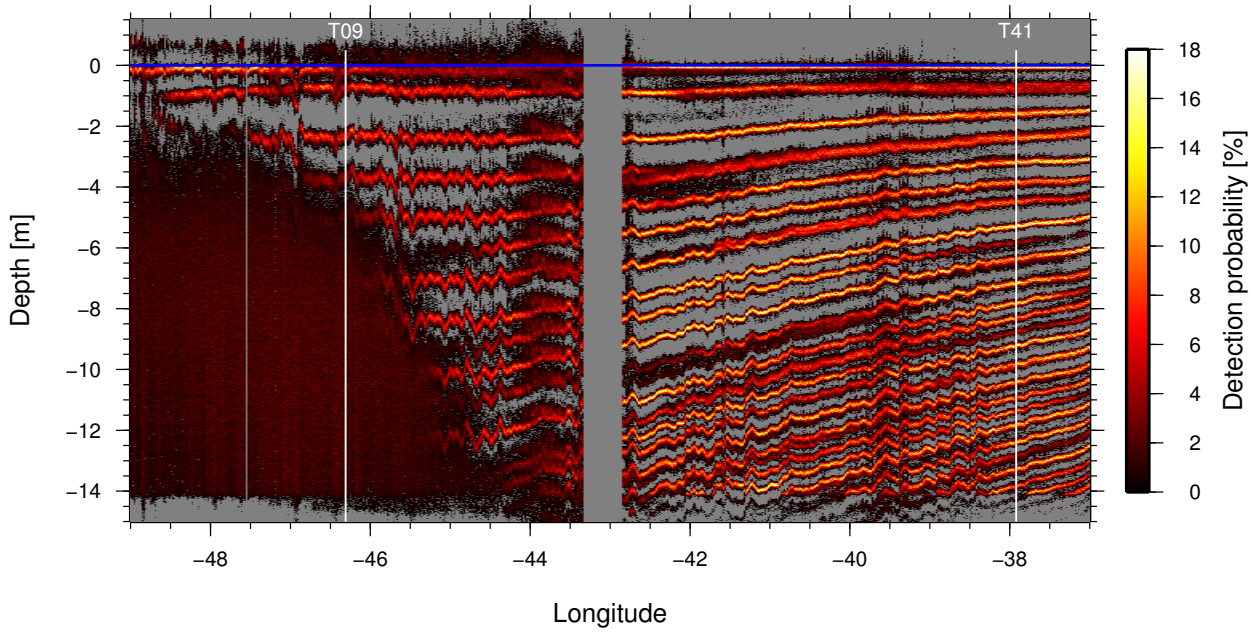

Figure 1. Probability for detecting a peak in ASIRAS data from spring 2006, over the 485 km profile from the percolation zone in west to the dry snow zone to the east (in colour-scale, gray indicates no detections). The gap in the profile around -43 degrees longitude is due to a lack of radar data. The surface is estimated from the radar data using a simple retracker (blue line). The position of the in-situ N-probe measurement are indicated with white.

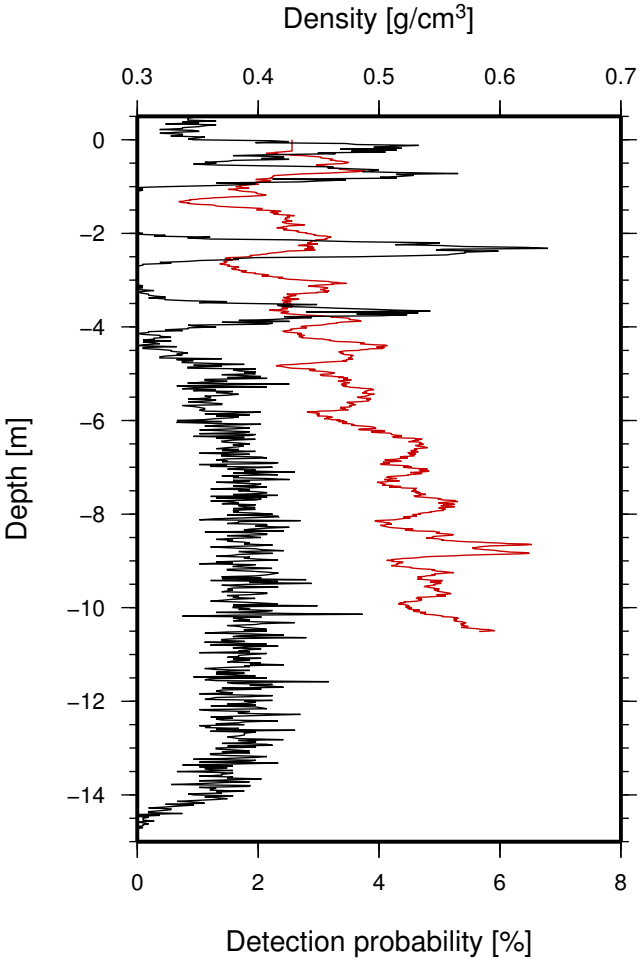

Figure 2. Relationship between layer detection probability and layer density at site T9 in the percolation zone observed in spring 2006. The probability (lower axis) for detecting a peak in ASIRAS data at a given depth relative to the surface (black) and the density (upper axis) as function of depth derived from N-Probe observations (red).

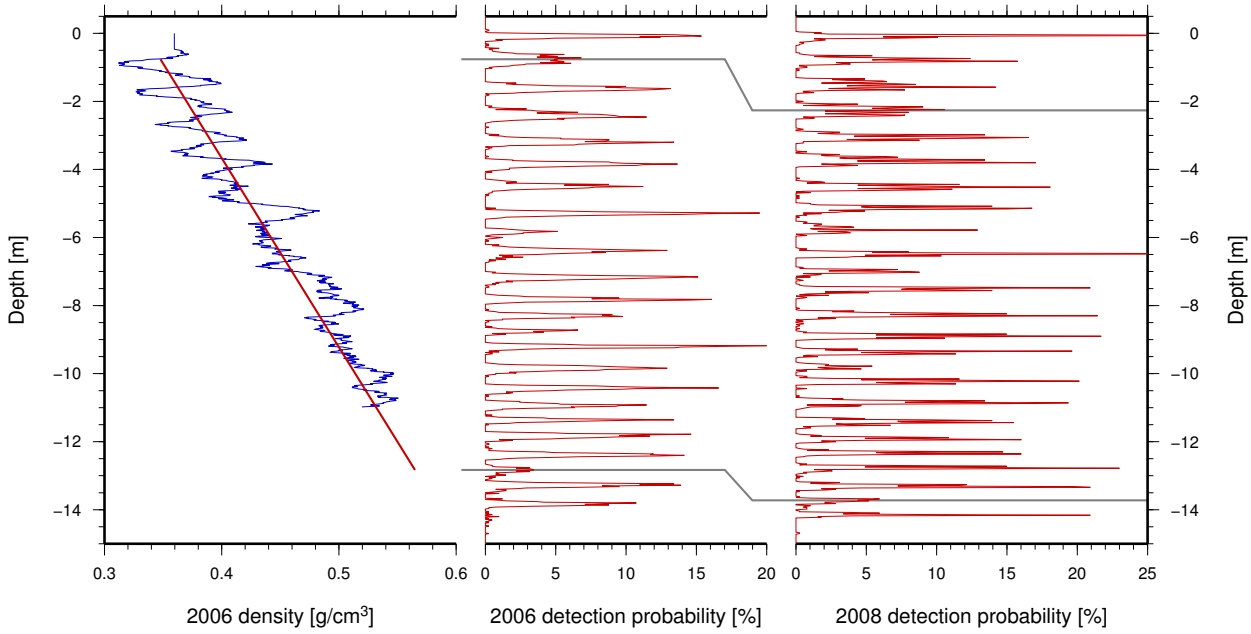

Figure 3. Comparison of in situ density profile, detected layers in ASIRAS data and estimated compaction. The left plot shows the measured density profile (blue) at T41 derived from N-probe data and the density profile derived from ASIRAS data (red). The middle and right plot shows the derived layer detection probabilities for 2006 and 2008 respectively (red). The two gray lines indicate the top and bottom layer used to derive the compaction.

A.2 First Results of Recovery of Short Wavelength Gravity Field Signals from CryoSat-2 Data

Proceedings paper to ESA CryoSat Validation Workshop, Frascati, Italy, February 1-3 2011. Submitted 3-2-2011. Stenseng and Andersen (2011)

FIRST RESULTS OF RECOVERY OF SHORT WAVELENGTH GRAVITY FIELD SIGNALS FROM CRYOSAT-2 DATA

Lars Stenseng[1] **and Ole Baltazar Andersen**[1]

[1]*Geodesy Dept., DTU-Space, National Space Institute, Juliane Maries Vej 30, DK-2100 Copenhagen, Denmark*

ABSTRACT

A number of geophysical phenomena in the open ocean are still unresolved by conventional 1 Hz altimetry, but could be observed through the potential improvements offered by SAR, or Delay-Doppler (DD), altimetry. The DD altimeter offers the following benefits with respect to conventional satellite altimetry: Factor of 20 improvements in along track resolution, along-track footprint length that does not vary with wave height (sea state), and improved precision in sea surface height measurements/sea surface slope measurements.

These improvements are studied with respect to retrieval of short wavelength geophysical signal related to mainly bathymetric features. The combination of upward continuation from the sea bottom and smoothing the altimeter observations resulted in the best recovery of geophysical signal for simulated 5-Hz DD observations. The first validation of these theoretical modelling results with respect to resolution and noise are presented using various CryoSat-2 data and evaluation against conventional Radar altimeter data from older GM missions onboard ERS-1 is presented.

A comparison of L2 products for LRM data are carried out with retracked L1b data for the same data types.

Key words: CryoSat-2, Retracking, Gravity field, Ocean.

1. INTRODUCTION

Three months of CryoSat-2 commissioning phase data has been investigated to asses the performances with respect to recovering geophysical signals. A number of different retrackers are applied on LRM and SAR data and the performance is evaluated and compared with LRM L2 data.

The derived datasets are filtered and geophysical signals are extracted and compared with earlier altimeter derived geophysical signals.

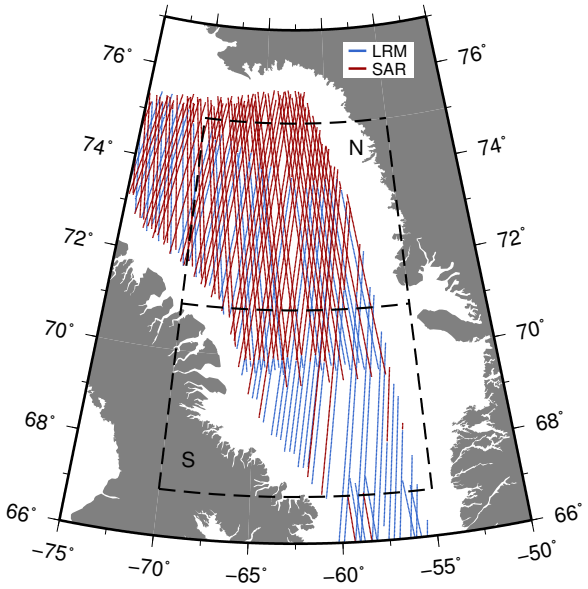

Figure 1. SAR (red) and LRM (blue) data from September to November in the Baffin Bay.

2. AREA AND DATA

Two test areas (S and N) has been chosen in the Baffin Bay (Figure 1) between Greenland and Canada and all available data in the period from September to November 2010 has been investigated. Figure 1 show the available LRM (blue) and SAR (red) data in the three month period.

It is expected that sea-ice can occur in the two test areas in November and thus affect the results negatively.

3. DATA PROCESSING

The provided range and geophysical correction were applied to the 20 Hz Cryosat-2 data. These include correction for the wet and dry tropospheric path delay as well as ionospheric path delay. Similar tide correction (ocean, load, pole and earth) and dynamic atmosphere correction was also applied. No correction for sea state bias were

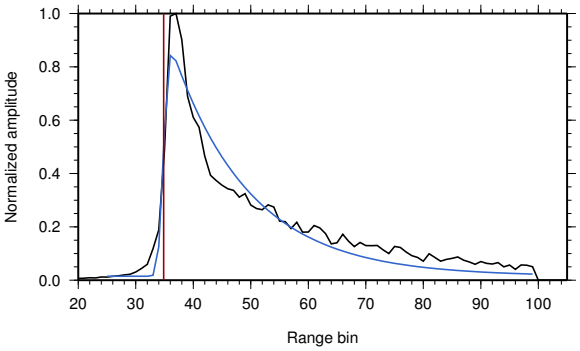

Figure 2. SAR waveform (black) with fitted five parameter Beta retracker with exponential tail (blue) and surface estimate (red).

provided or attempted and no information on the applied corrections could be retrieved from the data provided.

3.1. Retracking

A number of retrackers has been implemented to analyse the CryoSat-2 data. First the Offset Center Of Gravity (OCOG) retracker [1] is applied on all waveforms. This has been done even though the OCOG is expected to give erroneous results for SAR waveforms. Next a threshold retracker [2] is applied, using a 50% threshold for LRM data and a 80% threshold for SAR data, to obtain estimates of the range to the surface. In addition a five parameter Beta retracker with exponential tail [3] is implemented using a Levenberg-Marquardt nonlinear least squares algorithm to fit the model to the waveform. The Beta retracker is initialize with the output from the threshold and OCOG retracker.

Figure 2 shows an example of a SAR waveform and the fitted five parameter Beta model. It is clearly seen that the sharp peak characteristic of SAR waveforms is not captured by the Beta retracker.

Finally of a new retracker based on a simplification [4] of the CryoSat waveform [5] has been implemented. This retracker, including the characteristic SAR peak, is however still work in progress and therefore not included in this work.

The OCOG, threshold and Beta retrackers has been applied on all three months of LRM and SAR data from the Baffin Bay and used for the further analysis.

Figure 3 shows a descending segment of the data acquired on October 5 during a shift from SAR to LRM mode. A distinct offset of around 2 m is seen near the end of the SAR profile (red), this is believed to be caused by an error in the applied tropospheric correction. The bias and tilt with respect to the DTU10 Mean Sea Surface is also clearly seen.

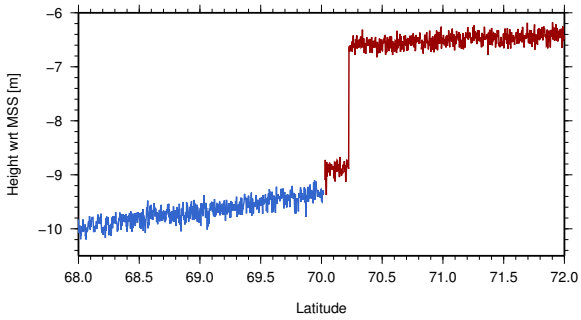

Figure 3. Elevation, obtained with the five parameter Beta retracker, relative to the DTU10MSS from a profile during a shift from SAR (red) to LRM (blue) mode.

3.2. Data editing and retrieval of geophysical signals

An initial screening and outlier detection of the data were performed by comparing the 20 Hz observations with the DTU10 Mean Sea Surface and removing data if they differ by more than 3 times the local standard deviation from this model. To reduce the effects of residual orbit errors and sea surface variability tracks were fitted individually to the EGM2008 geoid model by estimating bias and tilt terms to each track, thus removing all signals with a wavelength longer than the size of the region (typically about $3^\circ - 4^\circ$).

Subsequently, a crossover adjustment of the tracks was carried out, also using bias and tilt terms. The processing and interpolation and gravity field prediction follows the method used by Andersen et al. [6] except from the fact that only ERS-1 geodetic mission data have been used along with Cryosat-2 data for the gravity field determination.

4. RESULTS

As seen in Table 1 the standard deviation of the observations are reduced dramatically. For the Thresshold retracked data and the beta retracked data this reduces the standard deviation from around 1 meter to around 10 cm. For the OCOG retracker the reduction is from around 1 meter to roughly 25 cm.

The importance of upgrading from 1 Hz to 5 Hz sea surface height data for gravity field determination was demonstrated by the ESA SAMOSA project [7]. Subsequently a 5 Hz averaging were performed by analysing sections of 6 data points and removing the two data points that departed the largest with the mean value. Then the remaining four data points were used to compute the 5 hz average. The section were then moved 4 points along the track and the process were repeated. This furthermore reduces the standard deviation of the sea surface height to between 5 to 20 cm dependent on the data types.

The similar values for the 1 Hz ERS-1 geodetic mission

	LRM (area S)				SAR (area N)		
	OCOG	Threshold	Beta	L2	OCOG	Threshold	Beta
Points (Before edditing)	28444	28444	28139	18182	72925	72925	68824
Points (removed gross error)	28060	28127	27941	18180	68664	71653	68176
Std. dev.	1.008 m	0.998 m	1.027 m	0.760 m	1.231 m	1.237 m	1.279 m
Std. dev. (removed tilt and bias)	0.250 m	0.085 m	0.110 m	0.076 m	0.349 m	0.254 m	0.363 m
Points (resampled 5 Hz)	6921	6958	6921	4421	16974	17786	16585
Mean (obs-ref)	0.003 m	0.000 m	0.003 m	0.000 m	0.000 m	0.000 m	0.000 m
Std. dev. (obs-ref)	0.130 m	0.051 m	0.066 m	0.044 m	0.232 m	0.171 m	0.187 m
ERS-1 GM std. dev.	0.09 m				0.141 m		

Table 1. Effect of the data editing and choice of the retrackers in comparison with ERS-1 geodetic mission.

data are around 9 cm, so the 5 Hz (1.1 km along-track) Cryosat-2 data reduces the standard deviation by a factor of two compared with the 1 Hz (6.7 km along-track) older geodetic mission data. This number is very promising for future use of Cryosat-2 data for short wavelength gravity field recovery and represent a significant improvement with the older geodetic mission data.

However, the number should be interpreted with caution. First only a limited number of tracks have been investigated and the majority of the tracks are much shorter than the $3^\circ - 4^\circ$ and therefore only representative of very short wavelength signals. Secondly the sea state bias correction has not been applied and we have not been able to confirm the accuracy of the other range and geophysical corrections applied.

4.1. Comparison with marine gravity data

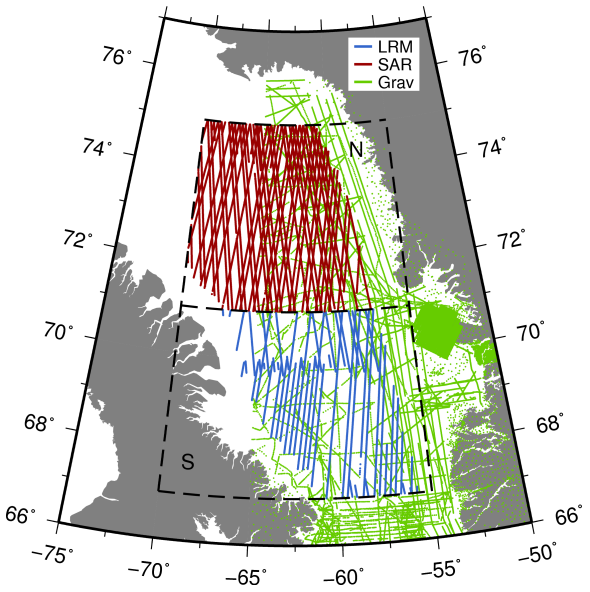

Figure 4. SAR (red), LRM (blue), and marine gravity data (green) in the Baffin Bay.

Table 2 present the comparison with marine gravity field data obtained in the Baffin Bay by several agencies and extracted from the Nordic gravity field database. A total of around 5100 marine gravity field observations were available for interpolation in the northern region and 1900 gravity field observations were available for the southern region. The obtained gravity field determination shown in Table 2 is encouraging. Even though the gravity field determination is generally only improved by 0.2 mGal for LRM and less for SAR this is a promising improvement in light of the fact that this is preliminary results. The reason being firstly that no fine-tuning of the gravity field determination to handle 5 Hz Cryosat-2 were made and the second reason being that only very limited numbers of Cryosat-2 tracks were available for the gravity field determination. A preliminary tuning of the processing toward the higher along-track resolution brings the the standard deviation down to 5.714 mGal for northern area. Thirdly much more finetuning of the processing of the data (i.e., including sea state bias correction) is expected in future versions of the data.

For the northern region a total of 482 ERS-1 Geodetic mission tracks were merged with 74 Cryosat-2 tracks and for the southern region 478 ERS-1 geodetic mission tracks were merged with 41 Cryosat-2 tracks. These CryoSat-2 tracks have a very inhomogenous distribution compared with the eight km equidistant cross track distance of the ERS-1 Geodetic Mission data.

For both the northern section, where SAR data were used, and for the southern section, where LRM data were used, Cryosat-2 data retracked using the tresshold retracker gave slightly favourable result when included in the gravity field determination. For the southern section we were also able to compare with the Level-2 retracked data and find a slight improvement, however L2 data were only available for about 60% of the L1b waveforms.

It might be argued that the comparison with marine grav-

	LRM (area S)	SAR (area N)
ERS-1 GM	6.578 mGal	6.130 mGal
ERS-1 GM + OCOG	7.730 mGal	8.725 mGal
ERS-1 GM + Thres	6.350 mGal	6.106 mGal
ERS-1 GM + Beta	6.535 mGal	6.302 mGal
ERS-1 GM + L2	6.430 mGal	

Table 2. Standard deviation of the difference between marine gravity and gravity estimated from altimetry.

ity field data is not impressive giving standard deviation around 6.5 mGal. This should be compared with many other marine regions with current gravity fields like DTU10GRA which gives numbers around 3 mGal in comparison with marine data. The reason for this is the fact that the gravity field variation in the Baffin Bay is extremely large. The standard deviation of the gravity field anomalies in the Baffin bay is 59 mGal compared with 27 mGal as the global number.

Secondly the marine gravity field observations in this region is generally taken under very rough conditions which directly degrades the accuracy of the observed gravity field observations.

5. CONCLUSION AND OUTLOOK

Three months of CryoSat-2 LRM and SAR data from the Baffin Bay has been investigated using SAR L1b, LRM L1b and LRM L2. The L1b data has been retracked with three different retrackers and compared internally and with an independent dataset. From this first investigation we find very promising results in the comparison with the mean sea surface in both LRM and SAR data. The comparison with the marine gravity field is also promising and preliminary tuning of the processing indicates that significant improvement can be achieved. Furthermore sea-ice debris is expected to be present in the November SAR data and will need to be handled in a future editing scheme to avoid degradation of the derived sea surface and thereby the derived gravity field.

ACKNOWLEDGMENTS

The authors would like to thank the ESA STSE programme for funding the SAMOSA project and the entire CVRT for their huge efforts.

REFERENCES

[1] D. J. Wingham, C. G. Rapley, and H. Griffiths. New techniques in satellite altimeter tracking systems. In *Proceedings of the IGARSS Symposium, Zurich*, pages 1339–1344. IEEE, September 1986.

[2] Curt H. Davis. A robust threshold retracking algorithm for measuring ice-sheet surface elevation change from satellite radar altimeters. *IEEE Transactions on Geoscience and Remote Sensing*, 35(4):974–979, 1997.

[3] Xiaoli Deng and W. E. Featherstone. A coastal retracking system for satellite radar altimeter waveforms: Application to ers-2 around australia. *Journal of Geophysical Research*, 111(C6), 06 2006.

[4] K. A. Giles, S. W. Laxon, D. J. Wingham, D. W. Wallis, W. B. Krabill, C. J. Leuschen, D. McAdoo, S. S. Manizade, and R. K. Raney. Combined airborne laser and radar altimeter measurements over the fram strait in may 2002. *Remote Sensing of Environment*, 111:182–194, 2007.

[5] D. J. Wingham, C. R. Francis, S. Baker, C. Bouzinac, D. Brockley, R. Cullen, P. de Chateau-Thierry, S. W. Laxon, U. Mallow, C. Mavrocordatos, L. Phalippou, G. Ratier, L. Rey, F. Rostan, P. Viau, and D. W. Wallis. CryoSat: A mission to determine the fluctuations in earth's land and marine ice fields. *Advances in Space Research*, 37:841–871, 2006.

[6] Ole Baltazar Andersen, Per Knudsen, and Philippa A. M. Berry. The dnsc08gra global marine gravity field from double retracked satellite altimetry. *Journal of Geodesy*, 84(3):191–199, 2010.

[7] Ole Baltazar Andersen. SAMOSA WP3 technical note. recovery of short wavelength geophysical signals and short spatial scale sea surface height/slope signals. Technical report, DTU-Space, 2008.

A.3 Greenland Ice Sheet Changes from Space using Laser, Radar and Gravity

Proceedings paper to ESA Living Planet, Bergen, Norway, June 27-July 2 2010. Submitted 2-7-2010. Sørensen et al. (2010b)

GREENLAND ICE SHEET CHANGES FROM SPACE USING LASER, RADAR AND GRAVITY

Louise Sandberg Sørensen[1], L. Stenseng[2], S. B. Simonsen[3], R. Forsberg[1], S. K. Poulsen[1], and V. Helm[4]

[1]*Geodynamics Dept., DTU-Space, National Space Institute, Juliane Maries Vej 30, DK-2100 Copenhagen, Denmark*
[2]*Geodesy Dept., DTU-Space, National Space Institute, Juliane Maries Vej 30, DK-2100 Copenhagen, Denmark*
[3]*Centre for Ice and Climate, NBI, Uni. of Copenhagen, Juliane Maries Vej 30, DK-2100 Copenhagen, Denmark*
[4]*Geosciences Division, Alfred Wegener Institute, Columbusstrasse, D-27568 Bremerhaven, Germany*

ABSTRACT

The Greenland cryosphere is undergoing rapid changes, and these are documented by remote sensing from space. In this paper, an inversion scheme is used to derive mass changes from gravity changes observed by GRACE, and to derive the mean annual mass loss for the Greenland Ice Sheet, which is estimated to be 204 Gt/yr for the period 2002-2010.
NASA's laser altimetry satellite ICESat has provided elevation estimates of the ice sheet since January 2003. In order to be able to compare GRACE and ICESat derived results, the ICESat volume change must be converted into a mass change estimate. Therefore, it is necessary to model the densities and compaction of the firn. We find that data from ASIRAS show great potential for validating the glaciological models used to determine the densities and firn compaction.

Key words: Greenland Ice Sheet; GRACE; ICESat; ASIRAS.

1. INTRODUCTION

The space-based techniques for measuring cryospheric changes are very different in nature, and have different advantages and disadvantages. The large present-day changes of the Greenland Ice Sheet are quantified by the different satellite data sets. Gravity changes observed by the GRACE satellites since 2002 can be used to estimate the total mass loss of the ice sheet [1, 2, 3]. The GRACE observations are sensitive to other mass redistribution signals such as post glacial rebound (PGR), which is still poorly constrained in Greenland. In this paper, we use an inversion scheme to estimate the mean annual mass loss of the Greenland Ice Sheet from GRACE data (2002-2009).
NASA's laser altimetry satellite ICESat has, since the launch in January 2003, provided time tagged and geolocated elevation estimates of the ice sheet. The ICESat laser signal is reflected by the snow surface and thus allowing the estimation of the change in volume of the entire ice sheet. Modeling of the snow/ice densities, and processes such as firn compaction, is a necessity in order to convert the volume change of snow and ice observed by ICESat into a mass change estimate, which can be compared with the GRACE results.
We show that the use of high resolution SAR altimeter data from ASIRAS along the EGIG line (see Figure 1) has great potential for validating and constraining the glaciological models, used to convert volume to mass changes.

2. MASS LOSS OF THE GREENLAND ICE SHEET FROM GRACE

We use a Tychonov generalized inversion method with regularization described in [4], to derive monthly mass variations of the Greenland Ice Sheet from changes in gravity, observed by the GRACE satellites.
The GRACE Level-2 data used, consist of monthly spherical harmonic expansions of the Earth's gravity potential. The monthly solutions are represented by a set of Stokes harmonic coefficients up to degree and order 60 [5], provided by the CSR processing center (Center for Space Research, University of Texas, USA) [6]. The C_{20} coefficients in the monthly GRACE solutions are replaced by coefficients derived from 5 satellite laser ranging (SLR) campaigns [7].
The gravity signal caused by PGR is determined from the ice history ICE-5G(VM2) [8], and is subtracted from the gravity trend derived from the GRACE data.
The time series of mass change is shown in Figure 2. By fitting a linear trend through the entire period (2002-2009) gives a mean annual mass loss of 204 Gt/year.

3. ICESAT DERIVED ELEVATION CHANGES ALONG THE EGIG LINE

The elevation changes of the ice sheet near the EGIG line are derived from the ICESat data. The area is outlined

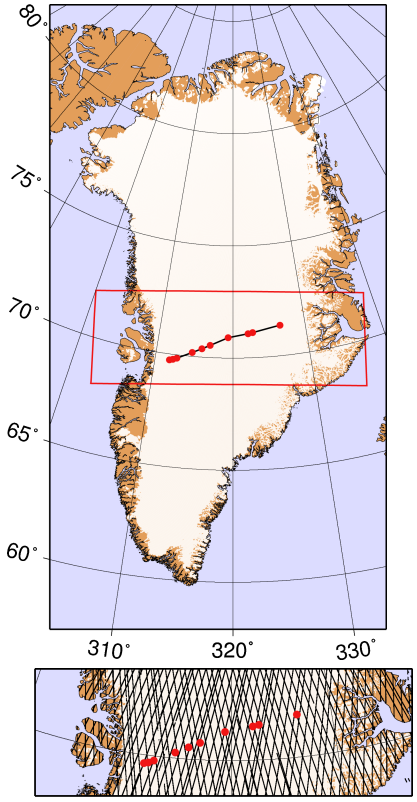

Figure 1. The upper figure shows the EGIG line crossing the Greenland Ice sheet. The lower figure shows the ICESat ground track coverage in the area.

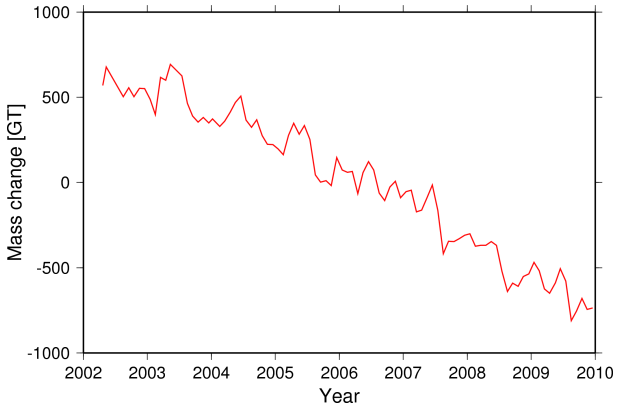

Figure 2. Mass change time series of the Greenland Ice Sheet from the monthly GRACE CSR models.

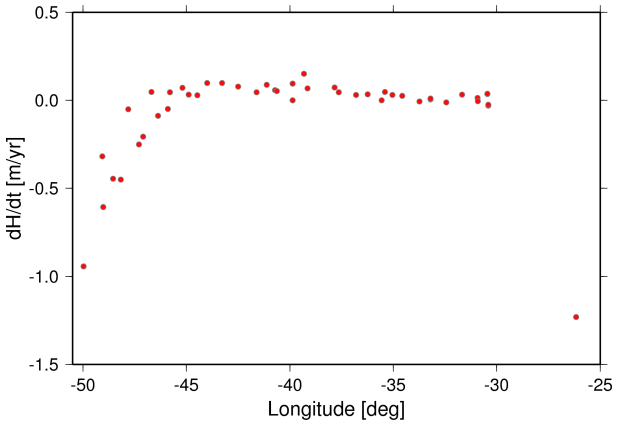

Figure 3. Elevation changes [m/yr] along the EGIG line derived from ICESat data.

in Figure 1. The data used is the GLA12 'Antarctic and Greenland Ice Sheet Altimetry Data' product [9], which was downloaded from National Snow and Ice Data Center. This study is based on the available release 31, 91-day repeat cycle data, spanning the period from October 2003 to March 2008.

Filtering of the data and application of corrections is necessary in order to remove problematic data [10, 11]. The saturation correction is added to the relevant measurements, which are flagged in the data files. We reject problematic data, based on the shape of the return signal, and the number of peaks. Besides these criteria, we have used the data quality flags and warnings given with the data to reject less accurate measurements [12].

Due to problems with the GLAS instrument, ICEsat has measured only 2-3 months (campaigns) every year. The ICESat ground tracks are not exactly repeated, and this makes deriving elevation changes problematic. An observed elevation difference between two (repeat) tracks is a sum of the surface slope, seasonal variations, and a secular trend.

Several method for deriving elevation changes from ICESat data have been published [13, 14, 15]. The elevation changes (dH/dt) presented here, are derived by a method similar to [16, 17] in which the elevation (H) is assumed to be a linear function of time and the surface slope (along-track and cross-track), and a cosine and sine function, describing the seasonal variability. Using this assumption, we estimate dH/dt in 500 m segments along track. The individual ICEsat measurements in each 500 m segment are assigned a weight which ensures that each available ICESat campaign will have equal weight in the dH/dt solution.

Figure 1 shows the ICESat data coverage in the area, and Figure 3 shows the derived elevation changes in a profile crossing the ice sheet, following along the EGIG line. It is seen, that there is a clear thinning of the ice sheet near the ice margins, and that the elevation changes are close to zero in the central parts.

4. DENSITY AND FIRN COMPACTION MODELLING

In order to tie the different observations of the Greenland Ice Sheet together, modelling of snow and firn processes have to be conducted. An observed elevation change of the ice sheet can be related to mass changes by modelling the firn response to climate changes, and the surface density of the ice sheet.
The firn compaction is a function of climate variables such as temperature and accumulation. It is important to determine the elevation changes caused by firn compaction, since it should not contribute to the total mass balance of the ice sheet determined from ICESat data.
Following [18, 19, 20, 21, 22], the annual firn layer thickness (λ) at time after deposition $t = t_0 + t_i$, can be modeled by Eq. 1

$$\lambda(t_0, t) = \begin{cases} \left(\frac{(b(t_0) - r(t_0))\rho_i}{\rho_f(t_0, t)} + r(t_0) \right) \tau & , b(t_0) \geq r(t_0) \\ b(t_0)\delta(t - t_0)\tau & , b(t_0) < 0 \end{cases} \quad (1)$$

where b is the surface mass balance, $r(t_0)$ is the amount of refrozen melt water inside the firn layer, ρ_i is the density of ice, ρ_f is the surface firn density, τ is a time constant and δ is the Kronecker delta. The layer thickness is estimated from year to year, to determine the elevation changes of the Greenland Ice Sheet, caused by changes in the surface temperature and precipitation.
Firn compaction modelling is associated with a number of unknowns, and the error analysis is not tangible from the model input. However, an important part of the modelling is to validate the models with airborne measurements such as the ASIRAS flight campaign and connected firn density studies from in-situ measurements.

5. ASIRAS DATA

The ASIRAS instrument [23] is developed as an airborne interferometric SAR altimeter with properties similar to the SIRAL instrument on CryoSat-2. ASIRAS radar data and lidar data was collected in spring 2006 along the EGIG line and snow densities were measured with N-probe [24] at selected sites. A combination of the delay compensated SAR processing and the low flight altitude (approximate 300 m above terrain), allows the radar signal to penetrate up to 15 m into the snow pack. From the radar return signal it is possible to detect layering in the snow pack [25], caused by the seasonal variations in the snow properties.
A local maximum algorithm is used to detect peaks in the ASIRAS echoes, which is related to the annual variation in the snow density. These annual layers can be detected and followed along the EGIG line in the entire dry snow zone, and in some parts of the percolations zone.
Assuming that the snow can be described as a mixture of air and small ice particles, it is possible to calculate

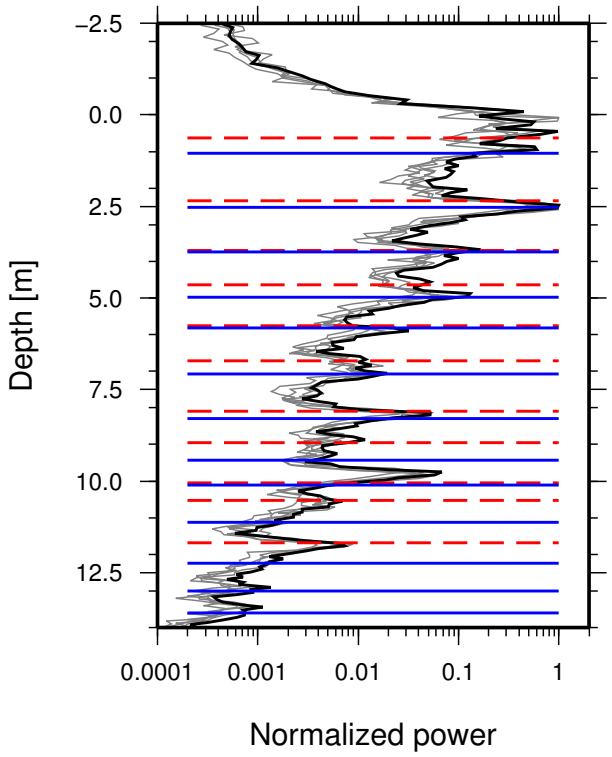

Figure 4. Comparison of different data types at T19. ASIRAS echos (in black and grey), modelled layers (in blue), and high density layers measured by N-Probe (in red).

the permittivity of the snow volume [26], as a function of the density, and hence the refractive index. The apparent depth of a layer can now be converted to true depth using a simple density model for the snow pack. It is now possible to compare the layers derived from the model with the layers detected in ASIRAS data.
An example of typical ASIRAS echoes is shown in Figure 4. The black line shows the echo obtained closest to the T19 site and the grey lines show echoes immediately before and after the closest approach.

6. CONCLUSION AND OUTLOOK

We find a mass loss estimate of the Greenland Ice Sheet of -204 Gt/yr based on GRACE data (2002–2009). In order to compare changes derived from ICESat data with the GRACE results, it is necessary to model firn compaction. Preliminary studies show that the firn compaction is a significant contribution to the total volume change, and therefore it is important to validate the models used.
In order to do so, we use ASIRAS and N-probe data along the EGIG line. We show that in general there are good agreement between ASIRAS data, N-probe data and the snow model west of the Ice Divide, see Figure 4. However, east of the Ice Divide the modelled layers and ASIRAS derived layers deviates, and unfortunately there

is no N-probe data in this area to confirm either.

ACKNOWLEDGMENTS

GRACE data was available via the PO.DAAC system
ASIRAS data has been collected during the CryoVEx (CryoSat Validation Experiment) campaigns by members of CVRT (CryoSat calibration and validation team). We would like to thank all members of the CVRT, especially Elizabeth Morris who collected and processed the N-probe data.
ECMWF ERA-interim data used in this study have been provided by ECMWF and been obtained from the ECMWF Data Server.
ICESat data was downloaded from the NSIDC web site.
We would like to thank S. J. Johnsen for useful discussions of the firn compaction process.

REFERENCES

[1] S. B. Luthcke, H. J. Zwally, W. Abdalati, D. D. Rowlands, R. D. Ray, R. S. Nerem, F. G. Lemoine, J. J. McCarthy, and D. S. Chinn. Recent greenland ice mass loss by drainage system from satellite gravity observations. *Science*, 314(5803):1286–1289, 2006.

[2] B. Wouters, D. Chambers, and E. J. O. Schrama. Grace observes small-scale mass loss in greenland. *Geophys. Res. Lett.*, 35(20):L20501–, October 2008.

[3] I. Velicogna. Increasing rates of ice mass loss from the greenland and antarctic ice sheets revealed by grace. *Geophys. Res. Lett.*, 36(19):L19503–, October 2009.

[4] L. Sandberg Sørensen and R. Forsberg. Greenland ice sheet mass loss from grace data. In *International Symposium on Gravity, Geoid and Earth Observation (GGEO), 2008, Crete, Greece*, 2008.

[5] B. D. Tapley, S. Bettadpur, M. Watkins, and C. Reigber. The gravity recovery and climate experiment: Mission overview and early results. *Geophys. Res. Lett.*, 31, 2004.

[6] S. Bettadpur. *Level-2 Gravity Field Product User Handbook, Rev. 2.3*. Center for Space Research, University of Texas, Austin, 2.3, 2007.

[7] M Cheng and B. D. Tapley. Variations in the earth's oblateness during the past 28 years. *J. Geophys. Res.*, 109:B9, 2004.

[8] W.R. Peltier. Global glacial isostasy and the surface of the ice-age earth: The ice-5g (vm2) model and grace. *Annual Review of Earth and Planetary Sciences*, 32(1):111–149, May 2004.

[9] HJ Zwally, R. Schutz, C. Bentley, J. Bufton, T. Herring, J. Minster, J. Spinhirne, and R. Thomas. GLAS/ICESat L2 Antarctic and Greenland Ice Sheet Altimetry Data V031. *Boulder, CO: National Snow and Ice Data Center left fence http://nsidc. org/data/gla12. html right fence*, 2010.

[10] Benjamin E. Smith, Charles R. Bentley, and Charles F. Raymond. Recent elevation changes on the ice streams and ridges of the ross embayment from icesat crossovers. *Geophys. Res. Lett.*, 32(21):L21S09–, October 2005.

[11] H. A. Fricker, A. Borsa, B. Minster, C. Carabajal, K. Quinn, and B. Bills. Assessment of icesat performance at the salar de uyuni, bolivia. *Geophys. Res. Lett.*, 32(21):L21S06–, September 2005.

[12] NSIDC. Glas altimetry product usage guidance. 2010.

[13] Helen Amanda Fricker and Laurie Padman. Ice shelf grounding zone structure from icesat laser altimetry. *Geophys. Res. Lett.*, 33(15):L15502–, August 2006.

[14] D.C. Slobbe, R.C. Lindenbergh, and P. Ditmar. Estimation of volume change rates of greenland's ice sheet from icesat data using overlapping footprints. *Remote Sensing of Environment*, 112(12):4204–4213, December 2008.

[15] Hamish D. Pritchard, Robert J. Arthern, David G. Vaughan, and Laura A. Edwards. Extensive dynamic thinning on the margins of the greenland and antarctic ice sheets. *Nature*, 461(7266):971–975, October 2009.

[16] Ian M. Howat, Ian Joughin, Mark Fahnestock, Benjamin E. Smith, and Ted A. Scambos. Synchronous retreat and acceleration of southeast greenland outlet glaciers 200006: ice dynamics and coupling to climate. *Journal of Glaciology*, 54:646–660, 2008.

[17] B. E. Smith, H. A. Fricker, I. R. Joughin, and S. Tulaczyk. An inventory of active subglacial lakes in antarctica detected by icesat (20032008). *J. Glaciol.*, 55(192):L21S09–, 2009.

[18] Michael M. Herron and Chester C. Langway. Firn densification: An empirical model. *Journal of Glaciology*, 25(93):373–385, 1980.

[19] H. Jay Zwally and Li Jun. Seasonal and interannual variations of firn densification and ice-sheetsurface elevation at the greenland summit. *Journal of Glaciology*, 48:199–207(9), March 2002.

[20] Jun Li, H. Jay Zwally, Helen Cornejo, and Donghui Yi. Seasonal variation of snow-surface elevation in north greenland as modeled and detected by satellite radar altimetry. *Annals of Glaciology*, 37:233–238, 2003.

[21] Niels Reeh, David A. Fisher, Roy M. Koerner, and Henrik B. Clausen. An empirical firn-densification model comprising ice lenses. *Annals of Glaciology*, 42:101–106, 2005.

[22] Niels Reeh. A nonsteady-state firn-densification model for the percolation zone of a glacier. *J. Geophys. Res.*, 113:–, September 2008.

[23] C. Mavrocordatos, E. Attema, M. Davidson, H. Lentz, and U. Nixdorf. Development of ASIRAS (airborne SAR/Interferometric altimeter system). *IEEE International Geoscience and Remote Sensing Symposium*, 4:2465–2467, 2004.

[24] Elizabeth M. Morris and J. David Cooper. Instruments and methods. density measurements in ice boreholes using neutron scattering. *Journal of Glaciology*, 49(167):599–604, 2003.

[25] R. L. Hawley, E. M. Morris, R. Cullen, U. Nixdorf, A. P. Shepherd, and D. J. Wingham. Asiras airborne radar resolves internal annual layers in the dry-snow zone of greenland. *Geophysical Research Letters*, 33, 2006.

[26] H. Looyenga. Dielectric constants of heterogeneous mixtures. *Physica*, 31:401–406, 1965.

A.4 K_u-Band Radar Penetration into Snow over Arctic Sea-Ice Derived from Airborne Laser and Radar Altimeter Freeboard Retrievals

Paper submitted to Journal of Geophysical Research, Ocean. Submitted 23-2-2011. Hendricks et al. (2011)

K_u-Band radar penetration into snow over Arctic sea ice derived from airborne laser and radar altimeter freeboard retrievals

S. Hendricks,[1] L. Stenseng,[2] V. Helm,[1] S. M. Hvidegaard,[2] C. Haas[3] and S. Hanson[4]

Abstract. Freeboard estimates from airborne laser and radar altimeters are used to quantify the penetration of K_u-Band radar waves into the snow layer of Arctic sea ice. Freeboard profiles were obtained by a CryoSat-2 type radar altimeter, the Airborne SAR/Interferometric Radar Altimeter System (ASIRAS) and elevation data of an across-track scanning laser altimeter. The apparent penetration, defined as the offset between the maxima of the radar and laser freeboard probability distributions, ranges between 0.0 and 0.15 m. In the Arctic these magnitudes are too small to agree with the expected snow thickness ($\geq$ 0.3 m). The real penetration is further reduced if the slower radar wave propagation speed (-18 – -27%) in the snow layer is taken into account. Local in-situ snow observations show a high density snow surface layer as a possible dominant backscatter source in an area of zero penetration. QuikScat backscatter maps are used to infer a relationship between the apparent penetration and surface characteristics, resulting in a correlation factor of -0.69. In addition, the influence of surface roughness within the radar footprint on the point-wise laser-radar differences is investigated using high resolution laser data. The analysis reveals a sensor bias in the low freeboard range when areas of mixed reflectivities are present and an overestimation of the radar freeboard in zones of heavy ice deformation. While findings might be used to improve CryoSat-2 sea ice products, the surface type dependence of airborne datasets must be considered for the direct or statistical comparison with satellite ground tracks.

1. Introduction

The retrieval of freeboard, the elevation of sea ice above the water level, is the only feasible but indirect method for satellite remote sensing of sea ice thickness at basin scales. Sea ice thickness is a fundamental parameter in the polar climate system [*Holland et al.*, 2006], since it contributes to the probability of the ice cover to survive the annual melting season. The observed reduction in sea ice extent in the Arctic [*Stroeve et al.*, 2007] and the observed reduction of the area of old, typically thicker ice [*Nghiem et al.*, 2007] imply a recent change in the overall thickness distribution of the Arctic. Therefore, basin-scale thickness observations are necessary to assess the current state and for predictions of the future evolution of the Arctic sea ice cover.

Freeboard data is obtained by satellite altimeters, which measure their range to the surface below. The result are elevation profiles which contain height data of sea ice floes and of the ice-free ocean surface. As illustrated in Figure 1, the elevations of the ice surface subtracted by the elevations of open water areas yield freeboard. If no elevation of the dynamically changing ocean surface is available, approximations must be used, such as ocean surface height models. Sea ice thickness can be calculated from freeboard using Archimedes principle with the assumption that ice floes are in isostatic balance for each measurement point. The estimation of sea ice thickness by freeboard measurements is the scientific target of several satellite missions. The radar altimeter on the ERS satellites were the first ones used for freeboard retrieval in the Arctic from 1993 to 2001 [*Laxon et al.*, 2003] and in the Antarctic (1995 to 2002) [*Giles et al.*, 2008a]. These measurements were followed by the European Space Agencys (ESA) ENVISat [*Giles et al.*, 2008b] and the NASAs ICESat missions [*Kwok et al.*, 2007; *Farrell et al.*, 2009]. The most recent CryoSat-2 spacecraft [*Wingham et al.*, 2006] features a synthetic aperture K_u-Band radar altimeter (SIRAL), which allows freeboard measurements with an extended maximum latitude of 88° compared to earlier missions (ERS-1, ERS-2, ENVISat: 81.5°, ICESat: 86°).

Since freeboard only represents a small fraction of the total thickness column of floating sea ice, the conversion into ice thickness is very sensitive to errors in the freeboard data. Satellite range measurements can be accurate on a centimeter scale over flat surfaces, however several methodical and instrument specific error sources exist in the freeboard processing. A common problem for all sensors is the inaccurate knowledge of the local sea level elevation in areas with high ice concentration. The dynamic sea surface topography (DSST) is influenced by ocean currents and atmospheric pressure patterns, which are not captured in a geoid model. Typically the DSST is obtained by interpolation of elevations of open water patches along the profile. These areas can be identified by using the reflectivity of the surface [*Kwok et al.*, 2006] or the application of filtering methods to the elevation data [*Forsberg and Skourup*, 2005; *Zwally et al.*, 2008]. Instrument specific errors, especially for radar altimeter systems, are on the one hand potential uncertainties in the penetration of the radar waves into the snow layer. The penetration depends on the wavelength of the radar altimeter and the physical properties of the snow layer, e.g.

[1]Alfred Wegener Institute for Polar and Marine Research, Bremerhaven, Germany.
[2]DTU-Space, Technical University of Denmark, København Ø, Denmark.
[3]Department of Earth and Atmospheric Sciences, University of Alberta, Edmonton, Canada.
[4]Danish Meteorological Institute, København Ø, Denmark.

0148-0227/11/$9.00

density and wetness, which are highly variable by region and time of the year. On the other hand, small scale surface roughness and ice floes of different spatial scales lead to a high freeboard variability within the radar footprint. Different types of surface roughness may influence retracker algorithms, which estimate the first arrival of the radar echo from the sea ice surface.

Here, we present results from three field campaigns in the framework of the ESA initiated CryoSat Validation Experiment (CryoVEx). Freeboard data was collected with an airborne laser and radar altimeter over sea ice in the northern Baltic Sea as well as the Greenland and Lincoln Sea in the western Arctic Ocean. The comparison of laser and radar freeboard data allows the direct estimation of an apparent penetration of the radar waves into the snow layer as laser beams are always reflected at the top snow or ice surface. In this study we define the term penetration as the depth of the dominant scattering horizon below the snow surface. A fraction of the received return echo might originate from below this horizon, however here we only consider the range to the main reflector.

The penetration of K_u-Band radar waves into the snow layer has been the focus of other studies in the Arctic [*Giles et al.*, 2007; *Mäkynen and Hallikainen*, 2009] and the Antarctic [*Leuschen et al.*, 2008; *Willatt et al.*, 2010b]. We verify their findings with large-scale surveys including key regions of Arctic perennial sea ice, for which the first results of coincident laser and radar freeboard are presented here. The entire dataset covers various snow conditions and sea ice types, which are classified by the use of other satellite remote sensing products.

We use two approaches to investigate radar penetration into the snow cover. First, we analyze differences between the radar and laser freeboard probability distributions. The comparison yields a large-scale apparent penetration, which may be used for the conversion of satellite-derived radar freeboard into ice thickness. Field data of snow properties, where available, are used to discuss the findings.

The contributions of different ice surface conditions to this large-scale apparent penetration are investigated in a second step with a point-to-point analysis of both altimeter systems. We focus on the influence of surface roughness on the freeboard retrieval, because ice deformations zones are common and hold a significant part of the sea ice volume in the Arctic Ocean. Besides the classification of surface roughness as variability between neighboring freeboard points, the high resolution of the digital elevation models (DEMs) of the across-track scanning laser altimeter enables the investigation of sub-footprint scale roughness of the radar antenna beam pattern.

2. Data

Airborne radar and laser altimetry data were collected during the CryoVEx field campaigns in spring 2005, 2006 and 2008 [*Helm et al.*, 2006; *Stenseng et al.*, 2007; *Hvidegaard et al.*, 2009]. The activities focussed on sea ice covered areas in the Bay of Bothnia (northern Baltic Sea) in 2005 and the Greenland and Lincoln Sea in both 2006 and 2008. While the Bay of Bothnia is covered by thin first year ice in early spring, much thicker sea ice originating from the Arctic Ocean can be found in the Greenland and Lincoln Sea. The Greenland Sea and Fram Strait are the major outflow region for multi-year ice (MYI) from the Transpolar Drift Stream, while the sea ice cover in the Lincoln Sea is characterized by a band of older and heavily deformed MYI along the coastlines of the Canadian Archipelago.

The location of individual profiles are illustrated in Figure 2. In 2005, altimeter data was collected during two transects between Stockholm and Oulo, Finland over the Bay of Bothnia in the northern Baltic Sea. In 2006 and 2008, the airports of Longyearbyen (Svalbard Archipelago), Station Nord (Greenland) and the Canadian Forces Station Alert on Ellesmere Island were used as bases for operations. Data were acquired along several profiles of 60 - 100 km length on the survey flights between the bases. A summary of all profiles, partitioned into the three main research areas is given in Table 1. The boundary between the Greenland and Lincoln sea is defined here by the 35°W meridian. Though the field campaigns were organized by different institutes in each year using varying aircraft types, the basic instrument configuration remained unchanged. In 2005, a Dornier 228 type airplane operated by the German Aerospace Centre (DLR) on behalf of the Alfred Wegener Institute was used during the Baltic Sea campaign. The field campaigns in the higher Arctic in 2006 and 2008 were executed by the Danish National Space Centre (DNSC, now Technical University of Denmark, DTU) using chartered Twin-Otter aircraft. All aircrafts were equipped with an inertial navigation system (INS) for accurate aircraft attitude information and several differential GPS receivers. The key instruments for freeboard retrieval were a synthetic aperture radar altimeter and a cross-track scanning laser altimeter, which are described in more detail in the following sections. The basic configuration and the data collection principle are illustrated in Figure 3.

2.1. Radar Altimeter

The ASIRAS (Airborne SAR/Interferometric Radar Altimeter System) is designed for radar height measurements with along-track resolution enhancement using the synthetic aperture technique. ASIRAS represents an airborne version of the SIRAL radar system onboard CryoSat-2, with two antennas and a center frequency of 13.5 GHz (K_u-Band). ASIRAS can be operated in a low-altitude (LAM) and high-altitude mode (HAM), allowing varying altitudes from 300 m to more than 1100 m. An interferometric mode using both antennas as receivers for sloped surfaces is also available in HAM but not used over sea ice.

The raw radar data of all campaigns was processed using software provided by ESA [*Cullen*, 2006]. The radar echoes of the individual pulses are sorted into Doppler cells using full beam steering. The resulting echo power waveforms are sampled with a vertical resolution of roughly 10 cm in a 24 m range window. After the SAR resolution enhancement the along-track footprint of the radar height estimates is roughly 3 m, while the across-track footprint depends on altitude with a 2.2 degree opening angle of the antenna beam pattern.

Table 1. Statistics of airborne laser and radar altimetry profiles over sea ice acquired during the CryoVEx field campaigns. For each date the total profile length (l), the number of manual DSST nodes (n_{dsst}) as well as their average spacing ($\overline{d_{dsst}}$) are indicated.

Date	l (km)	n_{dsst}	$\overline{d_{dsst}}$ (km)
CryoVEx 2005			
2005/03/13	127.7	73	2.9
2005/03/14	174.1	116	3.4
CryoVEx 2006			
2006/05/02	264.5	64	4.1
2006/05/11	477.7	61	7.3
2006/05/12	146.0	15	10.3
CryoVEx 2008			
2008/04/27	386.2	80	4.9
2008/05/01	501.0	82	5.8
2008/05/02	408.5	74	5.5
2008/05/05	63.7	13	4.3

2.2. Laser Altimeter

Airborne laser scanners (ALS) from Riegl Laser Measurement Systems were used during the field campaigns to create digital elevation models (DEM) of the sea ice surface. Typically, the across-track scanning altimeter uses a pulse frequency of 30 kHz and an opening angle of roughly 60 degrees, giving a swath width comparable to the flight altitude. The lateral spacing of neighboring data points varies between 1.3 m at 300 m altitude and 2.7 m at 650 m altitude. Given the ASIRAS across-track 3dB beam width of 2.2 degree, the ALS DEM covers the complete radar footprint with typically 20 points within the footprint.

3. Methods and Data Processing

An important issue before merging the individual data streams is the calibration of the timestamps of all sensors, because latencies in the data acquisition architecture can result in significant errors. Therefore, the 1 second time pulse of the GPS is used to synchronize time signals. First, offsets in the INS timestamps relative to the GPS time are removed by cross-correlation of the first derivative of the airplane heading from the INS and the calculated counterpart from both GPS receivers in the front and the rear of the aircraft hull. The timestamp offset of the altimeter sensors can be removed by minimizing undulations in the DEMs over flat surfaces, which are caused by the relatively shifted aircraft attitude information. These calibrations were performed and manually checked for each flight.

3.1. Calibration of the Laser DEM

During installation, the lever-arm between the firing point of the laserscanner and the INS and the phase center of the GPS antennas is measured in an aircraft fixed coordinate system. Using positions obtained from GPS, the attitude determined by the INS, and the lever-arm it is possible to determine the position of the target hit by the laser. Due to the distance between the laserscanner and the target the misalignment between the INS and the laserscanner needs to be determined with high accuracy to obtain a precise position estimate for the target. Positions of buildings near airports have been measured with differential GPS and used as calibration targets for the laser scanner misalignment during the campaigns. The stability of the determined offset angles is monitored and corrected throughout the campaign by overflights of known targets and correlation between crossing flights over rough terrain. Furthermore areas with level and smooth sea-ice can be used to monitor the cross-track misalignment.

3.2. Radar DEM

Contrary to the laser scanner, which directly outputs a range value for each pulse, ASIRAS records the return echo power over a certain time window. From these echo waveforms, the time of arrival of the main surface reflection is obtained by retracker algorithms. In this study we primarly use the Threshold Spline Retracker Algorithm (TSRA) [*Ferraro and Swift*, 1995]. The algorithm uses the one sided half-power width of a cubic spline fitted to the upward sloping curve of the waveform as retrack point. According to *Ferraro and Swift* [1995], the algorithm shows low dependence on noise and scattering mechanism.
The radar range retrieval becomes erroneous at airplane roll angles greater than 1 degree, because of the narrow across-track beam pattern of the ASIRAS antennas. As a result, the assumption of the main reflection in the nadir position is no longer valid yielding apparent undulations in the obtained radar elevation profile. All altimeter data points with roll angles of 1 degree or higher were discarded from further analysis.

3.3. Calibration of laser/radar offset

Internal latencies in the ASIRAS instrument and delays caused by the length of the cables which connect the antennas with the hardware cause an offset between laser and radar DEMs. By comparison of laser and radar derived ranges over surfaces with low or no penetration (e.g. open water, leads and runways) a common range reference can be established for both sensors. A coarse correction is applied in the radar processing to compensate for known delays in cables and internally in the radar. In addition, the use of different retracker algorithms will result in varying range estimates even over targets with no penetration. Therefore the range offset calibration was repeated for any retracker algorithms used here. For this study, the laser/radar offset was verified at any ice-free profile subsections, under the assumption that the water surface is the dominant reflection horizon for both altimeters and the retrieved range must be identical accordingly.

3.4. Estimation of Freeboard

The sea-ice freeboard (h_f) is then determined by using the height of the sensor determined from GPS (H_{gps}), the range to the reflecting surface corrected for off-nadir pointing (r) and the height of the sea surface (h_{ssf}).

$$h_f = (H_{gps} - r) - h_{ssf} \tag{1}$$

Where the sea surface height is a combination of; the geoid height (h_{geoid}), the dynamic topography of the sea associated with ocean currents (h_{dt}), tides (h_{tides}) and inverse barometric effects (h_{atm}).

$$h_{ssh} = h_{geoid} + h_{dt} + h_{tides} + h_{atm} \tag{2}$$

To get an accurate estimate of the sea surface height models of high temporal and spatial resolution are required. Existing models, unfortunately, do not have sufficiently high resolution. Instead the sea surface height can be estimated directly from the radar or the laser DEMs. In radar data, open water or newly formed ice will show up as specular reflections with a powerful and narrow peak [*Drinkwater*, 1991]. Laser data can be filtered using a lowest level algorithm to obtain an estimate for the sea surface height, assuming that open water does exist in all subsection of each profile. Inserting the determined sea surface height into equation 1 will result in an estimate of the freeboard height of the reflecting surface.

Here, we based the estimation of DSST with the elevation profiles on a manual approach for lead detection. The manual classification uses both laser and radar elevation profiles with the advantage of consistent DSST correction for both datasets with the simultaneous verification of the radar/laser range offset. In the laser DEM open water differs from thin ice by drop-outs of laser returns at the sides of the swath, where the specular reflection causes only very low backscatter towards the incident angle of the laser beam (see Figure 4a). Thin ice however, possesses a rougher surface which returns adequate laser backscatter at higher angles for detection by the laser altimeter. The identified height values of the SST nodes along the profiles are connected by spline interpolation and subtracted from the elevation profiles, yielding laser and radar freeboard.
While this manual detection approach may be suitable for a limited dataset, automated methods will be used for satellite

data like the algorithms for lowest level detection in the elevation profiles [*Forsberg and Skourup*, 2005]. We tested the effectiveness of such algorithms with a 480 km long profile of the 2008 field campaign in the Greenland Sea. The automatic open water detection algorithm uses a combination of waveform classification and lowest level to detect returns from open water. Open water and thin newly frozen ice in leads will act as a highly specular reflector and the returned echo will have a narrow and powerful peak. The distributions of waveform width and power are analyzed and a set of criteria for lead detection is selected. A number of open water candidates are then picked from the profile based on these criteria. To eliminate false returns, from e.g. melt ponds on top of the ice floes, the open water candidates are tested using a lowest level algorithm.
The deviation between the automatic and manual DSST profile is displayed in Figure 4b. For 95 percent of the data the deviation between the manual and automatic classification is less then 0.07 m, while for half of the profile the difference is less than 0.02 m. The latter value shows that the automatic algorithm can perform within the accuracy of the DEMs, however outliers of a significant magnitude are possible, which most likely originate from the ambiguity of elevation characteristics of smooth young level ice and open water patches in the profile. Therefore we chose the manual approach for this study, since we assume that a higher precision can be achieved by visually evaluating the laser DEMs.

3.4.1. Comparability of laser and radar freeboard

The point-to-point comparison of the laser and radar freeboard is complicated by the different footprints of the two altimeter systems. Therefore, the locations of the radar Doppler cells were estimated in the laser DEM, and the laser points within a single ASIRAS footprint were weighted by the radar antenna beam pattern and averaged. The result is a comparable laser freeboard data point for each radar freeboard data point. The number of laser points within the each radar doppler cell depends on the altitude and the application mode of ASIRAS and roughly varies between 10 and 30 points. The standard deviation of these points was calculated together with the weighted laser elevation as a measure of surface roughness within the radar footprint. Typical profiles for each region are illustrated in Figure 5.

4. Results

The sea ice in the Baltic sea consists of seasonal ice, which is comparably thin with respect to the first year/multi year ice in the Arctic Ocean. Although sea ice in the Bay of Bothnia can be heavily deformed due to the surrounding coastlines, wide stretches of thin and undeformed sea ice were sampled by our flights. These were almost completely level and had little or no snow cover. Therefore, they are an ideal target for the determination of the achievable accuracy of airborne freeboard retrievals. In contrast, the Arctic surveys were performed mostly over rough MYI with only sporadic patches of FYI. However, different spatial patterns can be seen over different regions in QuikScat backscatter maps (see Figure 2). For spring conditions, older MYI has a higher backscatter signature than e.g. second-year ice (SYI). In 2006 the older MYI zone extended farther into the central Arctic Ocean, while areal losses of MYI between both years lead to a much smaller MYI zone northwest of Greenland in 2008. However, as a general pattern in both years, the Greenland Sea shows lower QuikScat backscatter values, indicating less deformed sea ice.

4.1. Physical Snow Properties

Logistical constraints did not allow the in-situ characterization of the snow layer in the entire study region. In 2005, the CryoVEx ground activities were based on a ice station of the Finnish research vessel Aranda in the northern Bay of Bothnia. However, the surrounding sea ice was almost snow free and no thickness data was available from the snow covered sea ice in the central Bay of Bothnia. In 2006 and 2008, snow thickness, temperature, salinity, density, texture and stratigraphy were measured on sea ice in the Lincoln sea close to the coast of Ellesmere Island [*Haas et al.*, 2006a; *Hvidegaard et al.*, 2009]. In both years several internal snow layers were found on the multi-year ice with very dense and hard windblown layer at depths of 0.10 to 0.20 m below the surface. In 2006, this dense layer could not be penetrated by snow stakes in some parts of the snow thickness profile, hence the resulting mean snow thickness of 0.28 $\pm$ 0.19 m represents only the soft snow above the hard wind slab layer. More representative measurements of the snow thickness were done near drill holes with a average snow thickness of 0.46 m. In 2008, the mean snow thickness was 0.58 $\pm$ 0.32 m. The temperature in 2006 was typically -4°C at the surface and -8° to -12° at the snow/ice interface compared to colder conditions in 2008 (-8° to -16°). Snow densities ranged from 100 kg/m^3 for loose snow to almost 500 kg/m^3 in the hard windslab layer. The top snow surface featured a thin and dense radiation crust in both years, whose densities could not be sampled.

4.2. Freeboard Probability Distribution

Radar and laser freeboard probability distributions calculated in 0.05 m bins for each year and region are displayed in Figure 6. Except for very small values in the Baltic Sea (< 0.4 m) all other distributions are mainly characterized by two maxima or modes. The first mode lies at 0.0 m and consequently represents the amount of thin ice and open water patches present along each profile. Besides zero freeboard, negative values exist in all distributions. The amount of the negative freeboard represents the accuracy of the DEMs, the limitation of the DSST correction but also the existence of surface waves in larger leads, where the DSST elevation was manually set to a mean value. Another observable feature of the open water mode it the difference in the magnitude between the laser and radar freeboard, especially significant in the 2006 data. In general, all radar freeboard measurements show larger amounts of open water and thin ice (freeboard < 0.3 m).
The Arctic profiles show a second mode between 0.25 m and 0.5 m. In most of the regions the second mode is more pronounced than the open water mode, while the underlying distribution is broader and asymmetric with an elongated tail towards higher freeboard values. This mode represents the most frequent sea ice class, which we assume to be mainly composed of level sections of sea ice floes. Larger freeboard values characterize thicker deformed ice and therefore areas with a high roughness. In general the level ice mode in the Greenland Sea is smaller (0.25-0.5m) than in the Lincoln Sea (0.4-0.55 m). In addition, the amount of very high freeboards (> 1.5 m) is larger in the Lincoln Sea in both years, which shows the thick and rough nature of sea ice in this region [*Haas et al.*, 2006b]. The modes of all distributions are given in Table 2.
A snow layer with a thickness of 0.3 - 0.5 m [*Warren et al.*, 1999] typically covers the sea ice in the Arctic study region. In the Baltic Sea the snow cover is significantly less and in fact the sea ice was partially snow free in 2005. A first estimate of the penetration of the radar waves into the snow layer can be obtained by comparing the modes of laser and radar freeboard. We assume that the modes represents the level undeformed ice and neglect the influence of surface roughness at this point. However, since we cannot guarantee that the profile subset contributing to the modal position is identical for both sensors, the difference of laser and radar

freeboard mode is termed "apparent penetration" here. In the Baltic Sea the sea ice is too thin to resolve a modal difference with a bin size of 5 cm. In the Greenland Sea the modes of laser freeboard are clearly at larger values than the radar freeboard. Here, the apparent penetration amounts to 0.15 m in 2006 and 0.10 m in 2008 respectively. In the Lincoln Sea however, the modal difference is less than 5 cm and therefore not significant compared to the expected snow thickness, resulting in identical modal values in both years. The calculation of radar freeboard is based on the vacuum light speed for the conversion of the travel time into range. To calculate the ray path length through the snow, it is necessary to take the actual radar propagation speed within the snow layer into account. As a result, the actual penetration in the Greenland Sea is given by the apparent penetration reduced by a factor of 22% (37%) [*Mätzler and Wegmüller*, 1987] for a snow density of 300 kg/m^3 (500 kg/m^3). This correction yields a typical penetration of 0.13 m (0.11 m) in 2006 and 0.08 m (0.07 m) m in 2008 over level sea ice. Due to the zero modal offset in the Lincoln Sea, the snow layer correction has no effect here.

4.3. Point-to-Point Differences

The approach of using the modal positions as indicator for the typical penetration is useful for large scale data, however the processes leading to the observed apparent penetration can only be investigated with a point-to-point comparison of laser and radar data. Probability distribution functions of the point-to-point laser and radar freeboard differences are displayed in Figure 7. The PDFs reflect all surface conditions and hence show a broad spectrum of freeboard differences varying from negative values (smaller laser than radar freeboard) to positive values with a well defined mode in all years and regions. Negative differences have to be expected from the erratic and partially random backscatter of blocky ice deformation structures. Except in the Greenland Sea in 2006, the modes of the point-to-point differences are close to or at 0 m. However, most of the distribution are positively skewed, indicating that there is increased tendency for higher laser freeboard for all laser-radar data pairs. The Baltic Sea data from 2005 is most asymmetric, while the distributions in the 2008 Lincoln Sea appears almost symmetrical around a pronounced mode at 0 m. This shape suggests mostly zero penetration with a normally distributed variation of the laser and radar freeboard for rough, deformed surfaces.

The point-to-point difference statistics reveal that laser and radar freeboard are very similar for most of the profile data. However, in the Arctic ocean the profiles consist of level ice as well as zones with a variable degree of deformation. To allow a classification of the point-to-point differences for different surface types, we use the laser freeboard as a reference parameter. This choice is based on the assumption that deformed and level ice show distinct freeboard values. In addition, no penetration into the snow layer has to be considered in the laser range data.

Laser minus radar differences are displayed versus laser freeboard in Figure 8. The plots show the point densities of all measurements. The point density graphs combine the features of the freeboard histograms (Figure 6) and freeboard difference variation (Figure 7). The laser-derived modal freeboard appears in clusters of elevated point density, while the scatter of point-to-point difference is partitioned into the different ice classes. The figure shows that in general, the variability of the difference values is not limited to a certain laser freeboard range. The differences themselves are limited at lower values by the laser freeboard, since the radar freeboard does not show significant amounts of negative values. Especially in all 2006 profiles, a considerable amount of data points are aligned along the identity line of laser and radar freeboard. These data points correspond to the higher occurrence of zero radar freeboard in the histograms of Figure 6. Apparently under certain surface conditions, the radar freeboard tends to reveal open water, where the laser shows values up to the the typical freeboard of level ice (0.5 m). Besides this effect, the scatter of the freeboard difference reaches a maximum and decreases with increasing laser freeboard where less data points exist. Therefore it can be said, that the partially random differences between laser and radar freeboard are not limited to a certain freeboard range.

The positions of the local maxima in the point density give information about the typical penetration behavior in the corresponding freeboard range. In the Baltic Sea no second mode can be found, most of the data points are close to zero freeboard. The Greenland Sea data of 2006 shows in Figure 8 the most positive differences. However, the maximum in the point density is given at point-to-point difference of less than 0.1 m and hence on a smaller value than the apparent penetration of this region, which is defined as the offset in modal laser and radar freeboard (see Figure 6). In all other regions and years the density maximum in the level ice area is close to zero or even slightly negative, as seen in the 2008 Lincoln Sea data. Here, two maxima at non-zero laser freeboard exist. The first maximum, at a laser freeboard of roughly 0.1 m, represents thin FYI, which had formed in a polynya north of Nares Strait between Greenland and Ellesmere Island. Due to the inaccessibility for in-situ observations of this ice, no comparable field observations of snow thickness are available. The second maximum with the majority of data points shows a negative difference, indicating a overestimation of the radar freeboard of deformed ice zones. The overestimation is more pronounced close to the coast where the sea ice surface shows a higher roughness than further off-shore. No such behavior can be found in the 2006 Lincoln Sea and 2008 Greenland Sea data, where the maximum is located at a difference of 0 m.

One characteristic feature, which can be found in the 2008 (especially Greenland Sea) data in Figure 8 is an elevated density of negative differences at zero laser freeboard. This offset does not correspond to a mis-calibration of the laser-radar range offset over open water, but to a problem with the retracker algorithm at lead edges. Here the echo power waveforms show a complex shape, resulting in a tracked elevation below the adjacent open water elevation. In the 2008 data due to a very high ice concentration of the sea ice around Greenland, very few and mostly narrow leads with widths close to the radar footprint were observed. Hence, the radar freeboard is biased due to the retracker problem with many leads, which accumulates at the observed negative radar freeboard for the zero laser freeboard. However, in all profiles enough larger leads were available for the accurate determination of the laser-radar range offset.

4.4. Influence of Surface Roughness

Sea ice has a surface which is rough on many scales. While smaller-scale roughness is governed by the metamorphosis of snow and ice crystals, the larger scale roughness is caused by ice deformation processes. Here we have to consider both scales, since the small scale roughness influences the backscatter and hence the penetration of radar waves into the snow. On the other hand the large scale roughness itself may have a significant impact on the radar range retrieval. We use K_u-band backscatter maps from the SeaWinds sensor on the QuikScat satellite as an indicator for surface roughness on the scale of the radar wavelength. QuikScat data are available on a daily basis for the entire CryoVEx research area (see Figure 2). Because of the coarse resolution (12.5 km) of the backscatter maps, sea ice in only a few QuikScat pixels were surveyed. Data close to the coast were

Table 2. Statistical parameter of laser and radar freeboard distributions (mode and mean) and point-to-point differences (mode, mean and asymmetry factor defined by quotient of mean $\overline{d}$ and standard deviation d^{σ}) in the CryoVEx study regions.

Region	Year	Freeboard				PtP Difference		
		Laser		Radar				
		mode	mean	mode	mean	mode	mean	$\overline{d}/d^{\sigma}$
		m	m	m	m	m	m	
Baltic Sea	2005	0.00	0.08	0.00	0.03	0.00	0.05	0.81
Greenland Sea	2006	0.50	0.64	0.35	0.49	0.06	0.16	0.79
	2008	0.35	0.47	0.25	0.41	-0.02	0.07	0.41
Lincoln Sea	2006	0.55	0.80	0.55	0.71	0.00	0.12	0.45
	2008	0.40	0.68	0.40	0.67	0.00	0.03	0.17

excluded from the comparison because they are affected by land-leakage effects. We did not include the measurements from 2005 in the analysis, since the snow cover in the Baltic Sea cannot easily be compared to that in the Arctic Ocean. Figure 9 shows the relationship between the apparent penetration and QuikScat backscatter for all profiles in the Arctic. The apparent penetration for each profile was calculated with a 5 cm resolution and varies between 0.25 and -0.1 m. A linear regression showed a correlation of -0.69. Within the 95% confidence bounds the apparent penetration quantitatively decreases with increasing backscatter. While this behavior is principally expected from the regional differences of apparent penetration and backscatter maps in the different regions (figure 2), the linear fit reasonably describes the apparent penetration variations over the entire backscatter range. No significant differences between the two years were observed.

Alternatively to the low spatial resolution of the remote sensing dataset, we analyse the effect of larger-scale deformation-based roughness by means of the standard deviation of the laser DEM in the radar footprint. This allows for a comparison for each freeboard data point. However, since the standard deviation of the laser DEM is only a measure of the freeboard variability in the radar footprint and does not reveal the type of variability (e.g. broken small floes in a lead or ridged ice), we analyse roughness in dependence of the absolute freeboard value as well. Figure 10 shows all data points partitioned into bins of laser DEM standard deviation and laser freeboard. Here, the Baltic sea data is included, because its large-scale ice deformation features and ridges are similar to those in the Arctic. Figure 10a shows the amount of data in each bin, while Figure 10b shows the fractions of the data contributed by each region to each bin. The majority of points falls in a freeboard range up to 0.7 m and a roughness range of < 0.1 m. This area is mostly populated by data points from the Lincoln Sea, which also provides the majority of the entire dataset. Based on their ratio of point numbers, data from the Greenland and Lincoln Sea evenly populate the bins only in the lower freeboard range (< 0.4 m), while the Lincoln Sea data is overproportional represented for higher freeboard and roughness values. Data from the Baltic Sea contributes only to very low freeboard values of less then 0.1 m.

The apparent penetration calculated for each bin (Figure 10c) shows a divided structure. An area with positive values (dark-red colors) is diagonally separated from an area with negative apparent penetration (blue colors). While the positive values cluster at higher roughness and relatively lower freeboard values, the negative values are centered at smaller roughness for intermediate freeboard values and extend towards higher roughness for the highest freeboard. This shows that in general, the apparent penetration is highest at the lower freeboard range with a higher roughness, while presumably geometric effects (negative apparent penetration) dominate at the highest laser freeboard range.

The mean difference between laser and radar freeboard in each bin (10d) however does not show this behavior. Instead, the mean difference is persistently positive and increases with higher roughness and freeboard. The only exception is an area of the lowest roughness at a laser freeboard around 0.5 m. Here, the mean point-to-point difference and the apparent penetration show elevated values in a similar pattern. The low roughness values near the typical Arctic modal laser freeboard indicate that these data represent undeformed, snow covered level ice. Here the mean point-to-point differences and the apparent penetration show consistent values of 0.1 m. In all other cases both quantities behave different for individual roughness and freeboard combinations. This indicates that different surface types differently affect radar range retrieval over sea ice.

5. Discussion

The aim of this study is to investigate the penetration of K_u-Band radar waves into the snow cover of Arctic sea ice. To estimate apparent penetration first, we use statistical differences of radar and laser freeboard distributions. The latter serves as a reference measurement of the snow surface, since this is the reflection horizon at typical laser wavelength (near-infrared). We did not correct the radar freeboard for the slower propagation speed of electromagnetic waves in the snow layer, which would decrease the amount of apparent penetration. This approach was chosen, because the apparent penetration might not only be due to the actual travel time of the radar waves within the snow but may also be influenced by surface roughness within the radar footprint. As a matter of fact, the results showed that the freeboard result of both sensors differ significantly for certain sea ice conditions.

Data from thin ice without a significant snow cover in the Baltic Sea gives little evidence in this matter, since it was not covered with a thick snow layer. However, the flat ice surfaces and very low freeboard values in the Baltic create an ideal testbed for an accuracy determination of the sensors. Within the bin size (2 cm) of the freeboard-difference probability distributions only a few negative values were observed, while the majority of data points were located at 0 m or larger differences. This shows that the sensor setup is sufficiently accurate, and that small differences between laser and radar freeboard observed in the Arctic must be due to different penetration behavior and not due to a sensor bias.

5.1. Radar wave penetration

This work follows earlier studies which investigated K_u-Band radar wave penetration into the snow layer on Arctic sea ice with varying approaches. *Giles et al.* [2008a] used a similar airborne radar and laser altimeter combination in the Greenland Sea area, while *Giles and Hvidegaard* [2006] compared airborne laser with satellite radar (ERS-2) freeboard measurements. *Willatt et al.* [2010a] studied penetration in areas of well-known surface conditions by means of the response of corner reflectors.

The findings of our study show different results than these earlier investigations. While *Giles et al.* [2007] concluded that K_u-Band radars yield the range to the snow/ice interface, here we did neither find that the statistical apparent penetration nor the point-to-point difference of radar and

laser freeboard did indicate that the signal penetrates to the ice surface. The differences between laser and radar altimeter in the Greenland Sea were too small (< 0.15 m) for an expected snow thickness of 0.3 - 0.4 m in this region in May [*Warren et al.*, 1999]. More recent studies using corner reflectors [*Willatt et al.*, 2010a] and a ground-based K_u-Band radar [*Willatt et al.*, 2010b] however, confirm the findings of this study that the main radar reflection does not necessarily originate from the snow ice interface.

Two factors might explain the contradicting observed penetration between the two previous studies and our results: 1) Application of different retracker algorithm resulting in an incomparable interpretation of the radar echoes and 2) Differences in the physical properties of the snow layer between May 2002 and 2006/2008.

To test the impact of different retracker algorithms on the radar freeboard, two other retrackers have been applied to a test profile in the Greenland Sea in 2008. Besides the TSRA used for the entire dataset, radar freeboard was obtained by the Offset Center of Gravity (OCOG) [*Wingham et al.*, 1986] and a custom Threshold retracker (THRS). The custom threshold retracker first estimates the amplitude through an average of the three most powerful samples. Secondly the threshold point is estimated using a spline interpolateion of the leading edge. The test profile contains a significant amount of open water patches, which serve as a reference reflection horizon, hence it is very suitable for the range calibration of the different algorithms. The modal radar freeboards derived by the different retracker algorithms (Figure 11) show, that the TSRA yields the lowest value over this test profile. Hence, if for example the OCOG algorithms was used during this study, the apparent penetration would have been smaller in the order of a few centimeter. Though this test might not directly reflect the setups of the *Giles et al.* [2008a] and our campaigns, however its seems unlikely that the different findings can be explained by the choice of retracker algorithm alone.

In-situ information about the physical properties of the snow layer were only available from one dedicated site for each campaign. The site for obtaining ground truth information during CryoVEx 2005 in the Baltic Sea was located on almost snow-free fast ice and consequently field work was focused on local, high-resolution ice thickness data. For CryoVEx 2006 and 2008 snow properties were measured on accessible ice floes in the Lincoln Sea close to the coast of Ellesmere Island. This region was characterized by consistently zero radar penetration in two field campaigns. In regions of partial penetration no ground truth data is available. Hence, the influence of the physical snow properties on the limitation of K_u-Band radar wave penetration is still subject to speculation. Results from a radiative transfer model [*Tonboe et al.*, 2005, 2006] show, that a high density crust at the snow surface can dominate the total backscatter of the snow layer for K_u-Band frequencies. Therefore the radiation crust, which was observed in the Lincoln sea in both years may be a plausible explanation for the zero penetration behavior in the same area. On the other hand, NCEP reanalysis data [*Kalnay et al.*, 1996] reveals that the maximum air temperature was close to 0°C in May 2006, which might have resulted in an increased wetness of the snow layer. Even small amounts of liquid contents within the snow are able to cause a notable increase in radar wave absorption, while surface rather than volume backscatter processes become more important than in dry snow [*Onstott*, 1992]. Colder air and snow temperatures during surveys earlier in the year of 2008 however did not result in a larger apparent penetration than in 2006. The magnitude of the apparent penetration in the Greenland Sea in 2008 (0.15 m) is even smaller than in 2006 (0.10 m). The correlation of the apparent penetration with QuikScat maps points towards a backscatter process as a cause for the limited penetration, however whether snow density or wetness is the crucial factor cannot be answered here. This question can be answered with validation measurements in an earlier period when the snow is much colder, however airborne surveys in the central Arctic then would be logistically more demanding.

5.2. Significance for satellite data

The ASIRAS and the across track scanning laser-altimeter possess a spatial resolution of a few meters, enabling the analysis of radar returns of individual ice surface types. When mixing of different surfaces takes place within the radar footprint, the dominating surface type may differ for both laser and radar altimeter. This was observed with the case of small open water patches and thus a bias is introduced in the mean freeboard. Modal freeboard values instead are far less influenced by sensor biases. Within the CryoSat-2 footprint of roughly 250 × 1000 m the case of a uniform surface type will be rare in the perennial sea ice zone. While the airborne and satellite radar altimeters are affected by the interaction between the radar waves and the snow layer in the same way, the scale of the ice deformation based roughness with respect to the footprint size is significantly different for both systems. The larger satellite footprint leads to less importance of the large-scale roughness in deformation zones and by implication to a higher importance of scattering processes in the snow layer. In conclusion, while surface roughness has to be carefully taken into account when estimating radar penetration in high deformation zones, the direct effect of surface geometry within the radar footprint observed here cannot be directly applied on a satellite radar.

6. Conclusion

In this study, we have presented results from three aircraft campaigns performed to investigate K_u-Band radar penetration into the snow layer over first- and multi-year sea ice by means of coincident laser and radar freeboard estimation. While data acquisition over thin and undeformed first year sea ice in the northern Baltic Sea demonstrated the accuracy of the sensor setup, results over thicker perennial sea ice in the Arctic revealed that the radar range measurements did not yield the distance to the snow/ice interface under late spring conditions, although this is the underlying assumption for sea ice freeboard retrievals from satellites. The regional coverage of data is larger than that of previous studies and allows the observation of the regional variability of apparent penetration. The high spatial resolution of the data enables the discrimination of the influence of scattering processes in the snow and geometric effects due to high surface roughness on the radar range retrieval. We find that different surface roughness characteristics have a significant and varying impact on both airborne laser and radar altimeters.

The physical property leading to the limited penetration in the snow, e.g. density or wetness, could not be identified. The regional variability of the apparent penetration was observed on too large scales to be easily addressed by ground validation campaigns. On the one hand this illustrates the importance of aircraft surveys as an intermediate level for satellite data validation, on the other hand more work is needed to understand and finally quantify this process. In fact, the findings of only partial penetration of the K_u-band radar into the snow under late spring conditions are of high relevance for the accuracy of the CryoSat-2 sea ice product. Knowledge of the ice volume during the maximum of the annual cycle is important for sea ice mass balance monitoring in the Arctic. Since the estimation of ice thickness is crucially dependent on accurate freeboard retrievals, we suggest

that besides the partial penetration, also the regional variability found in this study should be incorporated into the freeboard retrieval algorithms of satellite missions. Additional remote sensing information, e.g. K_u-band backscatter maps from QuikScat follow-on missions are a well-suited to characterize this regional variability and their considerations in the thickness retrieval will lead to a better understanding of the Arctic sea ice thickness distribution observed by satellites.

Acknowledgments. This study was funded by the German Aerospace Center (DLR) and the German Federal Ministry of Economics and Technology (Grant: 50EE0505). Financial support for field campaigns was granted by the European Space Agency (ESA). The outstanding performance of the pilots and support staff of DLR, Air Greenland and Ken Borek was the basis for the success of the airborne surveys. We thank the crew of the Finnish Research Vessel Aranda, Canadian Forces Station Alert, Station Nord and Thule Air Force Base for their support and hospitality. Planning and support of the airborne data acquisition by Rene Forsberg is greatly acknowledged. Robert Cullen (ESA) is thanked for ASIRAS processing support. QuikScat data products have been obtained from CERSAT.

References

Cullen, R. (2006), ASIRAS - Product description, *Tech. rep.*, European Space Research and Technology Centre.

Drinkwater, M. R. (1991), K_u band airborne radar altimeter observations of marginal sea ice during the 1984 Marginal Ice Zone Experiment, *J. Geophys. Res.*, *96*(C3), 4555–4572.

Farrell, S. L., S. W. Laxon, D. C. McAdoo, D. Yi, and H. J. Zwally (2009), Five years of Arctic sea ice freeboard measurements from the Ice, Cloud and land Elevation Satellite, *Journal of Geophysical Research (Oceans)*, *114*, 4008–+, doi: 10.1029/2008JC005074.

Ferraro, E. J., and C. T. Swift (1995), Comparison of retracking algorithms using airborne radar and laser altimeter measurements of the Greenland ice sheet, *IEEE Transactions on Geoscience and Remote Sensing*, *33*, 700–707.

Forsberg, R., and H. Skourup (2005), Arctic Ocean gravity, geoid and sea-ice freeboard heights from ICESat and GRACE, *Geophys. Res. Lett.*, *32*, L21,502.

Giles, K., S. Laxon, D. Wingham, D. Wallis, W. Krabill, C. Leuschen, D. McAdoo, S. Manizade, and R. Raney (2007), Combined airborne laser and radar altimeter measurements over the Fram Strait in May 2002, *Remote Sensing of Enviroment*, *111*, 182–194.

Giles, K., S. Laxon, and A. Worby (2008a), Antarctic sea ice elevation from satellite radar altimetry, *Geophys. Res. Lett.*, *35*, L03,503.

Giles, K. A., and S. M. Hvidegaard (2006), Comparison of space borne radar altimetry and airborne laser altimetry over sea ice in the Fram Strait, *International Journal of Remote Sensing*, *27*, 3105–3113, doi:10.1080/01431160600563273.

Giles, K. A., S. W. Laxon, and A. L. Ridout (2008b), Circumpolar thinning of Arctic sea ice following the 2007 record ice extent minimum, *Geophys. Res. Lett.*, *35*, L22,502.

Haas, C., J. Haapala, S. Hanson, L. Rabenstein, E. Rinne, and J. Wilkinson (2006a), CryoVEx 2006: Field Report, *Tech. rep.*, Alfred Wegener Institut für Polar und Meeresforschung.

Haas, C., S. Hendricks, and M. Doble (2006b), Comparison of sea-ice thickness distribution in the Lincoln Sea and adjacent Arctic Ocean in 2004 and 2005, *Annals of Glaciology*, *44*, 247–252.

Helm, V., S. Hendricks, S. Goebell, W. Rack, C. Haas, U. Nixdorf, and T. Boebel (2006), CryoVex 2004 and 2005 (BoB) data aquisition and final report, *Tech. rep.*, Alfred Wegener Institute for Polar and Marine Research.

Holland, M. M., C. M. Bitz, E. C. Hunke, W. H. Lipscomb, and S. J. L. (2006), Influence of the sea ice thickness distribution on polar climate in CCSM3, *J. Climate*, *19*, 2398–2414.

Hvidegaard, S. M., R. Forsberg, V. Helm, S. Hendricks, H. Skourup, L. Stenseng, S. Hanson, and Haas (2009), CryoVEx 2008, Final Report, *Technical report*, DTU-Space.

Kalnay, E., M. Kanamitsu, R. Kistler, W. Collins, D. Deaven, L. Gandin, M. Iredell, S. Saha, G. White, J. Woollen, Y. Zhu, A. Leetmaa, B. Reynolds, M. Chelliah, W. Ebisuzaki, W. Higgins, J. Janowiak, K. C. Mo, C. Ropelewski, J. Wang, R. Jenne, and D. Joseph (1996), The NCEP/NCAR 40-Year Reanalysis Project., *Bull. Amer. Meteor. Soc.*, *77*, 437–470.

Kwok, R., G. Cunningham, H. Zwally, and D. Yi (2006), ICESat over Arctic sea ice: Interpretation of altimetric and reflectivity profiles, *J. Geophys. Res.*, *111*, C06,006.

Kwok, R., G. Cunningham, H. Zwally, and D. Yi (2007), Ice, Cloud and land Elevation Satellite (ICESat) over Arctic sea ice: Retrieval of Freeboard, *J. Geophys. Res.*, *112*, C12,013.

Laxon, S., N. Peacock, and D. Smith (2003), High interannual variability of sea ice thickness in the Arctic region, *Nature*, *425*, 947–949.

Leuschen, C. J., R. N. Swift, J. C. Comiso, R. K. Raney, R. D. Chapman, W. B. Krabill, and J. G. Sonntag (2008), Combination of laser and radar altimeter height measurements to estimate snow depth during the 2004 Antarctic AMSR-E Sea Ice field campaign, *J. Geophys. Res.*, *113*, 4–+, doi: 10.1029/2007JC004285.

Mäkynen, M. P., and M. T. Hallikainen (2009), Simulation of ASIRAS Altimeter Echoes for Snow-Covered First-Year Sea Ice, *Geoscience and Remote Sensing Letters, IEEE*, *6*(3), 486–490.

Mätzler, C., and U. Wegmüller (1987), Dielectric Properties of Fresh-Water Ice at Microwave Frequencies, *Journal of Physics D: Applied Physics*, *20*(12), 1623–1630.

Nghiem, S., I. Rigor, D. Perovich, P. Clemente-Colón, J. Weatherly, and G. Neumann (2007), Rapid reduction of Arctic perennial sea ice, *Geophys. Res. Lett.*, *34*, L19,504.

Onstott, R. (1992), SAR and Scatterometer Signatures of Sea Ice, in *Microwave Remote Sensing of Sea Ice*, edited by F. Carsey, no. 68 in Geophysical Monograph, chap. 5, pp. 73 – 104, American Geophysical Union.

Stenseng, L., S. Hvidegaard, H. Skourup, R. Forsberg, C. Andersen, S. Hanson, R. Cullen, and V. Helm (2007), Airborne Lidar and Radar measurements in and around Greenland, CryoVEx 2006, *Tech. rep.*, Danish National Space Center.

Stroeve, J., M. Serreze, S. Drobot, S. Gearheard, M. Holland, J. Mas¡lanik, W. Meier, and S. T. (2007), Arctic sea ice extent plummets in 2007, *Eos Trans. AGU*, *89*(13).

Tonboe, R., S. Andersen, R. Gill, and L. Pedersen (2005), The simulated seasonal variability of the Ku-Band radar altimeter effective scattering surface depth in sea ice, in *Arctic sea ice thickness: Past, present and future*, edited by P. Wadhams and G. Amanatidis, European Commission.

Tonboe, R., S. Andersen, and L. Pedersen (2006), Simulation of the Ku-Band Radar Altimeter Sea Ice Effective Scattering Surface, *IEEE Geosc. Remote Sens. Let*, *3*(2), 237–240.

Warren, S., I. Rigor, N. Untersteiner, V. Radionov, N. Bryazgin, V. Aleksandrov, and R. Colony (1999), Snow depth on Arctic sea ice, *Journal of Climate*, *12*, 1814–1829.

Willatt, R., S. Laxon, K. Giles, A. Ridout, and R. Cullen (2010a), Observations of ku-band radar penetration into snow on sea ice using in-situ, airborne and satellite techniques in support of cryosat-2, *submitted to Annals of Glaciology*.

Willatt, R. C., K. A. Giles, S. W. Laxon, L. Stone-Drake, and A. P. Worby (2010b), Field investigations of ku-band radar penetration into snow cover on antarctic sea ice, *IEEE Transactions on Geoscience and Remote Sensing*, *48*(1), 365–372, doi:10.1109/TGRS.2009.2028237.

Wingham, D., C. G. Rapley, and G. H. (1986), New techniques in satellite altimeter tracking systems, in *Proceedings of the IGARSS Symposium*, vol. SP-254, edited by T. D. Guyenne and J. J. Hunt, pp. 1339–1344.

Wingham, D., C. Francis, S. Baker, C. Bouzinac, D. Brockley, R. Cullen, P. Chateau-Thierry, S. Laxon, U. Mallow, C. Mavrocordatos, L. Phalippou, G. Ratier, L. Rey, F. Rostan, P. Viau, and D. Wallis (2006), CryoSat: A mission to determine the fluctuations in Earths's land and marine ice fields, *Adv. Space Res.*, *37*, 841–871.

Zwally, H. J., D. Yi, R. Kwok, and Y. Zhao (2008), ICESat measurements of sea ice freeboard and estimates of sea ice thickness in the Weddell Sea, *J. Geophys. Res.*, *113*, 2–+, doi: 10.1029/2007JC004284.

S. Hendricks, Sea Ice Physics, Alfred-Wegener Institute for Polar and Marine Research, Bussestr. 24, Bremerhaven, 27570, Germany. (stefan.hendricks@awi.de)

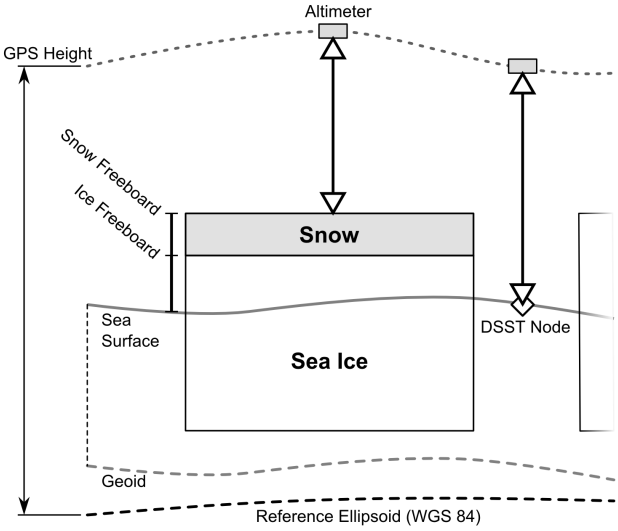

Figure 1. Satellite altimeter missions determine freeboard by range measurements to the ice surface and to the dynamic sea surface topography (DSST). The height of the sea surface is determined by the shape of the geoid and the influence of ocean currents and atmospheric pressure. The laser altimeters yield snow freeboard, since the laser beam is always reflected at the top snow surface. For radar altimeters it is assumed that radar pulses penetrate the snow layer to the ice-snow interface and therefore measure ice freeboard.

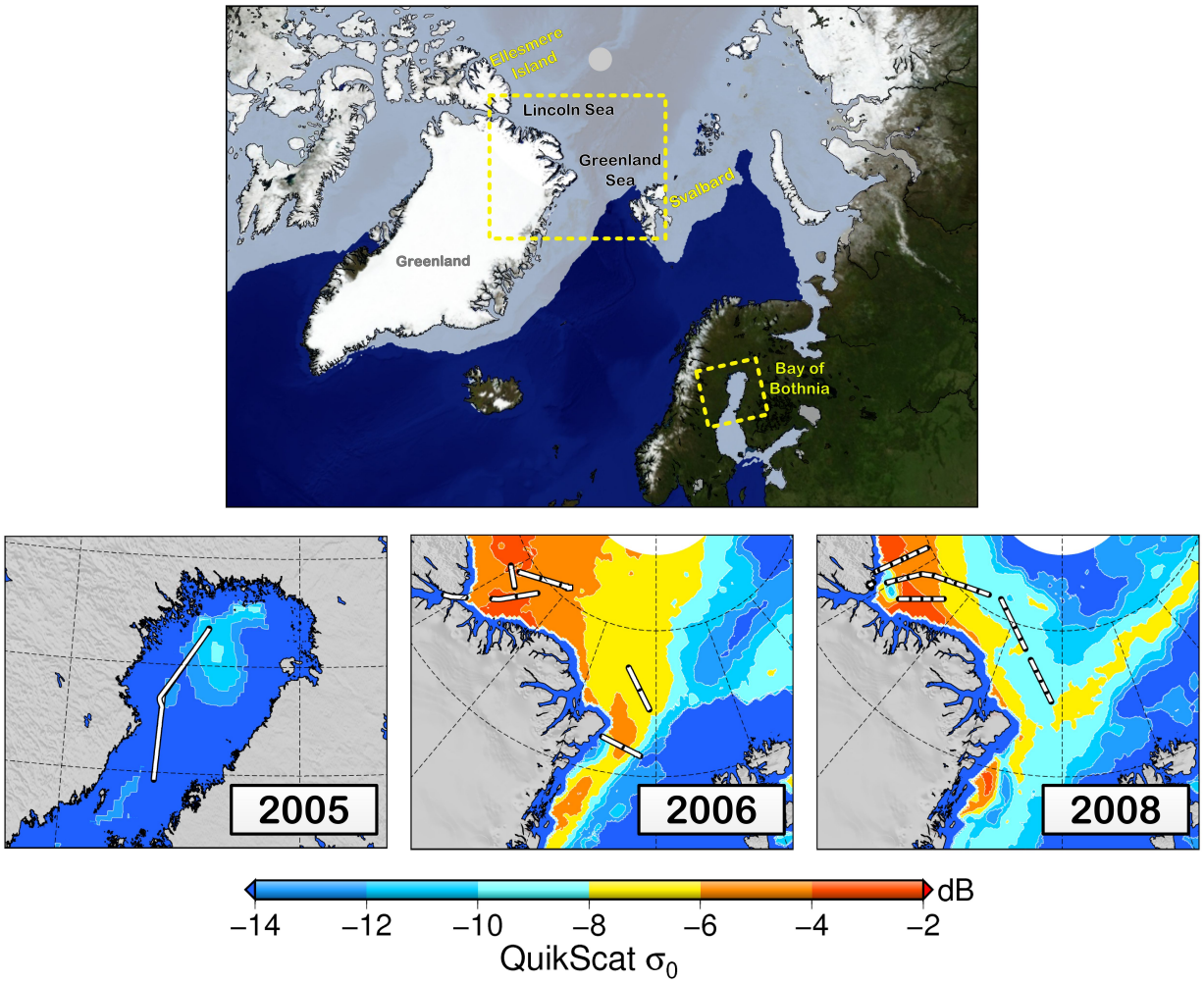

Figure 2. Geographical location of the CryoVEx surveys in 2005 (Baltic Sea) and in 2006 and 2008 in the Arctic Ocean (Greenland and Lincoln Sea). Survey lines of the individual years (lower panels) are shown together with QuikScat backscatter maps acquired during the time of the flights. Higher backscatter (red colors) corresponds to higher surface roughness, which is typical for perennial sea ice.

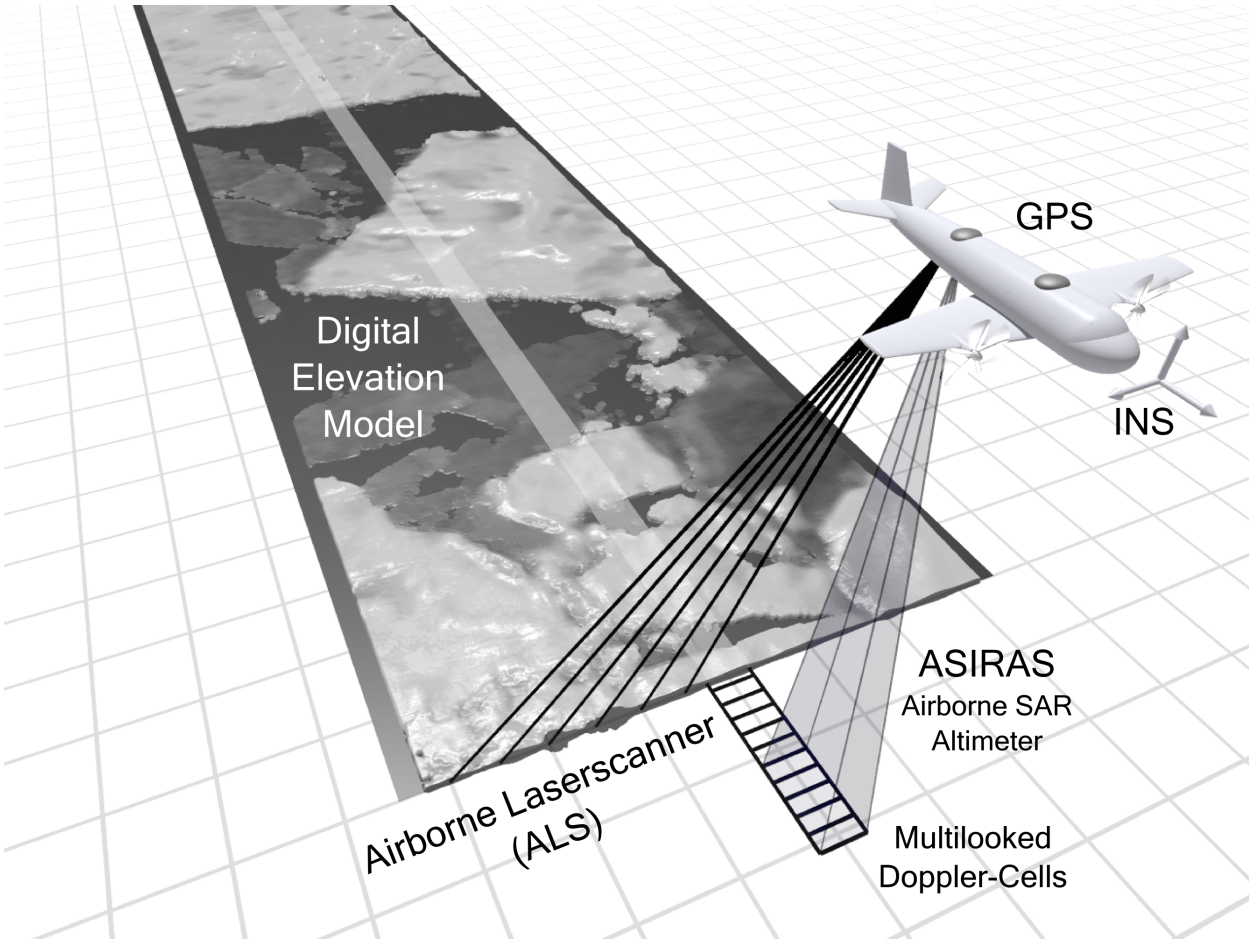

Figure 3. Aircraft instrumentation during CryoVEx field campaigns. Digital elevations models were obtained with a cross-track scanning airborne laserscanner (ALS) and an along-track SAR K_u-Band radar altimeter (ASIRAS). Two differential GPS antennas and a inertial navigation system (INS) were used for exact geolocation of the digital elevation models.

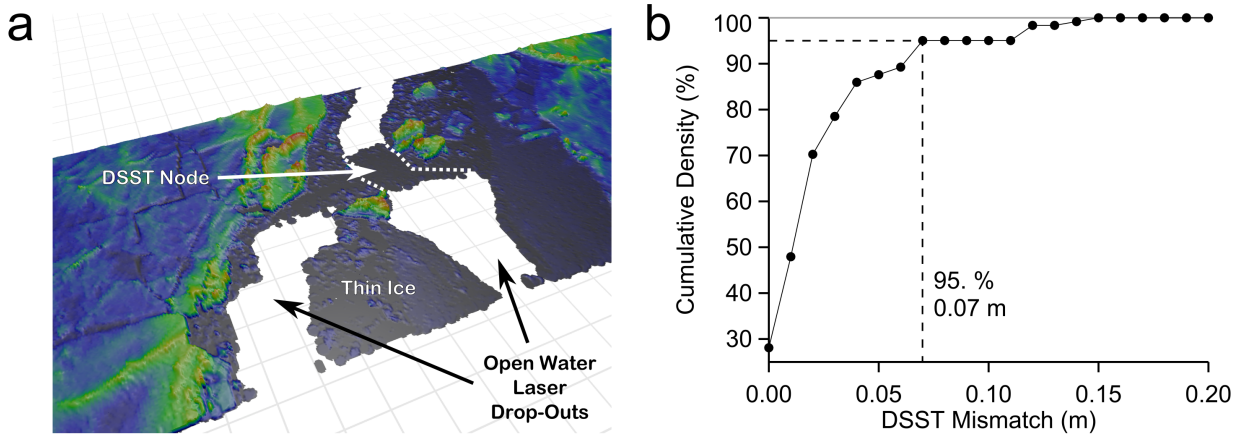

Figure 4. a) Laser DEM example of open water lead used for the estimation of the sea surface height. ALS data drop outs due to specular reflection at the side of the laser swath indicate open water, while laser returns can be detected over thin ice. The elevation of the sea surface is taken from the swath center. b) Cumulative histogram of discrepancy between manual and automatic classification of sea surface elevation. At 95% of a test profile the difference is 0.07 m or less.

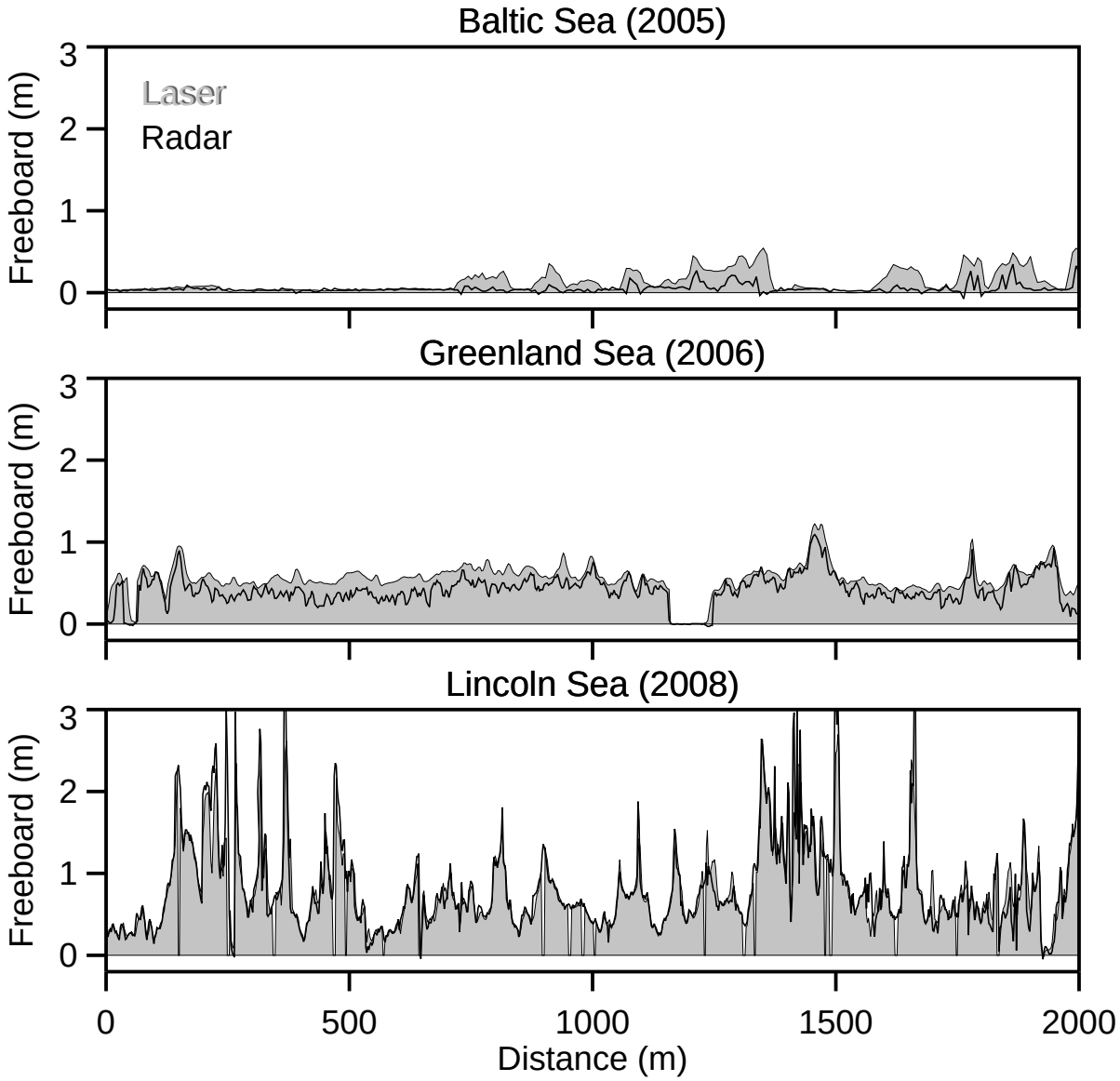

Figure 5. Typical examples of laser (gray-shaded area) and radar (black line) freeboard profiles from the three main study regions. The lateral resolution of these examples varies with the ASIRAS operation mode and aircraft speed (Baltic Sea: 7.0 m, Greenland Sea: 3.1 m, Lincoln Sea: 2.1 m).

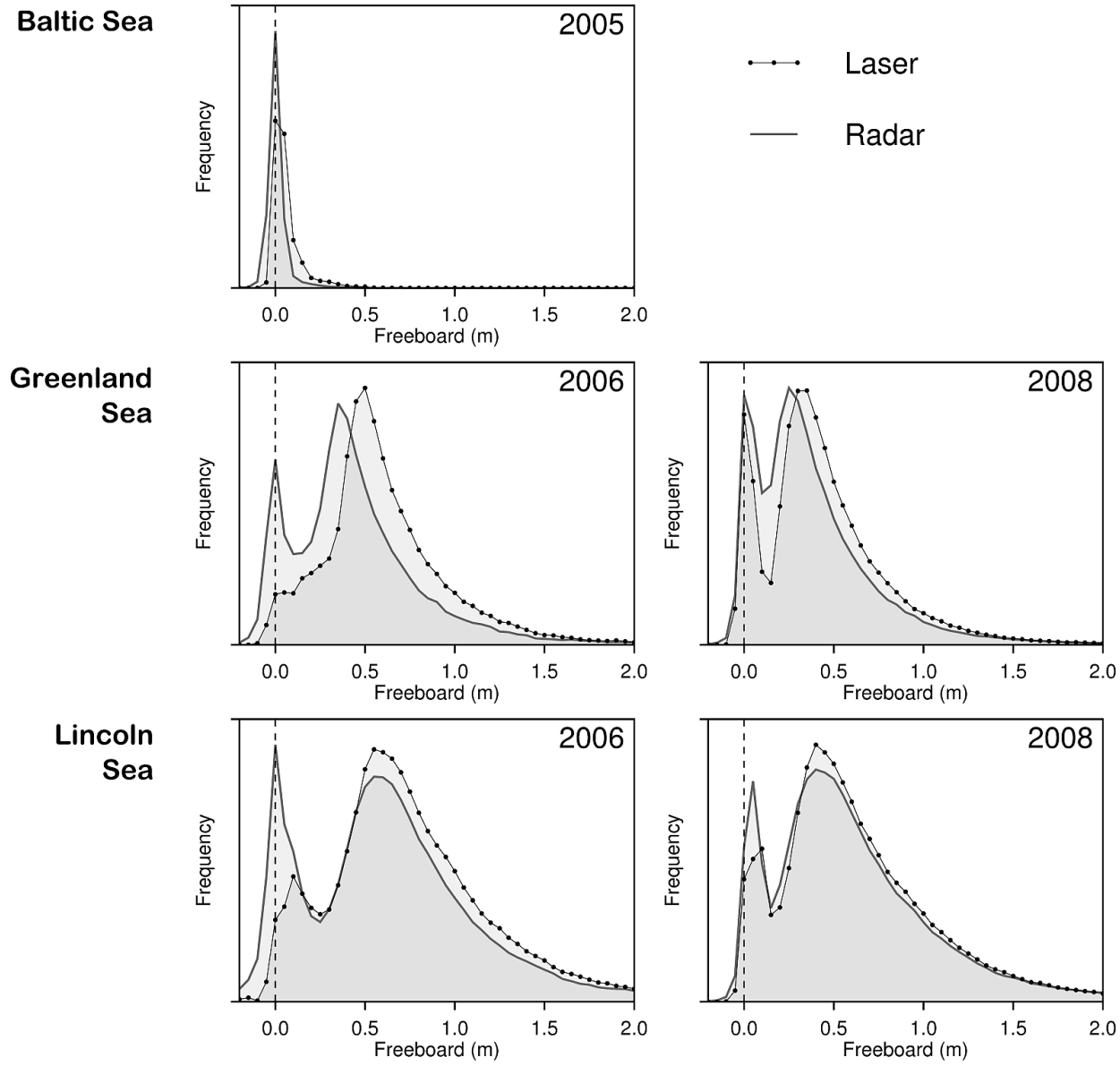

Figure 6. Laser (dotted line) and radar freeboard (continuous line) probability distributions in the CryoVEx validation areas for each year.

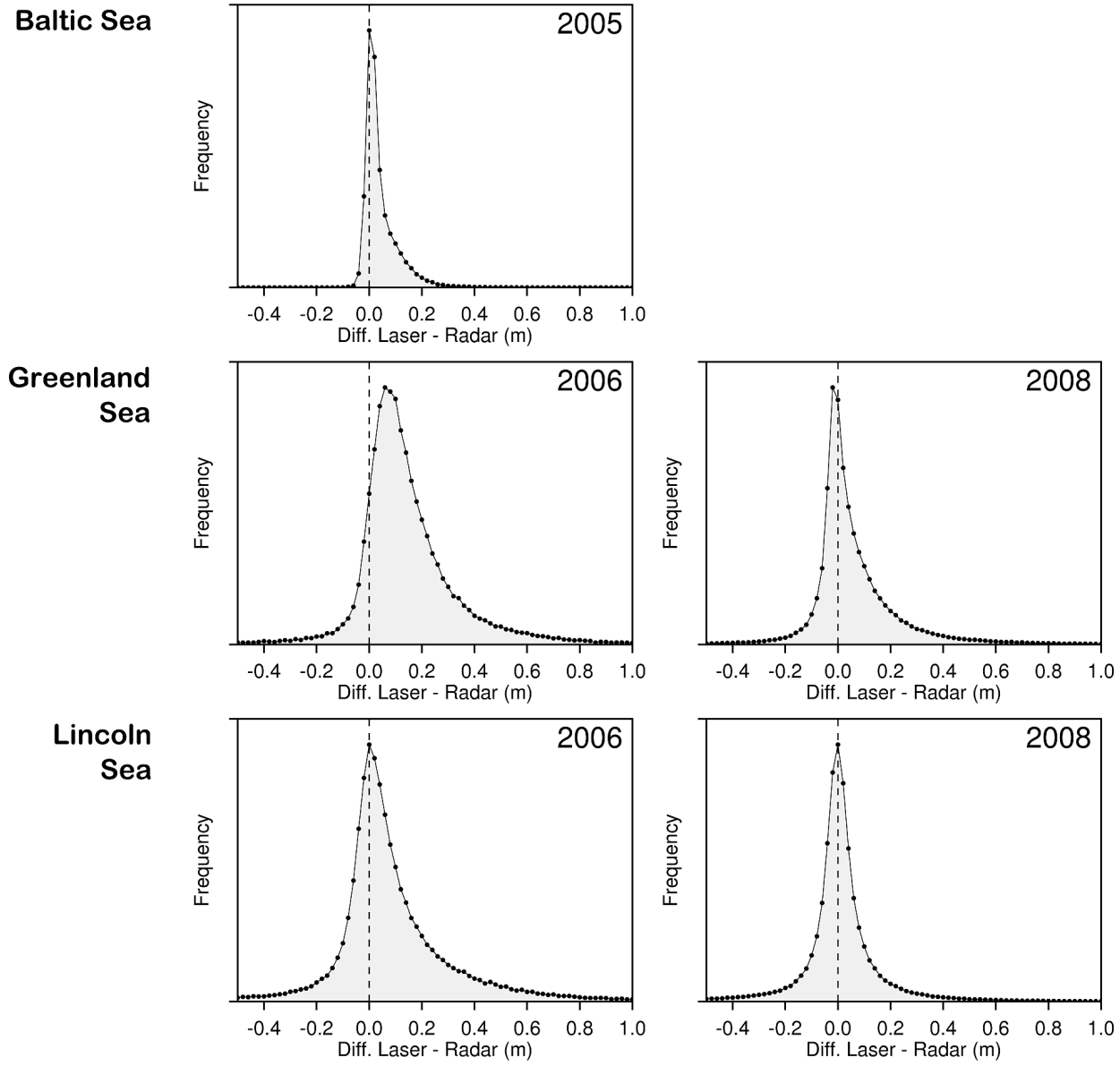

Figure 7. Probability distributions of point-to-point differences between laser and radar freeboard (laser minus radar) for each year and region.

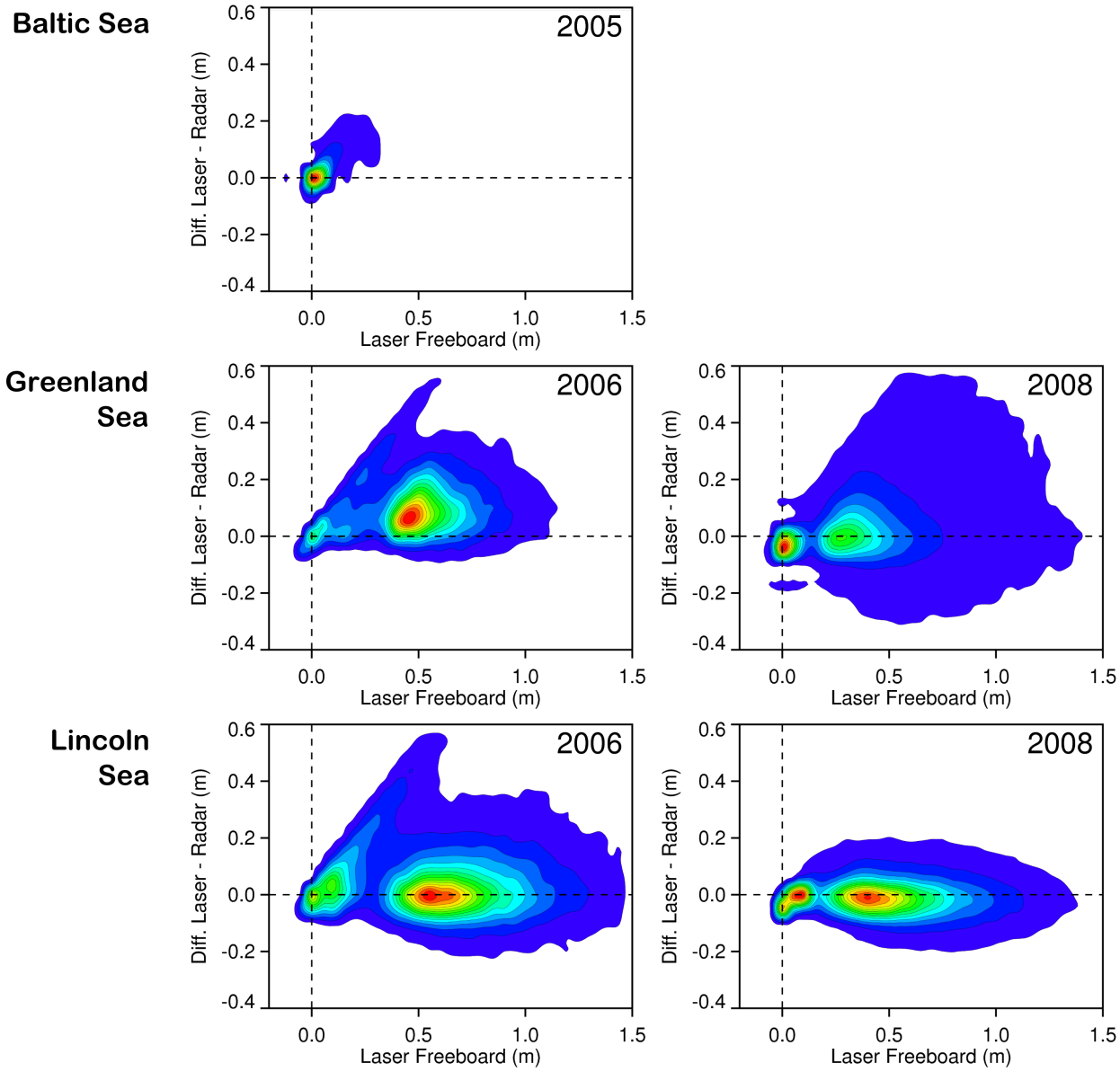

Figure 8. Data point density of point-to-point laser and radar freeboard differences versus laser freeboard for all regions and years. High density given by red, low density by blue colors.

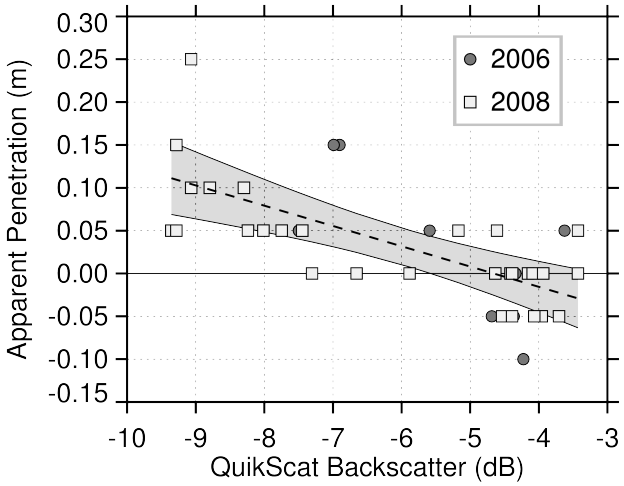

Figure 9. Linear regression of apparent penetration (modal difference between laser and radar freeboard) versus QuikScat backscatter of all profiles in the western Arctic Ocean. Shaded areas represents the 95% confidence interval of the regression.

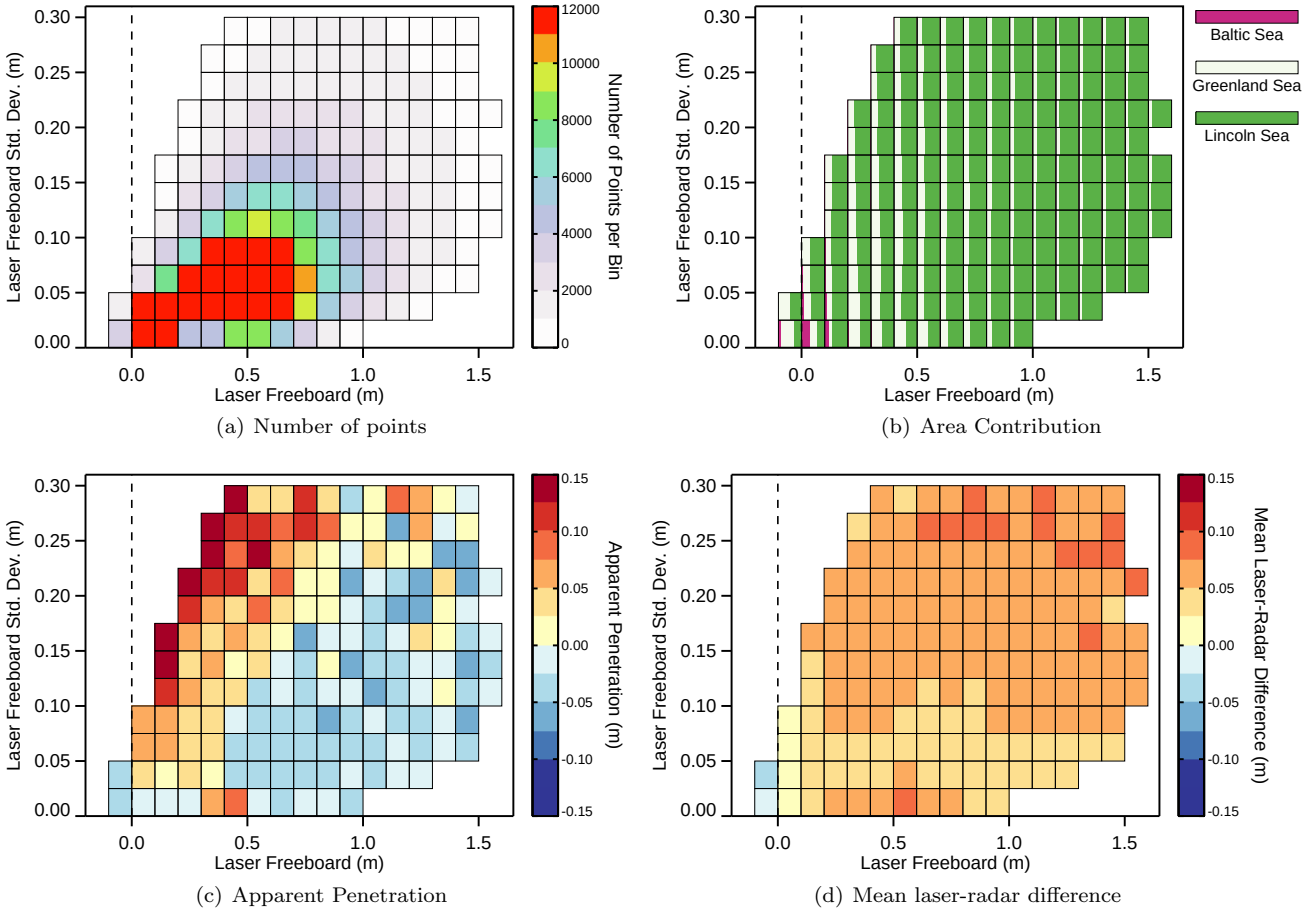

(a) Number of points

(b) Area Contribution

(c) Apparent Penetration

(d) Mean laser-radar difference

Figure 10. Classification of all data points in bins of laser freeboard and laser DEM standard deviation inside the radar footprint. Graphs show color-coded the number of data points (upper left), contribution by region to each bin (upper right), apparent penetration (lower left) and mean laser minus radar difference (lower right) for all data points within each bin. Bins with less then 500 points are not shown.

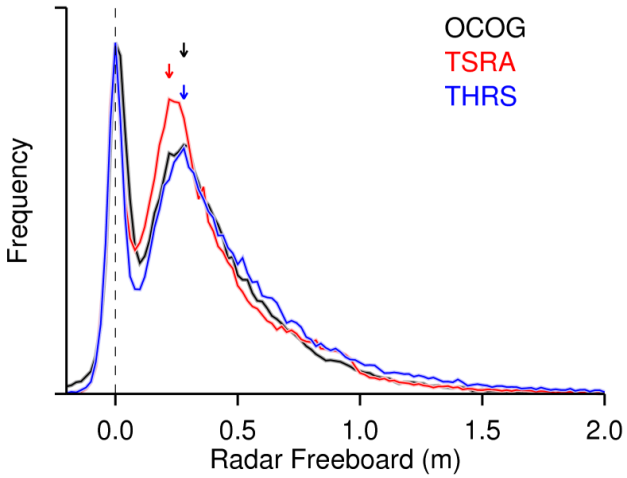

Figure 11. Probability distribution of radar freeboard by three different retracker algorithms for a test profile in the Greenland Sea. Vertical arrows mark the modal freeboard used for the estimation of apparent penetration of the individual retrackers.

A.5 Publications and Technical Reports Related to the Thesis

- *Initial Results of CryoSat-2 Data from the Arctic*; Stine Kildegaard Poulsen, Lars Stenseng, Henriette Skourup, Leif Toudal Pedersen, Rene Forsberg, and Louise Sandberg Sørensen; Proceedings CryoSat-2 Validation Workshop 2011. (Poulsen et al., 2011)
- *Airborne Campaigns for CryoSat Prelaunch Calibration and Validation*; Henriette Skourup, Rene Forsberg, Susanne Hanson, Sine Munk Hvidegaard, Elizabeth M. Morris, Peter Nienow, Stine Kildegaard Poulsen, and Lars Stenseng; Proceedings CryoSat-2 Validation Workshop 2011. (Skourup et al., 2011)
- *SAMOSA-2: Validation Against ASIRAS. Version 1.1 2011*; Lars Stenseng and Christine Gommenginger; ESA Technical Note. (Stenseng and Gommenginger, 2011).
- *Effect of Surface Roughness on Sea-Ice Freeboard Retrieval with an Airborne K_u-Band SAR Radar Altimeter*; Stefan Hendricks, Veit Helm, Lars Stenseng, and Christian Haas; Proceedings IGARSS 2010. (Hendricks et al., 2010)
- *CryoSat2 Pre-Launch Validation Measurements on Arctic Sea Ice*; Marcel Nicolaus, Stefan Hendricks, Lars Stenseng, Veit Helm, Rüdiger Gerdes, and Christian Haas; Proceedings ESA-Living Planet Symposium 2010. (Nicolaus et al., 2010).
- *Airborne Campaigns for CryoSat Pre-Launch Calibration and Validation*; Sine M. Hvidegaard, Rene Forsberg, Henriette Skourup, and Lars Stenseng; Proceedings ESA-Living Planet Symposium 2010. (Hvidegaard et al., 2010)
- *SAMOSA: Validation Using Airborne ASIRAS Data. Version 1.1, August 2009*; Lars Stenseng; ESA Technical Note. (Stenseng, 2009).
- *CryoVEx 2008 Final Report*; Sine M. Hvidegaard, Rene Forsberg, Veit Helm, Stefan Hendricks, Henriette Skourup, Lars Stenseng, Susanne Hanson, and Christian Haas; Danish National Space Institute, DTU, Technical Report 2/2009. (Hvidegaard et al., 2009).
- *Airborne Lidar and Radar Measurements In and Around Greenland, CryoVEx 2006*; Lars Stenseng, Sine M. Hvidegaard, Henriette Skourup, Rene Forsberg, Christian J. Andersen, Susanne Hanson, Robert Cullen, and Veit Helm; Danish National Space Center, Technical Report 9/2007. (Stenseng et al., 2007).

Appendix B

Abbreviations and Acronyms

ASAR	Advanced Synthetic Aperture Radar
ASIRAS	Airborne SAR/Interferometric radar altimeter system
CryoVEx	CryoSat validation experiment
CVRT	Calibration, Validation, and Retrieval Team
D2P	delay-Doppler Phase-monopulse
DEM	Digital elevation model
DTU	Technical University of Denmark
Envisat	Environment satellite
EGIG	Expedition Glaciologique Internationale au Groenland
EGM	Earth Gravitational Model
ERS	European Remote Sensing satellite
ESA	European Space Agency
FFT	fast Fourier transform
FM	Frequency modulation
GSFC	Goddard Space Flight Centre
GMES	Global Monitoring for Environment and Security
GPS	Global positioning system
HAM	High altitude mode
INS	Inertial navigation system
LAM	Low altitude mode
LGPL	GNU Lesser General Public License
LRM	Low resolution mode
NASA	National aeronautics and space administration
NBI	Niels Bohr Institute
OCOG	Offset center of gravity
PRF	Pulse repetition frequency
RST	Radar Systemtechnik
SAMOSA	Development of SAR altimetry mode studies and applications over ocean, coastal zones and inland water
SAR	Synthetic aperture radar
SARin	SAR/interferometry
SIRAL	SAR/interferometric altimeter
SRAL	SAR radar altimeter
SSMIS	Special Sensor Microwave Imager/Sounder
SWH	significant wave height

DTU Space
National Space Institute
Technical University of Denmark

Juliane Maries Vej 30
DK-2100 København Ø

Tel +45 3532 5700
Fax +45 3536 2475

http://www.space.dtu.dk

ISBN: 978-87-92477-06-4